Veit Scharf

Neutral Pion Subshower Reconstruction in Hadronic Tau Lepton Decays at the ATLAS Experiment

Diplomarbeit

Faculty of Physics and Astronomy

University of Heidelberg

Diploma thesis

in Physics

submitted by

Veit Scharf

born in Kulmbach

2009

Neutral Pion Subshower Reconstruction in Hadronic Tau Lepton Decays at the ATLAS Experiment

This diploma thesis has been carried out by Veit Scharf at the

Kirchhoff-Institute for Physics

under the supervision of

Dr. Jochen Dingfelder

Zusammenfassung

Die Identifizierung von Tau-Leptonen spielt bei der Suche nach dem Higgs-Boson und nach neuer Physik am Large Hadron Collider (LHC) eine wichtige Rolle. In vielen supersymmetrischen Modellen werden Tau-Leptonen mit kleinen Transversalimpulsen in den langen Zerfallsketten supersymmetrischer Teilchen erwartet. Diese stellen eine grosse Herausforderung für die Rekonstruktion im ATLAS-Detektor dar. Das Ziel dieser Arbeit ist es, die in hadronischen Tau-Zerfällen auftretenden Pionen unter Ausnutzung der hohen Granularität des elektromagnetischen Kalorimeters einzeln zu rekonstruieren und somit die Rekonstruktion und Identifikation des Tau-Zerfalls insbesondere für kleine Transversalimpulse zu verbessern.

Es wird ein Algorithmus zur Rekonstruktion neutraler Pionen in Tau-Zerfällen vorgestellt. Hierzu werden Tau-Zerfälle mit einer geladenen Spur (1-Prong) in simulierten Ereignissen aus Z-Boson-Produktion mit anschliessendem Zerfall $Z \rightarrow \tau\tau$ selektiert. Der Algorithmus basiert auf der Idee, die Energie des geladenen Pions aus dem elektromagnetischen Kalorimeter zu entfernen und in der verbleibenden Energieverteilung neutrale Pionen zu identifizieren. Die Anzahl der neutralen Pionen ermöglicht eine Klassifizierung der Tau-Lepton-Zerfälle als $\tau \rightarrow \pi\nu$, $\tau \rightarrow \rho\nu$ oder $\tau \rightarrow a_1\nu$ und eine Rekonstruktion der intermediären Resonanzen ρ und a_1. Die Leistungsfähigkeit des Algorithmus wird in Abhängigkeit der kinematischen Eigenschaften der Tau-Zerfälle studiert. Die Trennung verschiedener Zerfallskanäle ist nicht nur für die Tau-Rekonstruktion nützlich, sondern sie ist auch für Physik-Analysen von Bedeutung, z.B. für Studien der Polarisation von Tau-Leptonen aus Zerfällen neu entdeckter Teilchen.

Abstract

The identification of tau leptons plays an important role for the search for the Higgs boson and for new physics at the Large Hadron Collider (LHC) . In many supersymmetric models tau leptons with small transverse momenta can be expected in the long decay chains of supersymmetric particles . These present a great challenge for reconstruction with the ATLAS detector. The goal of this thesis is to separately reconstruct the neutral pions in hadronic tau-lepton decays by taking advantage of the high granularity of the electromagnetic calorimeter, thus to improve the reconstruction and identification of tau leptons, especially for small transverse momenta.

An algorithm for the reconstruction of neutral pions from tau decays is presented. Tau decays with one charged track (1 prong) are selected in simulated events from Z boson production with subsequent decay $Z \rightarrow \tau\tau$. The algorithm is based on the idea of subtracting the energy of the charged pion from the electromagnetic calorimeter and to identify the neutral pions in the remaining energy distribution. The number of neutral pions can be used to classify the tau-lepton decays as $\tau \rightarrow \pi\nu$, $\tau \rightarrow \rho\nu$ or $\tau \rightarrow a_1\nu$ and to reconstruct the intermediary resonances - ρ and a_1. The performance of the algorithm is examined in dependence of the kinematic properties of the tau decay. The identification of separate tau-lepton decay modes is not only useful for tau reconstruction but also for physics analyses, i.e. studies of the polarization of tau leptons coming from the decay of newly discovered particles.

Contents

Introduction

In 2009 the Large Hadron Collier (LHC) and its four experiments ALICE, ATLAS, CMS and LHCb will restart operation and record first collision data. The LHC will take particle physics to the "terascale", an energy frontier never reached before. At the LHC, protons will be collided with a center-of-mass energy of $14\,\mathrm{TeV}$ at a rate of $1\,\mathrm{GHz}$. The main goal of the two general purpose detectors ATLAS and CMS is finding the Higgs boson and physics beyond the Standard Model. The Higgs boson, which has been searched for for a long time, is the last not yet discovered particle predicted by the Standard Model. Since the Standard Model has some apparent problems, many theories describing physics beyond the Standard Model have been developed over the last decades, for instance the supersymmetric extensions to the Standard Model.

Tau leptons are expected to play an important role for the discovery of new physics at the LHC, in particular for the search for the Higgs boson and for supersymmetry (SUSY). Since the Higgs boson couples to mass, the decay to tau leptons, as the heaviest leptons, is a promising decay mode for Higgs searches in the low-mass region. Also a large part of the SUSY parameter space, the region with large $\tan\beta$, predicts enhanced couplings to tau leptons. Since for large $\tan\beta$ the electron and muon channels of SUSY decays have very small branching fractions, it could even be, that the tau lepton is the only lepton which allows for a discovery of SUSY. In addition only third generation particles have a visible mixing of the left and right handed eigenstates to mass eigenstates in SUSY. Studying the mixing in the τ-sector could help to understand the SUSY breaking mechanism.

To exploit the discovery potential of tau leptons to its full extend a good tau-lepton reconstruction is necessary. Since leptonic tau-lepton decays cannot be distinguished from direct lepton production the tau-lepton identification at ATLAS is based on hadronic tau-lepton decays. The signatures of hadronic tau-lepton decays used to reconstruct tau-lepton candidates are narrow jets with one or three associated tracks coming from charged particles. The biggest challenge for a successful tau-lepton identification is the abundant background of jets from QCD processes, which may fake a tau lepton in the detector. The suppression of the jet background is based on using jet-shape and tracking variables. While algorithms for tau-lepton identification already exists in ATLAS, an important step to improve the tau-lepton identification is to study the substructure of tau-jets in the calorimeter, especially the neutral pions accompanying the decay.

This thesis presents an algorithm for the reconstruction of the substructure of tau-jets due to neutral pions from hadronic tau-lepton decays. The neutral pion reconstruction is expected to work best for tau leptons with relatively low transverse momentum, for which the particles in the decay are not so strongly boosted, that they all overlap in the detector. However the algorithm presented here is able to reconstruct neutral pions that overlap with energy depositions of charged particles from the tau-lepton decay. The algorithm is based on the idea of removing energy contributions from the electromagnetic calorimeter that come from charged particles. Then the resulting energy distribution, now containing only contributions

from neutral particles, is used to find the neutral pion subshowers. The goal of this algorithm is to improve the tau lepton identification at low transverse momenta by improving suppression of jets from QCD processes and to allow for an identification of different hadronic tau decay modes for physics analyses. In addition to the development of the algorithm detailed performance studies are presented and the dependence of the algorithm's performance on the kinematics of tau-lepton decays are presented.

The structure of this thesis is as follows:

- Chapter 1 provides the theoretical background for the work presented in this thesis. The Standard Model is summarized and its minimal supersymmetric extension is introduced as an example for new physics. The role of tau leptons for physics analyses at the ATLAS and CMS experiments is discussed. Also the properties of tau-lepton decays are presented.

- In Chapter 2 the Large Hadron Collider and the ATLAS Experiment are introduced. The focus is set on the inner-tracking system and in particular on the calorimeter, which play an important role for this thesis

- Chapter 3 gives an overview of the tau-lepton reconstruction at the ATLAS experiment.

- Chapter 4 introduces the datasets and the selection of the tau-lepton samples used for this thesis.

- Chapter 5 describes the algorithm for the reconstruction of neutral pion subshowers in detail. This is done by illustrating the individual steps necessary for the reconstruction and the efforts made to validate each step.

- In Chapter 6 the performance of the neutral pion reconstruction algorithm is studied. These results are compared to the existing algorithm and an approach for using the algorithm with first data is shown.

- Chapter 7 gives some ideas and plans how the algorithm can be validated with data which systematic effects will have to be studied after its validation. Also an outlook on possible future improvements is given.

- Chapter 8 summarizes the results of this thesis.

Chapter 1

Theoretical Introduction

In this chapter the theoretical background for the studies in this work is provided. First the Standard Model of particle physics is introduced. Then a short overview of models for physics beyond the Standard Model is given, with a focus on Supersymmetry (SUSY). For a large part of the SUSY parameter space, tau leptons in the final state of decays of SUSY particles are an important signature. Finally, the properties of tau leptons and the kinematics and characteristics of their decays are presented. Their role as a probe for new physics at the Large Hadron Collider (LHC) are discussed.

1.1 The Standard Model of Particle Physics

The Standard Model (SM) of particle physics describes the known elementary particles and three of the four fundamental interactions between them. Only gravitation, which is several orders of magnitude weaker and can be neglected for energies far below the Planck scale, is not included in this model. The Standard Model was established by Glashow, Salam, Weinberg, Wilczek, Gross, Politzer and others in the late sixties and early seventies and has successfully described almost all experimental data gathered over the last thirty years with a good precision. It is a relativistic quantum field theory. The spectrum of elementary particles contains fermions with half-integer spin and bosons with integer spin. Each particle is described by a set of quantum numbers, e.g. spin, parity, charge, isospin, etc. Every fermion has a corresponding antiparticle which has opposite charge and parity, but otherwise the same quantum numbers. The interactions between these particles, namely the electromagnetic, the weak and the strong interactions, are mediated by the exchange of so called "gauge bosons". The weak force couples to all twelve fermions whereas the electromagnetic force couples to nine and the strong force only to six fermions. This gives a first categorization of the elementary particles: fermions only coupling to the weak force or the electromagnetic force are called "leptons", while fermions which couple in addition to the strong force are called "quarks". They can be grouped further by their electric charge q_e (in units of the electron charge) into four groups:

1. up-type quarks ($q_e = +2/3$)

2. down-type quarks ($q_e = -1/3$)

3. neutral leptons ($q_e = 0$)

4. charged leptons ($q_e = -1$)

Each group consists of three generations of fermions. The visible matter surrounding us is composed of fermions belonging to the first generation. The fermions from the second and third generations are only produced in high energy physics experiments or cosmic radiation. The complete listing of all twelve fundamental fermions and the interactions they participate in is given in Tab. 1.1.

	Generation			**Interaction**
	I	II	III	
up-type quarks	u	c	t	strong, weak, electromagnetic
down-type quarks	d	s	b	strong, weak, electromagnetic
neutral leptons	ν_e	ν_μ	ν_τ	weak
charged leptons	e^-	μ^-	τ^-	weak, electromagnetic

Table 1.1: The twelve fundamental fermions of the Standard Model of particle physics, their generation and the interactions they participate in. The corresponding anti-particles are not listed.

The gauge bosons, that are responsible for the various interactions, their couplings and the relative strengths of the forces they mediate are given in Tab. 1.2.

Interaction	**Gauge Boson**	**Couples to**	**Relative Strength**
strong	gluons	color charge	1
electromagnetic	photon	electromagnetic charge	10^{-2}
weak	Z^0, $W^\pm$	weak charge	10^{-6}

Table 1.2: The three interactions described by the Standard Model, their gauge bosons, couplings and strength relative to the strong interaction.

The electromagnetic interaction, described by "Quantum Electro Dynamics" (QED), is mediated by the exchange of a single massless gauge boson, the photon that couples to electric charge. The theory of the weak interaction contains three heavy gauge bosons: the Z^0 ($m_Z = 91.2\,\text{GeV}$) and the $W^\pm$ ($m_W = 80.4\,\text{GeV}$). They couple to weak charge. Only left-handed fermions and right-handed anti-fermions carry weak charge.

The strong interaction is described by the theory of "Quantum Chromo Dynamics" (QCD). Eight massless gluons mediate the strong force. They couple to the so-called color charge. It is carried only by quarks and the gluons themselves. Each quark carries one out of three colors (red, green and blue) and gluons exchange colors between quarks. Only colorless states[1] are allowed in QCD and thus free quarks do not exist. Quarks appear either in bound quark – antiquark states ($q\bar{q}$) called mesons or in three-quark states (qqq or $\overline{qqq}$) called baryons.

The electromagnetic and the weak interactions were unified and successfully described as a single interaction called electroweak interaction. The apparent differences between them at energies below 100 GeV are explained by the mechanism of spontaneous symmetry breaking. This mechanism requires a doublet of complex scalar fields, the Higgs doublet. Three of four degrees of freedom of the complex Higgs doublet are needed to give masses to the vector bosons $W^\pm$ and Z^0. The fourth degree of freedom corresponds to a physical scalar particle, the Higgs boson. The electroweak and strong interactions could not yet be unified, but there is the possibility of unifying them at the GUT scale ($\approx 10^{15}\,\text{GeV}$).

---

[1] A combination of the three different colors or a combination of color and anticolor yields a colorless state.
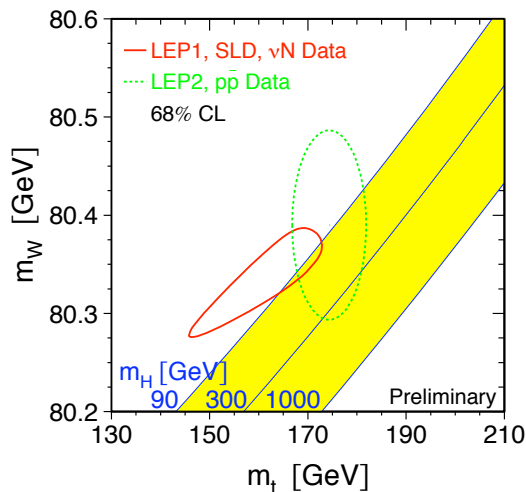
Figure 1.1: Constraints of direct m_W and m_t measurements (dotted ellipse) compared with constraints from precision electroweak data (solid curve) [2].

The Higgs boson is the last particle predicted by the Standard Model that has not yet been discovered. Its discovery is one of the main objectives of the ATLAS[2] and CMS[3] experiments at the LHC. A lower limit on the Higgs mass comes from direct searches of the $e^+e^- \rightarrow H^0 Z$ process at the Large Electron Positron Collider (LEP) leading to $m_H > 114.4\,\text{GeV}$ [1]. Upper limits are given by theoretical constraints and the results of fits to electroweak precision data. As a consequence the Higgs mass is expected to be in the range $114.4\,\text{GeV} < m_H \lesssim 180\,\text{GeV}$ (see Fig. 1.1).

1.2 New Physics Beyond the Standard Model

Although the Standard Model of particles physics has been very successful in describing all experimental data to date, it cannot be a complete theory of fundamental physics, as it still has some apparent problems:

- it contains numerous free parameters, which have to be determined using experimental data;

- gravity is not included;

- the "hierarchy problem", which arises from the huge difference of many orders of magnitude between the electroweak scale ($O\,(100)$ GeV) and the GUT $O\left(10^{15}\right)$ GeV) or the Planck ($O\left(10^{19}\right)$ GeV) scale. The radiative corrections to the Higgs mass are of the order of Λ^2: $m_H^2 = m_{H,0}^2 + O\left(\Lambda^2\right)$, where $m_{H;0}$ denotes the "bare" Higgs mass. Here Λ is the scale up to which the Standard Model is supposed to remain valid. A natural choice is the Plank scale (M_{Pl}), which would result in a Higgs mass that corresponds to the Planck mass.

---

[2] A Toroidal LHC Apparatus
[3] Compact Muon Solenoid
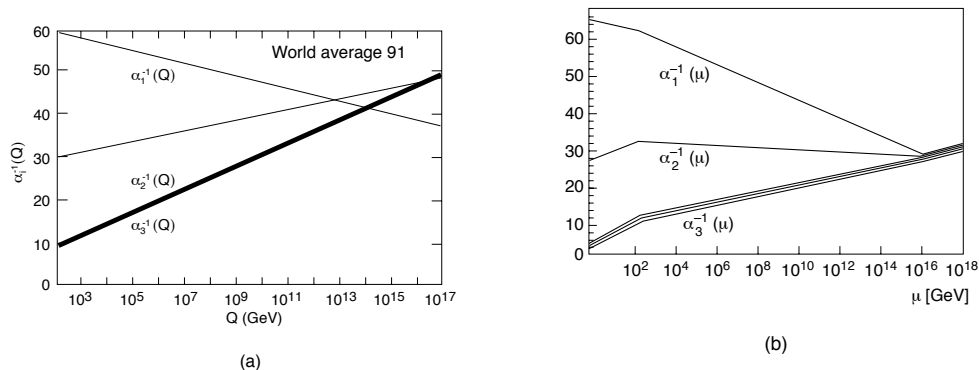
Figure 1.2: Measurements of the gauge coupling strength without supersymmetry (a) and with supersymmetry(b) [4].

- "unification of forces" is not possible in the Standard Model; the coupling constants of the weak, electromagnetic and strong interactions do not meet in one point when extrapolated to high energies (see Fig. 1.2).

- the "dark matter" observed in cosmological measurements, e.g. WMAP [3], that accounts for $\approx 25\,\%$ of our universe cannot be explained. Even more mysterious in the dark energy which makes up $\approx 70\,\%$ of our universe.

In order to address these problems theories that extend the Standard Model have been developed. Some examples are SUSY, extra dimensions, compositeness, models with 4th generation quarks and leptons and many more. As an example the following section will give a short introduction to supersymmetry. SUSY is one of the best motivated and most widely favored extensions. In addition, tau-leptons play a key role in SUSY searches and thus the work presented in this thesis may be of direct relevance for SUSY analyses.

1.2.1 Supersymmetry

Supersymmetry could solve several of the problems of the Standard Model listed above. It states that every fundamental fermion has a so-called "superpartner" with the same quantum numbers, but a spin that differs by $1/2$. The supersymmetric extension of the Standard Model, which adds the minimal number of additional particles, is the so called "Minimal Supersymmetric Standard Model" (MSSM). It contains the Standard Model particles, their superpartners and five Higgs bosons. The nomenclature for the superpartners is as follows: the superpartners of quarks and leptons are denoted by prepending an "s" to their name, e.g. "squarks" or "sleptons". Superpartners of Standard Model bosons are denotes by appending "-ino" to the name, e.g. "gluino" for the superpartner of the gluon. The MSSM extends the Higgs sector of the Standard Model by requiring two complex Higgs doublets,

$$H_u = \begin{pmatrix} H_u^+ \\ H_u^0 \end{pmatrix}, \; H_d = \begin{pmatrix} H_d^0 \\ H_d^- \end{pmatrix} \tag{1.1}$$

with opposite hypercharges in order to give masses to up-type quarks and to down-type quarks and charged leptons, respectively. This yields in total five mass eigenstates for the

Higgs bosons: h^0, H^0 (CP-even), A^0 (CP-odd) and $H^\pm$. The complete particle spectrum of the MSSM is given in Tab. 1.3.

		SM-Particles		**Superpartners**	
Leptons	electron	e	selectron	$\tilde{e}$
	muon	μ	smuon	$\tilde{\mu}$
	tau	τ	stau	$\tilde{\tau}$
Neutrinos	neutrino	ν	sneutrinos	$\tilde{\nu}$
Quarks	up, down	u, d	sup, sdown	$\tilde{u}, \tilde{d}$
	charm, strange	c, s	scharm, sstrange	$\tilde{c}, \tilde{s}$
	top, bottom	t, b	stop, sbottom	$\tilde{t}, \tilde{b}$
Gauge particles	B boson, W^0 boson	B, W^0	Bino, Wino^0	$\tilde{B}, \tilde{W}^0$
	gluon, $W^\pm$ boson	$g, W^\pm$	gluino, Wino$^\pm$	$\tilde{g}, \tilde{W}^\pm$
Higgs	Higgs bosons	$h^0, H^0, A^0, H^\pm$	Higgsinos	$\tilde{H}$

Table 1.3: Particle spectrum of the MSSM.

In analogy to the mixing of the B and W^0 bosons to photon and Z boson as mass eigenstates, the $\tilde{B}$, $\tilde{W}^0$ and neutral Higgsinos mix to give four neutralinos as mass eigenstates ($\tilde{\chi}_i^0$, $i = 1, \cdots, 4$) and the $\tilde{W}^\pm$ and charged Higgsions mix to two charginos ($\tilde{\chi}_i^\pm$, $i = 1, 2$) as mass eigenstates.

In the MSSM Lagrangian new terms exists that violate lepton or baryon number. Baryon- and lepton number violating processes are severely constrained by experimental data, e.g. by measurements of the proton lifetime. Therefore many models (including the MSSM) introduce an additional quantum number, R-parity, to force baryon- and lepton-number conservation. R-parity is defined as $R_p = -1^{3(B-L)+2S}$. By definition all particles of the Standard Model have $R_p = 1$ and all superpartners have $R_p = -1$. $R-$parity conservation has the following consequences:

- supersymmetric particles can only be produced in pairs;

- supersymmetric particles can only decay into an odd number of SUSY particles;

- the lightest supersymmetric particle (LSP) must be stable.

The last fact leads directly to a possible solution of the dark-matter problem in the Standard Model. If the LSP is only weakly interacting it is a perfect dark-matter candidate. Another problem of the Standard Model has an elegant solution in SUSY. Since fermions and bosons contribute with different signs in the radiative corrections to the Higgs boson mass, the contributions from Standard Model particles and their SUSY partners cancel and the "hierarchy problem" is solved in a natural way. This holds only if particles and their SUSY partners have the same masses. But SUSY must be a broken symmetry. Otherwise SUSY would have been discovered already. The masses of SUSY particles need to be restricted to $m_{\mathrm{SUSY}} \lesssim 1\,\mathrm{TeV}$, if a cancellation of the fermionic and bosonic contributions to the Higgs-boson mass is required. Thus if SUSY is realized in nature should be discovered at the LHC.

The missing knowledge of the mechanism that introduces the symmetry breaking must be compensated by adding a great (> 100) number of free parameters to the MSSM model. Since the resulting parameter space is too big to scan for SUSY analyses, simplifying assumptions about the SUSY breaking mechanism must be made. One of the most common models is called "mSUGRA" (minimal SUperGRAvity). It describes the symmetry breaking as being mediated by the gravitational interaction and unifies all gaugino masses, all scalar masses and trilinear couplings at the GUT scale. This yields four free parameters and a free sign. The mSUGRA parameters are listed in Tab. 1.4. The LSP in mSUGRA is the lightest neutralino $\tilde{\chi}_1^0$.

Parameter	Description
$m_{1/2}$	common gaugino mass at the GUT scale
m_0	common scalar mass at the GUT scale
A_0	trilinear scalar coupling at the GUT scale
$\tan\beta$	ratio of the Higgs vacuum expectation values
$\text{sign}\,\mu$	sign of the Higgsino mixing parameter

Table 1.4: The four free parameters and the free sign of the mSUGRA model of supersymmetry.

For SUSY analyses with tau leptons the ratio of the Higgs vacuum expectation values, $\tan\beta = \langle H_u \rangle / \langle H_d \rangle$, is an important parameter. If it is large the coupling of neutralinos and charginos to tau leptons is enhanced. For large $\tan\beta$ the electron and muon channels may be "closed", i.e. the branching ratios of neutralino and chargino decays with electrons or muons may be very small, and tau leptons are the only available leptons to study the decay of SUSY particles.

1.3 Tau Leptons at the Large Hadron Collider

1.3.1 Tau Leptons in First Data

$Z \to \tau^\pm \tau^\mp$ and $W^\pm \to \tau^\pm \nu_\tau$ decays will be the main source of tau leptons for first data at the LHC. The tree level diagrams for th production of W- and Z bosons are shown in Fig. 1.3. In first data corresponding to an integrated luminosity of $100\,\text{pb}^{-1}$, about 1.7 million $W^\pm \to \tau^\pm \nu_\tau$ and 70000 $Z \to \tau^\pm \tau^\mp$ events are expected. These events can be used to study the tau-lepton reconstruction efficiency and performance with real data. In addition for $Z \to \tau^\pm \tau^\mp$ decays the Z mass can be reconstructed and a Z-mass constraint can be used to calibrate the tau energy scale. The reconstruction of the Z-mass is not straightforward, since the neutrinos from the tau-lepton decay will escape the detector undetected. Thus the Z-mass has to be reconstructed in the so-called collinear approximation, which assumes that the neutrinos have the same direction as the tau-leptons, which is a good approximation for large enough tau-lepton momenta. The missing energy and the direction of the neutrinos is used to obtain their energies, E_{ν_1} and E_{ν_2}. The mass of the Z boson can then be calculated as $m_Z \approx \sqrt{2\left(E_{\tau_1} + E_{\nu_1}\right)\left(E_{\tau_2} + E_{\nu_2}\right)\left(1 - \cos\alpha\right)}$. Here α denotes the angle between the two tau-jets and E_{τ_1}, E_{τ_2} their energies. A tau-jet is defined as the particles of the tau-lepton decay visible in the detector (i.e. all particles except the neutrinos).
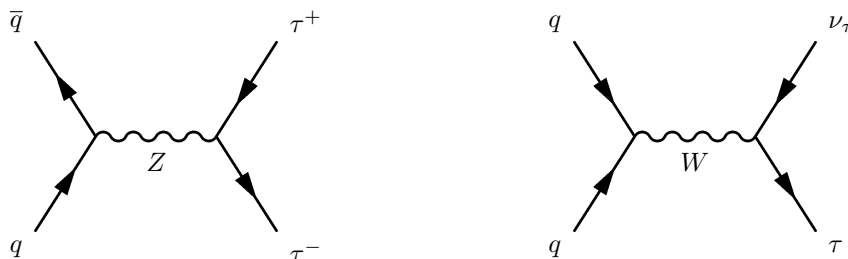
Figure 1.3: Tree level diagram for $q\bar{q} \to Z \to \tau\tau$ and $q\bar{q}\prime \to W \to \tau\nu_\tau$ processes.

1.3.2 Tau Leptons for Higgs and SUSY discoveries

An important Standard Model process involving tau leptons as a promising final state is the Standard Model Higgs boson decay $H \to \tau^{\pm}\tau^{\mp}$ as the Higgs boson couples to mass and the tau lepton is the heaviest lepton. The vector-boson-fusion Higgs production process $qqH \to qq\tau\tau$ yields a final state with two quark-jets at small angles ("forward jets") in addition to the two tau leptons as a promising signature. For Higgs boson masses around 120 GeV this signature has a 5σ discovery potential[4] [5]. In the MSSM Higgs sector the decays $H/A \to \tau\tau$ and $H^{\pm} \to \tau\nu$ are the most promising decay channels for large $\tan\beta$, e.g. for $\tan\beta \gtrsim 10$ the decay $H^{\pm} \to \tau^{\pm}\nu_\tau$ has a branching fraction of about $10\,\%$. The dominant decay mode $H^{\pm} \to t\bar{b}$ suffers from large background by Standard Model QCD processes [6].

Apart from the fact that for large $\tan\beta$ the tau lepton may be the only lepton resulting from SUSY decays, the tau-lepton can also be used get information about the SUSY breaking mechanism. Only particles of the third generation have an observable mixing between left- and right-handed eigenstates. Eq. 1.2 shows the mixing between left- and right-handed staus leading to two different mass eigenstates, $\tilde{\tau}_1$ and $\tilde{\tau}_2$. $M^2_{\tilde{\tau}_{L/R}}$ denote the mass of the staus, m_τ the mass of the tau lepton, θ_W the "Weinberg angle", A_τ the trilinear coupling for the tau lepton and M_z the mass of the Z-boson. Measuring the mass splitting between $\tilde{\tau}_1$ and $\tilde{\tau}_2$ yields information about SUSY parameters and the SUSY breaking mechanism.

$$\begin{pmatrix} \tilde{\tau}_1 \\ \tilde{\tau}_2 \end{pmatrix} = M_{\tilde{\tau}} \begin{pmatrix} \tilde{\tau}_L \\ \tilde{\tau}_R \end{pmatrix} \tag{1.2}$$

with

$$M_{\tilde{\tau}} = \begin{pmatrix} M^2_{\tilde{\tau}_L} + m^2_\tau + M^2_Z \cos 2\beta \left(-\frac{1}{2} + \sin^2 \theta_W\right) & m_\tau \left(A_\tau - \mu \tan\beta\right) \\ m_\tau \left(A_\tau - \mu \tan\beta\right) & M^2_{\tilde{\tau}_R} + m^2_\tau - M^2_Z \cos 2\beta \sin^2 \theta_W \end{pmatrix} \tag{1.3}$$

SUSY predicts long decay cascades with leptons mostly towards the end of the decay chain, which come from decays of neutralinos and charginos (illustrated in Fig. 1.4). Thus the identification of tau leptons with relatively low transverse momenta will play an important role. In addition a part of the "mSUGRA" parameter space favored by cosmological dark matter constraints, the so called "Stau-Neutralino-Co-annihilation" region, yields the stau as

---

[4]Assuming $30\,\mathrm{fb}^{-1}$ and a branching fraction to tau leptons on the order of a few percent.

next-to-lightest supersymmetric particle (NLSP) with a very small mass difference of possibly as low as $5 - 15$ GeV to the LSP. In this scenario tau leptons from the stau decay are expected to have small transverse momenta. This necessitates a reliable and efficient reconstruction of tau leptons for low transverse momenta.
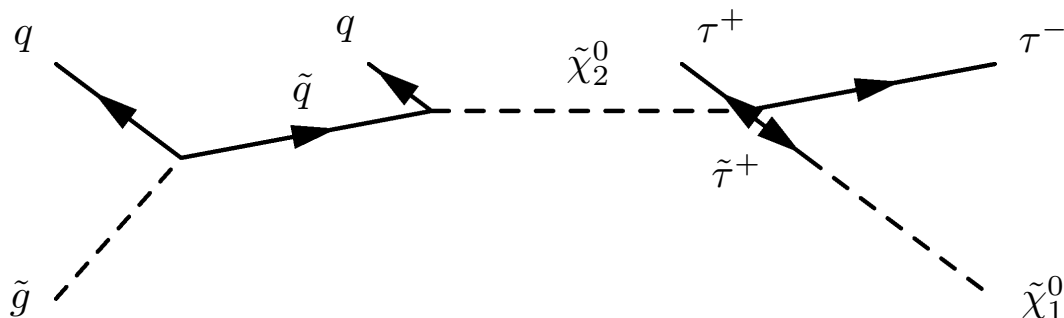
Figure 1.4: An example of a SUSY decay chain of a gluino $\tilde{g}$ decay in mSUGRA resulting in tau leptons.

1.4 Properties of Tau Leptons and Decay Kinematics

The tau lepton was discovered in 1975 [7] by M. Perl and his colleagues with the electron-positron collider SPEAR at the Stanford Linear Accelerator Center (SLAC). The Nobel Prize for physics was awarded to him "for the discovery of the tau lepton" in 1995. It is the heaviest lepton known to date. The currently best known value of the tau lepton mass is $m_\tau = 1776 \pm 0.17$ MeV and the mean lifetime is $\tau_\tau = 290.6 \pm 1.0$ fs, yielding a decay length of $c\tau = 87.11\,\mu$m [8].

The following sections will introduce the tau-lepton decay and its kinematic properties. At the end, the use of tau-lepton polarization studies for physics analyses is briefly discussed.

1.4.1 Tau Lepton Decays

In contrast to the lighter leptons, the tau lepton masses exceeds the mass of the lightest mesons. Hence it decays into leptons ($\tau^- \to l^- \overline{\nu}_l \nu_\tau$ and hadrons ($\tau^- \to \text{hadrons}\,\nu_\tau$). The Feynman diagrams for these decays are shown in Fig. 1.5.

The tau-lepton decays can be classified by counting the number of charged particles (charged pions or kaons) resulting from the decay. In theory the creation of up to twelve particles, thereof eleven charged ones, is possible [9], but this case is extremely rare. The most common decays have one or three charged particles. Up to now, five prong[5] decays have been

---

[5] "Prong" denotes the tracks associated with the tau lepton decay.
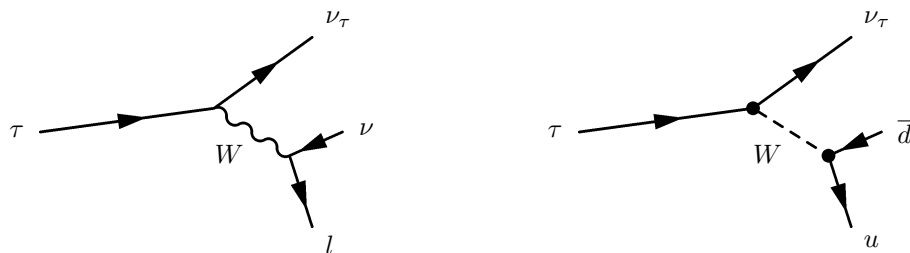
Figure 1.5: Feynman diagrams of a leptonic (left) and a hadronic (right) tau lepton decay.

observed (e.g. at LEP) and limits for seven prong decays are available [10]. A listing of the branching ratios of tau-lepton decays is given in Tab. 1.5.

category	decay mode	branching fraction[%]
	$\tau \rightarrow e \nu_e \nu_\tau$	17.85 ± 0.05
single prong	$\tau \rightarrow \mu \nu_\mu \nu_\tau$	17.36 ± 0.05
	$\tau \rightarrow h \geq 0 \, \text{neutrals} \, \nu_\tau$	50.15 ± 0.12
three prong	$\tau \rightarrow hhh \geq 0 \, \text{neutrals} \, \nu_\tau$	15.18 ± 0.08
five prong	$\tau \rightarrow 5h \geq 0 \, \text{neutrals} \, \nu_\tau$	0.102 ± 0.004
seven prong	$\tau \rightarrow 7h \geq 0 \, \text{neutrals} \, \nu_\tau$	$< 3.0 \cdot 10^{-5}$

Table 1.5: Tau lepton branching ratios for one-, three- or five-prong decays. Here h denotes either a charged pion or a charged kaon and "neutrals" stands for neutral pions or photons. All values are given in percent and taken from [8].

A closer look at the hadronic one-prong decay modes of the tau lepton shows some interesting features of these decays. The branching fraction for tau-lepton decays with a charged kaon is much smaller than the branching fraction for decays with a charged pions. Decays with charged pions proceed predominantly via an intermediate ρ or a_1 resonance. The number of neutral pions in the final state are an indication of the intermediate resonance – if any – in the decay. Tab. 1.6 shows that final states of hadronic tau-lepton decays with one charged and one neutral pion mostly originated from the ρ resonance. The same holds for the a_1 resonance which either decays into three charged pions or one charged and two neutral pions. A sketch of a tau-lepton decay into three charged and one neutral pion is shown in Fig. 1.6.

1.4.2 Kinematic Properties of Hadronic Tau-Lepton Decays

The hadronic tau-lepton decays, i.e. $\tau \rightarrow \text{hadrons} \, \nu_\tau$, can be described as two body decays into the neutrino and a hadronic resonance. For the decay kinematics it is not relevant, wheter the hadronic decay products formed a resonance or not. In the rest frame of the tau lepton, the kinematics of its decay are completely determined by energy and momentum conservation. If the neutrino mass is neglected, the energy and momentum of the hadronic

decay mode	branching fraction[%]
$\tau \to h\nu_\tau$	11.60 ± 0.06
$\tau \to \pi\nu_\tau$	10.91 ± 0.07
$\tau \to h\pi^0\nu_\tau$	25.95 ± 0.10
$\tau \to \rho\left(\to \pi\pi^0\right)\nu_\tau$	25.52 ± 0.10
$\tau \to h\pi^0\pi^0\nu_\tau$	10.84 ± 0.12
$\tau \to a_1\left(\to \pi\pi^0\pi^0\right)\nu_\tau$	9.27 ± 0.12

Table 1.6: Hadronic single-prong decay modes of the tau lepton. The fact that the intermediate resonance defines the number of neutral pions is of special interest to this study. The branching fractions are taken from [8].
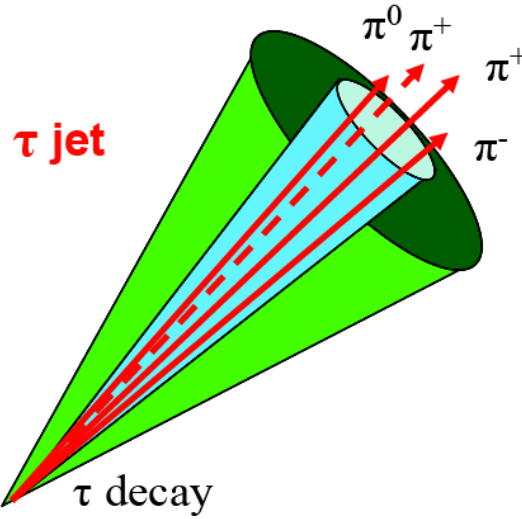
Figure 1.6: Sketch of a tau lepton decaying into three charged and one neutral pion.

Tau-Lepton E$_T$ and E$_T^{vis}$ spectrum
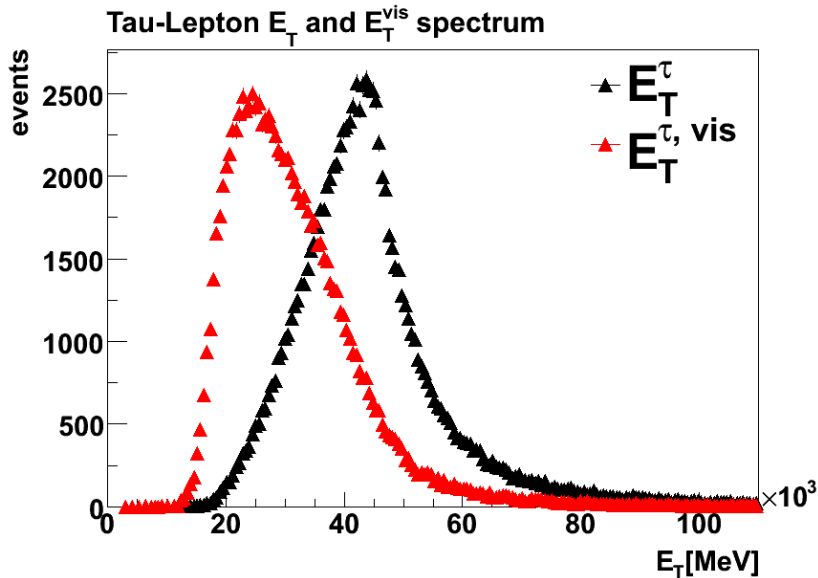
Figure 1.7: Transverse energy and visible transverse energy of tau-leptons from the $Z \to \tau^{\pm}\tau^{\mp}$ sample used in this study. The selection of the data sample is described in Section 4.3.

decay products in the rest frame of the tau lepton is given by

$$
\begin{aligned}
E_{\text{had}} &= \frac{m_\tau^2 + m_{\text{had}}^2}{2m_\tau} \\
p_{\text{had}} &= \frac{m_\tau^2 - m_{\text{had}}^2}{2m_\tau} \ .
\end{aligned}
\tag{1.4}
$$

The energy of the hadronic decay products in the laboratory frame, depends on their emission angle with respect to the direction of the Lorentz boost into the laboratory frame.

The transverse energy, E_T, and the so-called "visible transverse energy", E_T^{vis}, of the tau lepton from the $Z \to \tau^{\pm}\tau^{\mp}$ signal sample obtained as described in Section 4.3 are shown in Fig. 1.7. The visible energy is defined as the energy of the tau lepton which can be measured with the detector, i.e. the energy of all tau-lepton decay products apart from the neutrinos. Fig. 1.8 shows the transverse energy of the charged and neutral pions from $\tau^{\pm} \to \rho^{\pm}\nu_\tau$ and $\tau^{\pm} \to a_1^{\pm}\nu_\tau$ decays from the same data sample as above. In addition the charged pion energy from $\tau^{\pm} \to \rho^{\pm}\nu_\tau$ decays is shown. The energy of the charged and neutral pions decreases as the particle multiplicity increases, since the energy must be split among all particles.

1.4.3 Tau-Lepton Polarization

The tau-lepton polarization, P_τ, affects the kinematic distributions of the tau-lepton decay products [11]. Thus determining the tau-lepton polarization can be useful for physics analyses, e.g.:

- P_τ can be used to suppress Standard Model background in MSSM Higgs searches [12]. This is possible since the decay $H^- \to \tau_R^- \bar{\nu}_R$ results in $P_\tau = +1$ while the main SM backgrounds give $P_\tau = -1$ (tau-lepton from a $W^- \to \tau \bar{\nu}_R$ decay).
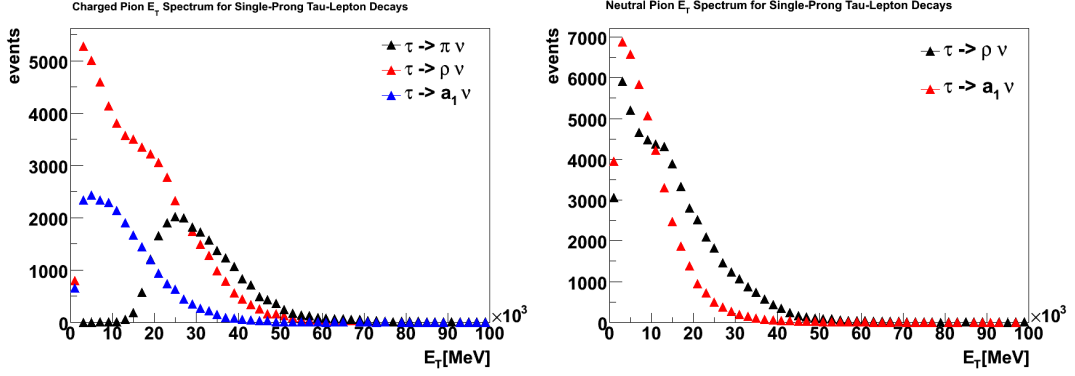
Figure 1.8: Transverse energy of charged pions from $\tau^{\pm} \to \pi^{\pm}\nu_{\tau}$, $\tau^{\pm} \to \rho^{\pm}\nu_{\tau}$ and $\tau^{\pm} \to a_1^{\pm}\nu_{\tau}$ decays and neutral pions from $\tau^{\pm} \to \rho^{\pm}\nu_{\tau}$ and $\tau^{\pm} \to a_1^{\pm}\nu_{\tau}$ decays obtained with the $Z \to \tau^{\pm}\tau^{\mp}$ sample used in this study.

- Measuring P_{τ} provides information on SUSY couplings, because the average tau-lepton polarization in the decay $\tilde{\chi}_2^0 \to \tilde{\tau}_1\tau \to \tau\tau\tilde{\chi}_1^0$ depends on the couplings between τ, $\tilde{\tau}_1$ and $\tilde{\chi}_j^0$ [13].

- The tau-lepton polarization affects angular distributions of decays with tau leptons, which need to be studied to determine the spins of SUSY particles.

Polarization effects depend on the tau-lepton decay mode. While the $\tau^{\pm} \to a_1^{\pm}\nu_{\tau}$ decay is insensitive to polarization, the $\tau^{\pm} \to \pi^{\pm}\nu_{\tau}$ decay shows the highest sensitivity to P_{τ}. Therefore polarization-dependent analyses profit from the ability to distinguish the different hadronic single-prong decays [13]. The neutral pion reconstruction presented in this thesis facilitates the distinction between these decay channels.

Chapter 2

The ATLAS Experiment at the Large Hadron Collider

2.1 The Large Hadron Collider

In 2009 the LHC at the European Organization for Nuclear Research (CERN) in Geneva will record first collision data. At the LHC two counter-rotating proton or heavy ion beams with an energy of 7 TeV and 5.5 TeV each will be collided at four interaction points. Each interaction point houses one of the four experiments installed at the LHC.

ALICE "A Large Ion Collider Experiment at CERN LHC" is build to study heavy ion collisions.

ATLAS "A ToroidaL LHC AppartuS" and **CMS** "The Compact Muon Solenoid Experiment" are multipurpose detectors.

LHCb "The Large Hadron Collider beauty experiment" is designed for precise measurements of CP violation and rare B-meson decays.

An overview of the LHC and its experiments is given in Fig. 2.1.

The LHC was build in the existing LEP tunnel which lies around 100 m below the surface and has a circumference of 27 km. In order to keep the protons on track for such high energies exceptional high magnetic fields of up to 8.33 Tesla are needed. These are created by 1232 superconducting dipole magnets at a temperature of 1.9 K and another 386 quadrupole magnets provide beam focusing.

Before injection into the LHC the protons are accelerated to 450 GeV using the existing Super Proton Synchrotron (SPS). Then eight superconducting cavities accelerate the beams to 7 TeV and compensate the energy loss due to synchrotron radiation. At the design luminosity of $10^{34} \frac{1}{\text{cm}^2 \text{s}}$ The proton beams are split into 2808 so-called "bunches" with $\approx 10^{11}$ protons each. The length of a bunch is 7.5 cm in beam direction and they have a diameter of 16.7 μm. The spacing between two bunches is 7.5 m and a so-called "bunch crossing" will happen every 24.95 ns yielding on average 23 inelastic proton-proton interactions at design luminosity.

2.2 The ATLAS Experiment

The discovery of the Higgs boson, if it is realized in nature, and the search for physics beyond the Standard Model make great demands on a detector. It must be able to measure many different final state objects like photons, electrons, muons, tau leptons, jets and missing
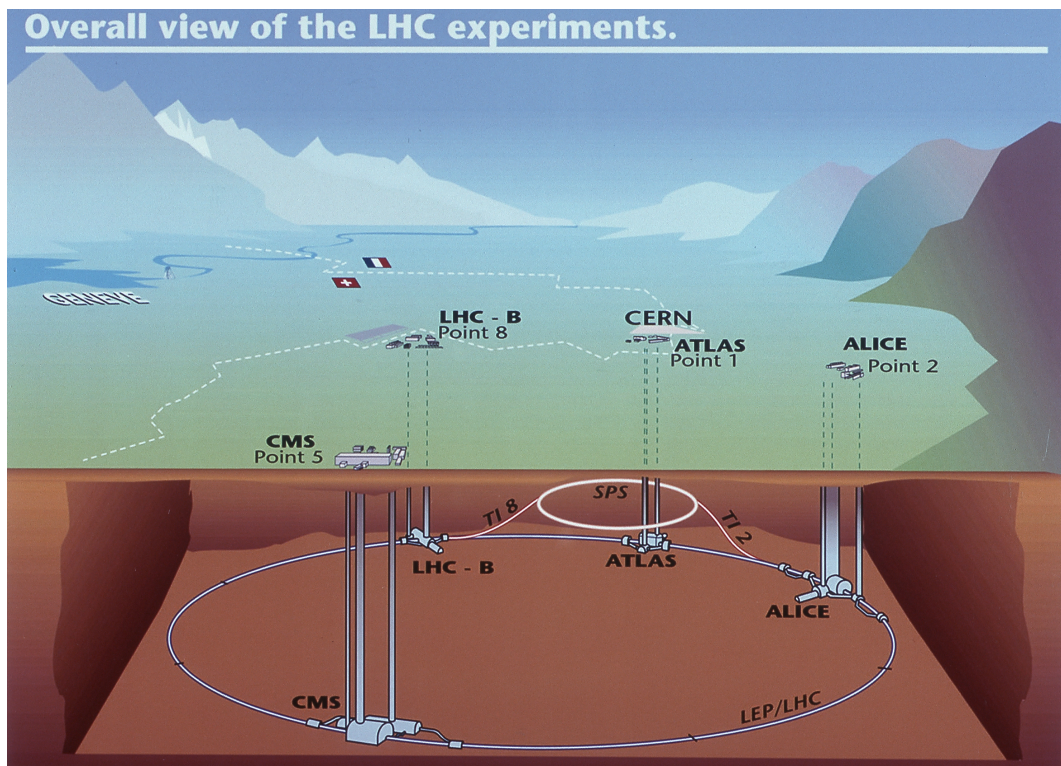
Figure 2.1: Overview of the Large Hadron Collider and its four experiments [14].

transverse energy with decent precision and over a wide kinematic range. These requirements lead to the following criteria for the ATLAS detector:

- A good tracking system with a strong magnetic field and a high granularity to precisely measure tracks of high p_T particles.

- Good resolution and coverage in the electromagnetic and the hadronic calorimeters.

- A precise muon systems which allows tracking and momentum measurements of muons.

- A high-performance trigger system to select interesting events.

The ATLAS detector is shown in Fig. 2.2. It weights 7 000 tons and is 45 meters long and 25 meters high. The detector consists of the following four subsystems:

- The **Inner Detector** is used to measure tracks of charged particles. A strong magnetic field provided by a solenoid magnet bends the particles and the measurement of the curvature can be used to reconstruct the transverse momenta of the charged particles.

- The **Calorimeters** are used to measure the energy of the particles produced in the p-p collisions. The calorimeter system consists of an electromagnetic, a hadronic and a forward calorimeter. The electromagnetic calorimeter is designed to measure electron and photon energies, whereas hadron energies are measured in both the electromagnetic and the hadronic calorimeter.

- The **Muon System** is the outermost detector subsystem measuring tracks from muons bent by a large superconducting toroid magnet. It was designed to provide a transverse momentum resolution σ_{p_T}/p_T of 10 % for muons with $p_T = 1\,\text{TeV}$. To reach this precision, a precise alignment of the tracking chambers is mandatory. The alignment is tested using 12 000 built-in optical sensors.

- The **Trigger System** must reduce the expected data rate of $\approx 60\,\text{TByte/s}$ to a rate that can be handled by permanent storage ($\approx 300\,\text{MByte/s}$) without rejecting interesting events. This is achieved using three stages of triggers, a Level-1 hardware trigger, a Level-2 software trigger and an event filter, each refining the decision of the previous stage and applying additional selection criteria.

Since the inner detector and the calorimeter system are of special interest for the work presented in this thesis, a more detailed description of them will be given in the following sections. Beforehand the coordinate system used at the ATLAS experiment will be introduced. A detailed description of the detector and all of the subsystems can be found in [15].

2.2.1 Coordinate System

The origin of the ATLAS coordinate system is defined as the nominal interaction point. The beam direction defines the z-axis, while the x-y plane is perpendicular to the beam axis, with the x-axis pointing to the center of the LHC ring. The azimuthal angle, ϕ, is measured in the x-y plane around the beam axis and the polar angle, θ, is measured from the beam axis. The transverse energy, $E_T = E \sin \theta$, transverse momentum, $p_T = \sqrt{p_x^2 + p_y^2}$, and the transverse
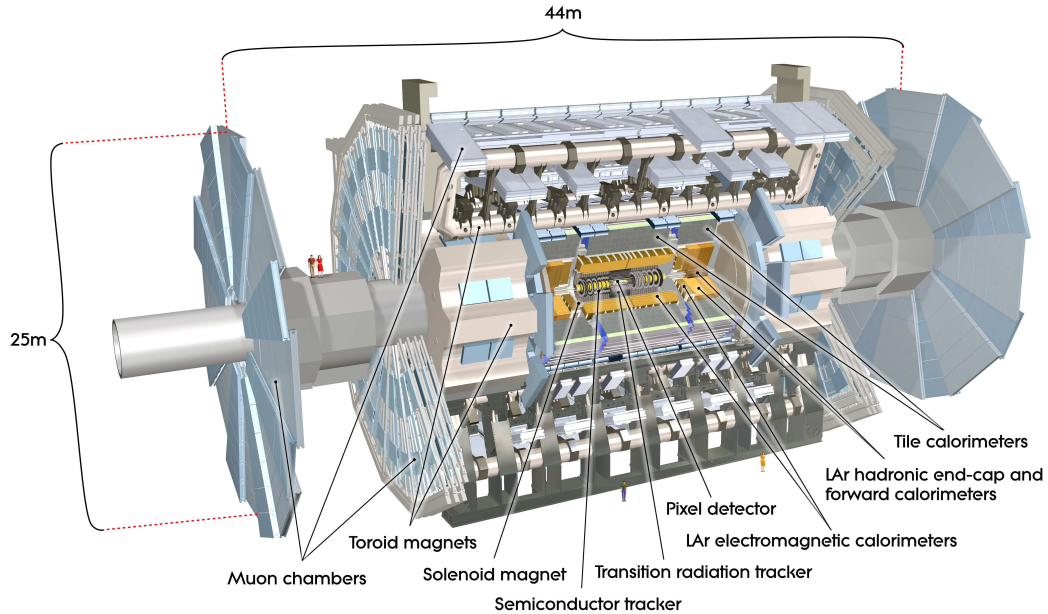
Figure 2.2: The ATLAS detector [15].

missing energy, E_T^{miss}, are defined in the x-y plane. The pseudorapidity, η, is defined as $\eta = -\ln\left(\tan\left(\frac{\theta}{2}\right)\right)$ and the distance in pseudorapidity-azimuthal angle space, ΔR, is defined as $\Delta R = \sqrt{\Delta\eta^2 + \Delta\phi^2}$.

2.2.2 Inner Detector

The inner detector is used to measure tracks of charged particles. These tracks can be used to measure the transverse momentum and direction of the particles and allow to reconstruct the primary vertex and additional secondary vertices. The tracking system is designed to cope with a very large track density, since ≈ 1000 particles will be produced every 25 ns. The inner detector is the innermost subsystem of the ATLAS detector and is installed next to the beam pipe. Its length is 6.2 m and it is 2.1 m high (see Fig. 2.3). The pixel and microstrip detectors cover the pseudorapidity range $|\eta| < 2.5$. To bend the charged particles in order to measure the transverse momentum a 2 T magnetic field created from the central solenoid is used.

The inner detector consist of three subsystems, which can be operated independently.

Semiconductor Pixel Detector : It is the innermost subsystem with the highest granularity consisting of three layers in the barrel and in the endcap. Its intrinsic resolution is $10\,\mu$m in R-ϕ and $115\,\mu$m in z for the barrel and R for the endcap pixels.

Silicon Microstrip Detector : Each track crosses eight silicon microstrip layers (SCT) yielding four space points per track. The intrinsic resolution is $17\,\mu$m in R-ϕ and $580\,\mu$m in z and R.

Transition Radiation Tracker : The Transposition Radiation Tracker (TRT) provides a large
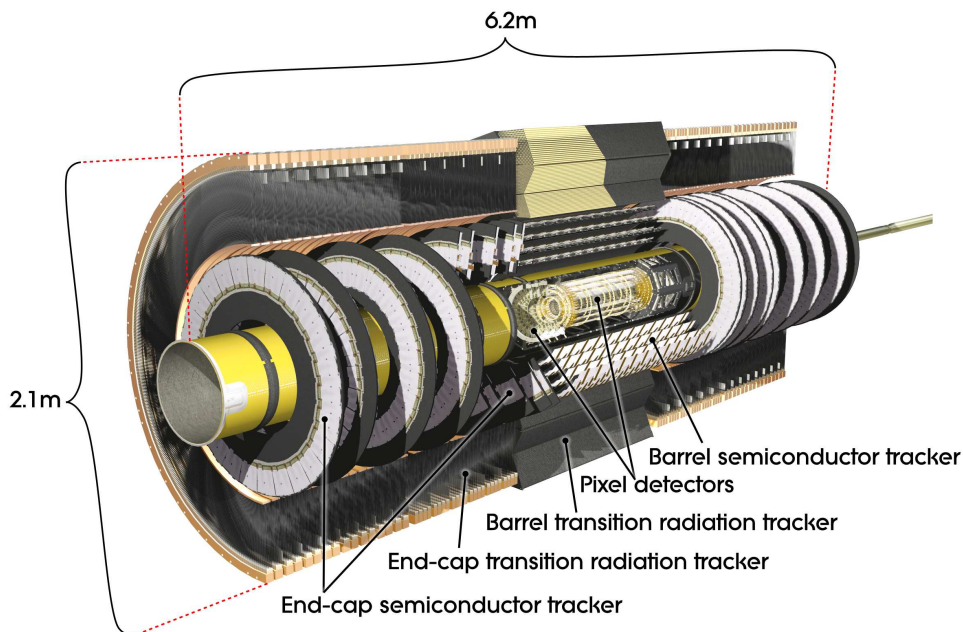
Figure 2.3: The ATLAS Inner Detector [15].

number of hits for each track up to $|\eta| = 2.0$. It consists of straw tubes with a diameter of 4 mm and provides only information about R-ϕ with an intrinsic resolution of 130 μm per straw. In addition, the amount of transition-radiation photons produced by charged particles that traverse the TRT are used for particle identification, in particular to separate electrons from pions.

The data obtained from the three inner detector subsystems are used to reconstruct the direction and transverse momentum of charged particles. This is done in three steps:

1. Pre-processing: The raw data from the pixel detector and the SCT and the TRT timing information are turned into tracking clusters and drift circles.

2. Track Finding: Track-finding algorithm use the pixel and SCT data to find tracks originating from the interaction region. Then these tracks are extended to the TRT.

3. Post-processing: The available tracks are used to reconstruct the primary and secondary vertices as well as photon conversions.

Inner Detector Performance

The resolution of the transverse momentum measurement depends on the transverse momentum of the charged particle, since the curvature of the track due to the magnetic field decreases with higher transverse momenta. The inverse transverse-momentum resolution for muons obtained with the inner detector can be expressed as [15]

$$\sigma_{1/p_T} = 0.34 \, \text{TeV}^{-1} \cdot \left(1 \oplus \frac{44 \, \text{GeV}}{p_T} \right) \quad (2.1)$$

for the region $0.25 < |\eta| < 0.5$.

2.2.3 Calorimeter System

A overall view of the calorimeter system of the ATLAS detector is shown in Fig. 2.4. It covers the region $|\eta| < 4.9$. The region $|\eta| < 2.5$ which is also covered by the inner detector is devoted to high precision physics and was thus build with a fine granularity. The coarser granularity in the regions with $|\eta| > 2.5$ is sufficient to provide a reasonable precision for jet and E_T^{miss} measurements.
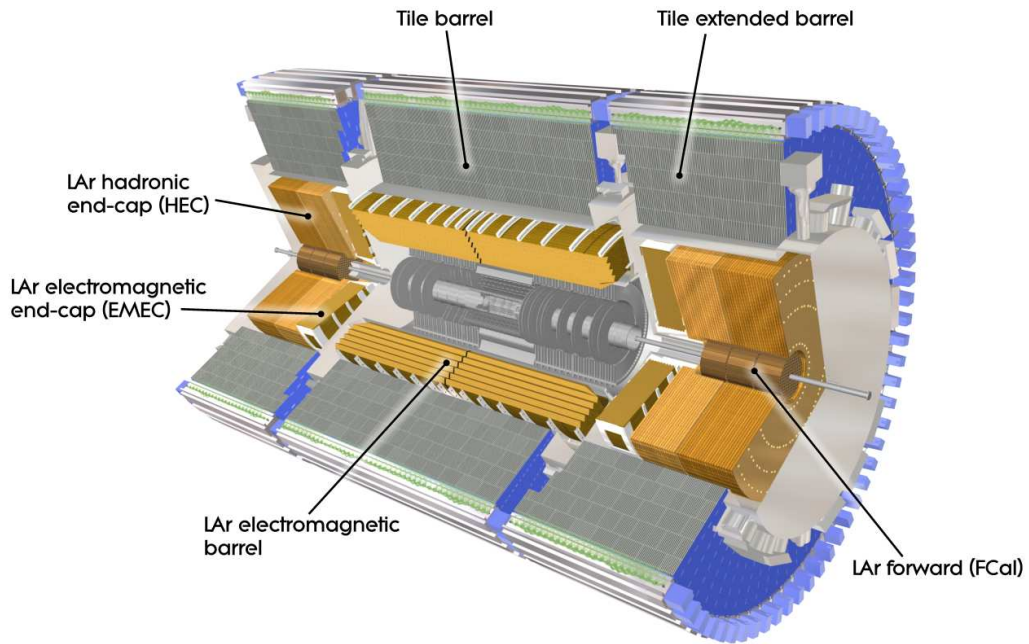
Figure 2.4: The ATLAS calorimeter system [15].

The complete calorimeter system consists of sampling calorimeters, which means that particle absorption and signal readout are separated. The primary particles interact with the absorber material and this results in cascade of secondary particles. These particles can be detected in the active material and yield a signal proportional to the energy deposited by the primary particle. Electrons and photons interact with the absorber material mainly via Bremsstrahlung and pair production whereas hadrons loose energy due to inelastic scattering with the nucleons of the absorber material. The deeper penetration of hadrons is the reason for the subdivision of the calorimeters into electromagnetic and hadronic ones.

In addition to the electromagnetic and the hadronic calorimeters in the central region, the forward calorimeter (FCAL) is installed in the region $3.1 < |\eta| < 4.9$. It uses liquid argon as active material and tungsten as passive one. Since tau-leptons are reconstructed only in the high-precision central region of the detector, the FCAL will not be discussed in more detail. The following two sections summarize the electromagnetic and the hadronic calorimeters and finally the expected performance of both is discussed.

The Electromagnetic Calorimeter

The electromagnetic calorimeter (ECAL) uses lead for absorption and liquid argon as active material. The absorber plates and the electrodes are accordion shaped to provide complete ϕ symmetry (see Fig. 2.5). The barrel region and the endcap consist of three layers each. In the region $|\eta| < 1.8$ a presampler is used to correct for the energy loss due to passive material between the interaction point and the calorimeters. The first layer of the ECAL, also called the "η-strips", has the highest granularity in η. The granularity of the electromagnetic-calorimeter layers for the $\eta = 0$ region are given in Tab. 2.1.
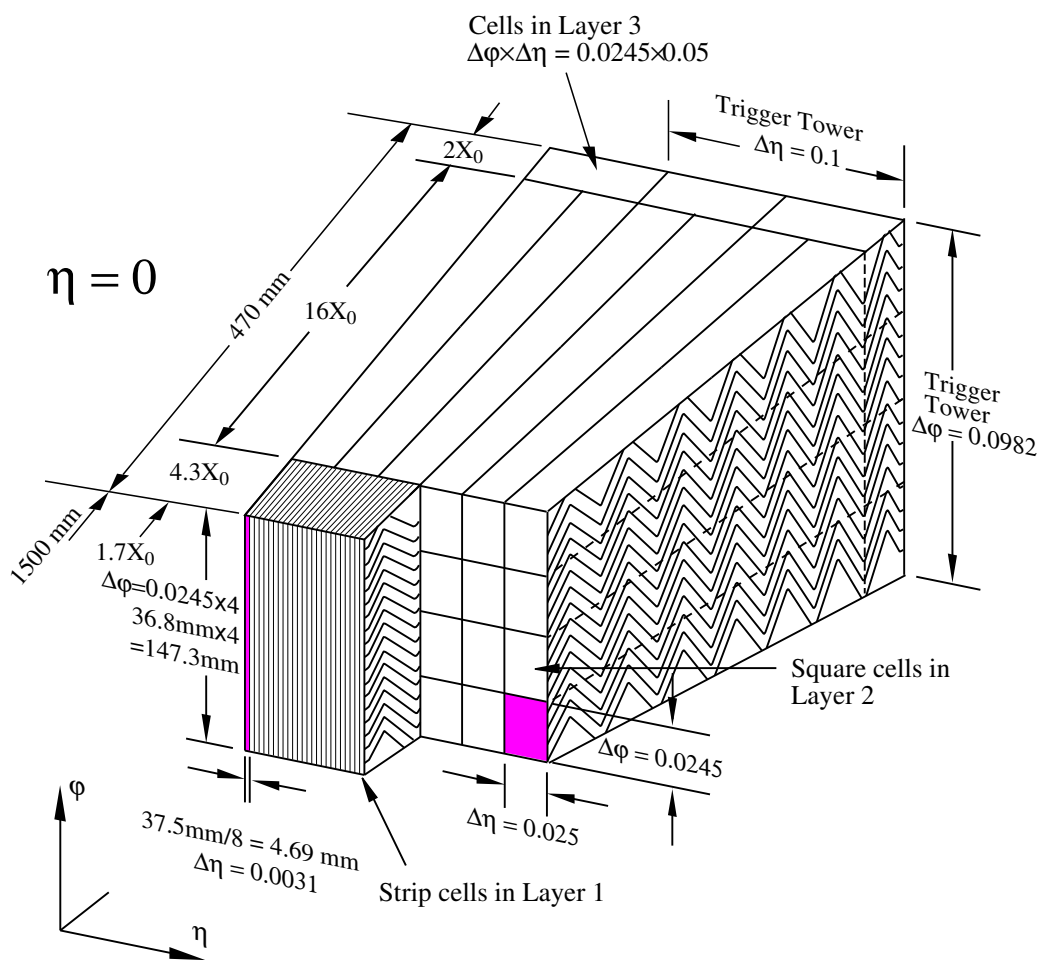
Figure 2.5: Sketch of the electromagnetic calorimeter showing the accordion-shaped architecture. In addition the granularity in η and ϕ and the longitudinal segmentation is shown [15].

The thickness of the ECAL corresponds to 22 radiation lengths (X_0) in the barrel region and $24X_0$ in the endcap. The radiation length, X_0, is the distance after which the energy of an electron drops to $\frac{1}{e}$ of its initial value. Thus the ECAL provides good containment for electromagnetically interacting particles, i.e. electrons and photons.

Electromagnetic Barrel

Layer	Granularity in $\Delta\eta \times \Delta\phi$
Presampler (PresamplerB)	0.025×0.1
1st layer (EMB1)	$0.025/8 \times 0.1$
2nd layer (EMB2)	0.025×0.025
3rd layer (EMB3)	0.025×0.05

Table 2.1: Granularity of the electromagnetic layers for the region $\eta = 0$.

Hadronic Calorimeter

The hadronic calorimeter (HCAL) is again split into the so-called "TileCal" and the "LAr hadronic endcap".

The TileCal consist of two parts, the central barrel covering the region $|\eta| < 1.0$ and an extended barrel covering $0.8 < |\eta| < 1.7$. Each barrel is radially segmented into three layers, which consists of 64 segments each. The segments have a size of $\Delta\phi \approx 0.1$ in the azimuthal direction. The granularity in the η-direction is $\Delta\eta = 0.1$ in the first two layers and $\Delta\eta = 0.2$ in the last one. The TileCal uses iron as absorber material and scintillator tiles as active material. Wavelength shifting fibers guide the photons from the scintillator material to photo-multiplier tubes, which are used for the readout (see. Fig. 2.6).

The LAr hadronic endcap is located directly behind the electromagnetic endcap calorimeter and uses liquid argon (LAr) as active and copper as passive material. It covers the region $1.5 < |\eta| < 3.2$ and is radially split into 4 layers. The granularity in $\Delta\eta \times \Delta\phi$ is 0.1×0.1 in the region covered by the inner detector and 0.2×0.2 otherwise.

The thickness of the hadronic calorimeter is 7.4 interaction lengths (λ) for the TileCal and the hadronic endcap. The interaction length is defined as the distance after which the energy of a hadron dropped to $\frac{1}{e}$ of its initial value. The total thickness of the calorimeter system is $11\,\lambda$ at $\eta = 0$. This is enough to reduce punch-through of hadronic showers into the muon system to an acceptable level.

Calorimeter Performance

The performance of the calorimeter has been tested using electron, muon and pion beams with energies between $1\,\text{GeV}$ and $250\,\text{GeV}$. The energy resolution of the calorimeters after noise subtraction was parametrized as follows [15]

$$\frac{\sigma(E)}{E} = \frac{a}{\sqrt{E\,(\text{GeV})}} \oplus b \; . \tag{2.2}$$

Here a is the stochastic term and b is a constant term reflecting non-uniformities in the calorimeter response.

The performance of the electromagnetic calorimeter has been tested using an electron beam. It yielded $a = 10.1\,\%\sqrt{\text{GeV}}$ and $b = 0.17\,\%$. In addition, the polar-angle resolution in the "η-strip" layer was measured. The high η-granularity allows a resolution of about $\frac{50\text{-}60(\text{mrad})}{\sqrt{E(\text{GeV})}}$.
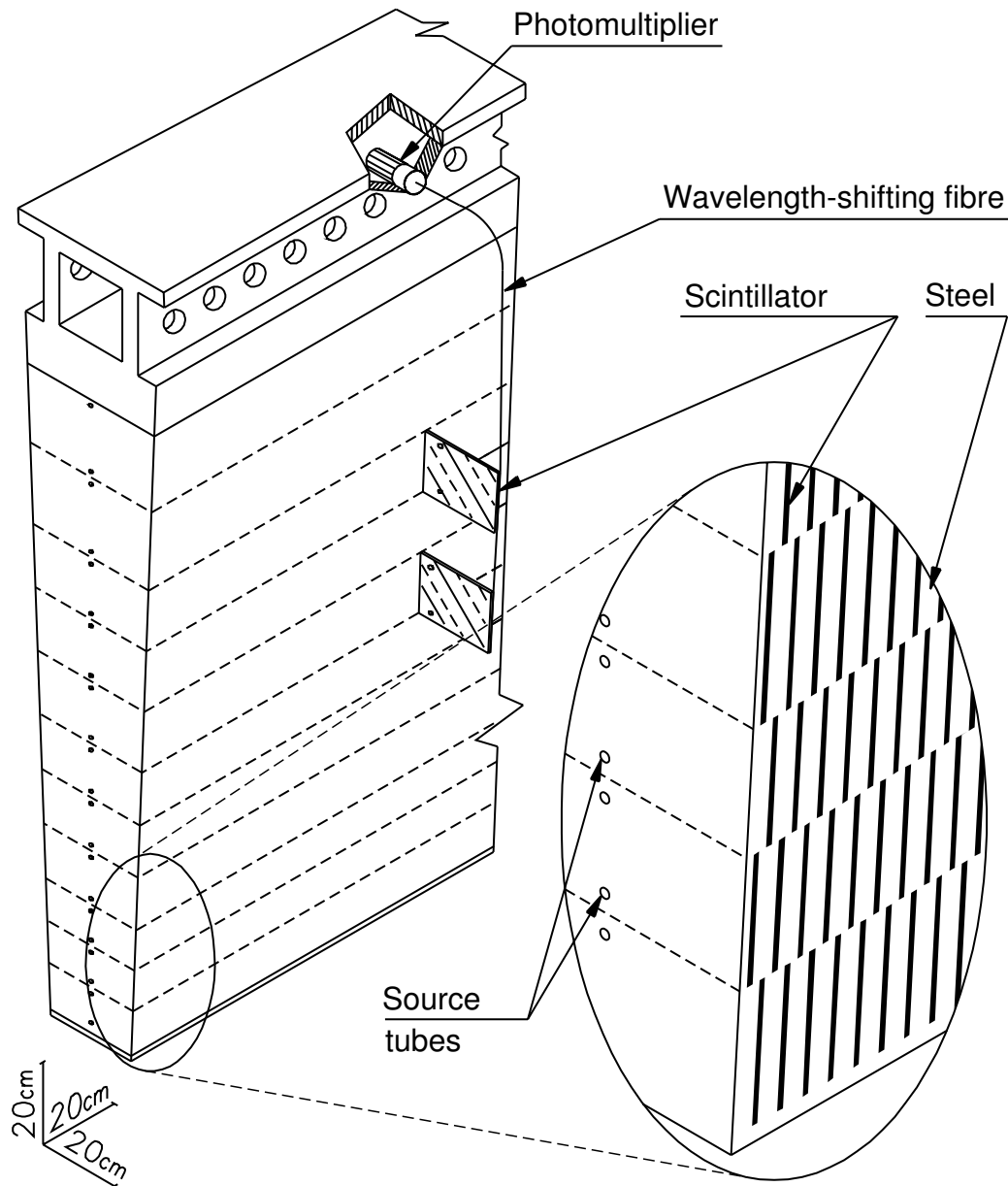
Figure 2.6: Schematic sketch of a TileCal segment. The components used for the readout are shown [15].

The energy resolution of the hadronic calorimeters was measured using charged pion beams. The hadronic endcap calorimeters yielded a stochastic term $a = (70.6 \pm 1.5)\,\%\sqrt{\text{GeV}}$ and a constant term of $b = (5.8 \pm 0.2)\,\%$. For the TileCal the resolutions are slightly better. The stochastic term is $a = (56.4 \pm 0.4)\,\%\sqrt{\text{GeV}}$ and the constant term $b = (5.5 \pm 0.1)\,\%$.

Calorimeter Calibration

The ATLAS calorimeter system is non-compensating, which means, that the response of the calorimeter to electromagnetic and hadronic interactions is different. This difference must be corrected by applying a factor, $f_{e/\pi}$, to the energy measurement of hadrons in order to reconstruct their correct energy. This study uses an calibration method proposed in [16]. It is based on a calibration developed for the H1-experiment ([17]), which applies a weight to the energy measurements of each single calorimeter cell. The weights depend on the cell's energy, pseudorapidity and the calorimeter layer: $f_{e/\pi} = f_{e/\pi}\,(E_{\text{cell}},\, \eta_{\text{cell}},\, \text{layer})$. On average the energy from hadrons is scaled up by $\approx 30\,\%$.

Chapter 3

Tau Lepton Reconstruction at the ATLAS Experiment

Tau-lepton decays into electrons or muons ($\tau \to e\nu_e\nu_\tau$ and $\tau \to \mu\nu_\mu\nu_\tau$) are basically indistinguishable from direct production of electrons or muons. That is why the tau-lepton reconstruction at that ATLAS experiment looks for hadronic tau-lepton decays. The signatures of hadronic tau-lepton decays are narrow jets in the calorimeter with a low particle multiplicity and few associated charged tracks. The main challenge of the tau lepton reconstruction is the suppression of the abundant jet background from QCD processes. This is done by studying jet shapes in the calorimeter and properties of the charged tracks in the tracking system.

This chapter summarizes the offline reconstruction of hadronically decaying tau leptons at the ATLAS experiment ("tauRec" software package [18]). This reconstruction is split into two distinct steps:

- tau-candidate reconstruction
- tau identification.

An overview of these two steps is given in the following sections. The neutral pion reconstruction presented in this thesis is designed to improve the identification of low tau leptons with low transverse momenta and thus must run in the framework of the tauRec package.

3.1 Tau-Candidate Reconstruction

The current implementation of TauRec has two different starting points (seeds) for tau reconstruction [19]:

- The "calo-seeded" approach uses jets in the calorimeter as seed.
- The "track-seeded" approach uses good quality tracks as seed.

Both approaches will be shortly summarized in the following:

"Calo seeded" approach: Jets in the calorimeter are used as tau seeds. The jets are formed by a cone algorithm with cone size $\Delta R = 0.4$ that runs over calorimeter clusters and is calibrated using an H1-style calibration (cf. Section 2.2). The direction and the energy of the tau jet is calculated using the calorimeter cells comprising the jet. The jet's transverse energy must exceed $10\,\mathrm{GeV}$ and it must be reconstructed within the pseudorapidity range $\eta \in [-2.5, 2.5]$). All tracks closer than $\Delta R = 0.3$ to the jet axis are associated to the tau jet if they fulfill basic quality requirements (see App. A.1).

"Track seeded" approach: A track with transverse momentum $p_T > 6\,\mathrm{GeV}$ which fulfills the seed quality criteria (all seed quality criteria used in the tauRec package are summarized in App. A.1) is the starting point for the "track-seeded" tau-lepton reconstruction. Other tracks within a cone of $\Delta R < 0.2$ are added to the tau candidate if they pass basic quality criteria (see App. A.1). If more than eight tracks are matched to the tau candidate or the sum of the charges q_i of all tracks, $Q = \sum q_i$, does not yield $|Q| = 1$ the tau candidate is dropped. In case only two tracks could be assigned to the candidate, some of the quality restrictions are relaxed in order to find a third track [19]. The energy of the tau candidate is calculated using an energy-flow algorithm [20], which was shown to reflect the visible tau-lepton energy well. The direction of the tau candidate is determined using tracking information. If more than one track is present, the transverse momentum barycenter of all associated tracks is used.

In the latest software release (release 14), a track- and a calo-seeded candidate are merged if their distance is less than $\Delta R = 0.2$, i.e. if they are suspected to be the same tau lepton. In the software release used for the study presented in this thesis (13.0.40) no merging was implemented. This study is carried out using only calo-seeded candidates. Please also note that in agreement with the ATLAS publication policy all plots and numbers shown for the tau-lepton reconstruction in this chapter are taken from an older release (release 12.0.6) of the reconstruction software, because they are the only public results [18]. Nevertheless, the plots from release 12.0.6 can give the reader an approximate picture of the current tau-lepton reconstruction and identification performance at the ATLAS experiment.

Fig. 3.1 shows the tau reconstruction efficiency, ϵ, defined as

$$\epsilon = \frac{\text{number of truth-matched tau candidates}}{\text{number of true taus}} \tag{3.1}$$

To check if a reconstructed tau candidate corresponds to a generated tau lepton, a so-called "truth-matching" method needs to be defined. In this case and throughout this thesis the truth matching is done geometrically. If a reconstructed tau candidate is closer than $\Delta R = 0.2$ to a generated tau lepton, the candidate is called "truth-matched". Only tau leptons with $E_T > 10\,\mathrm{GeV}$ and $\eta \in [-2.5, 2.5]$ are considered for Eq. 3.1.
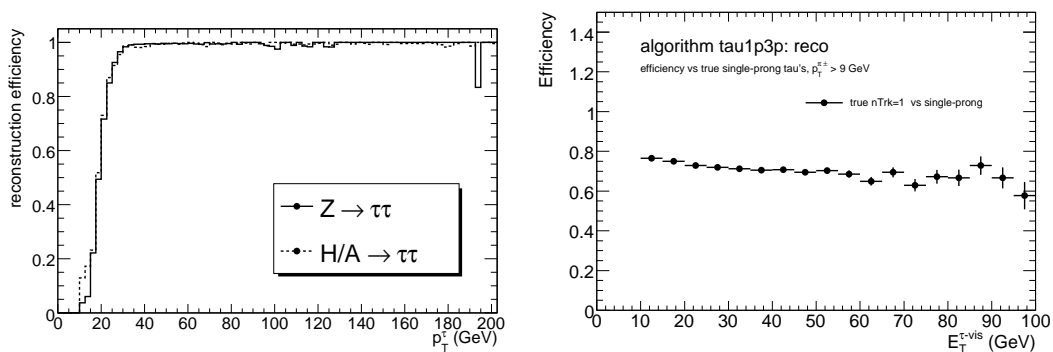
Figure 3.1: E_T dependence of the reconstruction efficiency for calo-seeded tau candidates on the left and track-seeded tau candidates on the right [18].

3.2 Tau-Lepton Identification

Tau identification and thus QCD rejection is done using a set of shower shape and tracking variables, for instance the isolation in the calorimeter or the number of associated charged tracks, calculated for each tau candidate. The list is of all variables is given in [18]. Multivariate analysis techniques, for instance a likelihood technique, are used to train a τ-identification discriminant using these variables as input. Fig. 3.2 shows the overall jet rejection versus tau-lepton identification efficiency as a function of the tau-lepton E_T obtained with a likelihood method.
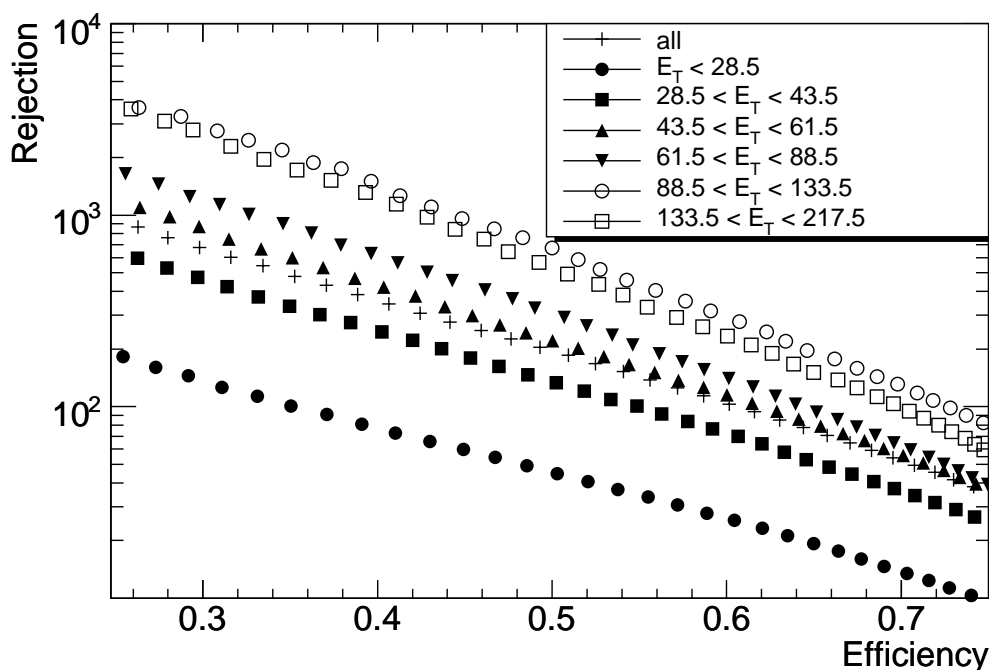
Figure 3.2: Jet rejection versus identification efficiency for calo-seeded tau candidates in different E_T intervals obtained with a likelihood discrimination method [18].

So far we looked only at the suppression of jets from QCD processes, but also tau candidates resulting from misidentification of electrons or muons must be suppressed. Mainly electrons fake a tau candidate. Therefore an additional electron veto is applied. It uses the fact, that electrons are contained in the electromagnetic calorimeter and that the track should roughly reflect the energy measured in the electromagnetic calorimeter. In addition the electron identification capability of the Transition Radiation Tracker (TRT) is used. About 2.5 % of all electrons from $W \to e\nu$ decays are reconstructed as tau candidates after the electron veto has been applied [18] and about 4.4 % of all hadronically decaying tau leptons from $W \to \tau\nu$ are rejected due to the electron veto.

3.3 Tau-Jet Substructure and Neutral Pion Reconstruction

So far the the tau identification only used jet shapes and tracking properties of the tau candidates. Studying the substructure of the tau jet will give additional information, that can be used to reject jet background. In particular the reconstruction of neutral pions is useful, since it gives access to the intermediate resonances of the tau-lepton decay (cf. Section 1.4.1).

Currently a basic neutral pion reconstruction is only implemented for the track-seeded approach. It is based on reconstructing clusters in the electromagnetic calorimeter that are not too close to a track. Before the clustering algorithm is run, cells with a distance less than $\Delta R = 0.0375$ to the track are rejected, as long as the total energy of the rejected cells does not exceed 70% of the track momenta. The rejection is done to remove decays with a significant overlap between the energy deposits from charged and neutral pions. A detailed description can be found in [18].

Only clusters with $E_T > 1\,\text{GeV}$ and more than 10% of their total energy in the first two layers of the electromagnetic calorimeter are accepted as neutral pions. The resulting reconstruction efficiencies are shown in Tab. 3.1.

tau-lepton decay	$0\,\pi^0$ rec.[%]	$1\,\pi^0$ rec.[%]	$\geq 2\,\pi^0$ rec.[%]
$\tau^\pm \to \pi^\pm \nu_\tau$	66.4	20.0	13.6
$\tau^\pm \to \pi^\pm \pi^0$	16.3	50.9	32.8
$\tau^\pm \to \pi^\pm 2\pi^0$	9.8	37.4	52.8

Table 3.1: Fraction of reconstructed neutral pions for single-prong tau candidates shown as function of the tau-lepton decay mode. The numbers are given with respect to tau-lepton decays with $p_T^\pi > 9\,\text{GeV}$ reconstructed as track-seeded candidate [18].

The neutral pion subcluster algorithm is used to improve the tau identification by training separate discriminants (see Section 3.2) for the following two categories:

- tau candidates with no neutral pion subclusters;

- tau candidates with one or more neutral pion subclusters.

Especially for low tau-lepton transverse momenta, this separate training of the τ-identification discriminant improves the suppression of background from QCD processes [18] and thus increases the signal purity. In this thesis a new algorithm for neutral pion subshower reconstruction is developed. It is based on a tau-lepton reconstruction algorithm that was developed at the H1-experiment [21, 22]. This algorithm aims at further improving the tau reconstruction efficiency and the identification of the tau-lepton decay mode. It is the first implementation of a neutral pion reconstruction for calo-seeded tau-lepton candidates. In contrast to the method presented above for the track-seeded approach, it allows for a reconstruction of neutral pion candidates that have energy depositions that overlap with those from charged particles in the tau-lepton decay.

Chapter 4

Datasets and Selection of Samples with Tau Leptons

Only Monte-Carlo simulated datasets are available at the time of writing, since the LHC is not operating yet. The following chapter first gives a short overview of the Monte-Carlo simulation procedure used in the ATLAS experiment. Then the datasets used in this study are presented and the selection of tau-lepton samples is discussed and some kinematic distributions are shown.

4.1 Monte-Carlo Simulation Procedure

The procedure used to create Monte-Carlo datasets consists of three steps:

1. event generation;

2. simulation of the interactions of the generated particles with the detector;

3. reconstruction.

For this study two different "Event Generators" are used to generate the physics processes. The first one simply creates single tau leptons with a given transverse momentum. The second one, simulates the $p\bar{p} \to Z \to \tau\tau$ process. For the latter the PYTHIA generator [23] is used, which takes into account many physics aspects such as hard and soft interactions, parton distributions on the protons and initial- and final-state parton showers. The tau-lepton decay are simulated by the TAUOLA decay generator [24].

The second step is to simulate the interaction of the final state particles with the detector material. This is done using the GEANT4 package [25]. The output of this step corresponds to the output of the various detector subsystems after a real event has been recorded (digitization step). The last step is to run the official reconstruction software, which reconstructs objects like tracks and clusters, on the output of the GEANT4 simulation. The same reconstruction software used for simulated and real data to make a comparisons between simulated and real data possible.

4.2 Dataset Selection

The development and the validation of the reconstruction algorithm for neutral pion subshowers are both completely based on Monte-Carlo simulation. Two different types of datasets are used in this study.

- A data sample of single-tau leptons, generated in the central region of the detector with a fixed transverse momentum and a random direction, is used for the development of the algorithm. It provides a clean (albeit "unphysical") environment, which simplifies the development. The single-tau samples are generated for $p_T^\tau = 20$, 50, and 100 GeV.

- A sample of $p\bar{p} \to Z \to \tau\tau$ is used to validate the algorithm, since it reflects the denser environment of real collisions better. Most likely, Z-decays will also be the best source of tau leptons in the first data taken by ATLAS.

All datasets used are for this study were generated assuming slightly misaligned detector components and include calorimeter noise. This is important since noise will affect the shower parameterizations of charged pions, which is used later in this work. All datasets are listed in Tab. 4.1. No dedicated background sample is needed, since both true and misidentified neutral pions can be taken from the same sample. The size of the $Z \to \tau^\pm \tau^\mp$ samples corresponds to an integrated luminosity of $\approx 400\,\mathrm{pb}^{-1}$.

Dataset Name	Generated Event	Events Available	Selections Applied
Single Tau[a]	τ	79000	$p_T^\tau = 20\,\mathrm{GeV}$
Single Tau[b]	τ	62500	$p_T^\tau = 50\,\mathrm{GeV}$
Single Tau[c]	τ	113500	$p_T^\tau = 100\,\mathrm{GeV}$
ZTauTau[d]	$p\bar{p} \to Z \to \tau^\pm \tau^\mp$	200000	$1.0 < \Delta\phi\,(\tau^\pm, \tau^\mp) < 3.1$ or $3.2 < \Delta\phi\,(\tau^\pm, \tau^\mp) < 5.3$

[a]Official name is: trig1_misal1_mc12.007600.SingleTaupt20.recon.ESD.v13004002
[b]Official name is: trig1_misal1_mc12.007602.SingleTaupt50.recon.ESD.v13004002
[c]Official name is: trig1_misal1_mc12.007604.SingleTaupt100.recon.ESD.v13004002
[d]Official name is: trig1_misal1_mc12_V1.005189.A3_Ztautau_filterA.recon.v13004002

Table 4.1: Datasets used for the neutral pion reconstruction algorithm. The single-tau samples are generated for three different transverse momenta. For $Z \to \tau^\pm \tau^\mp$, the selection criterion on $\Delta\phi$ rejects back to back tau-lepton candidates to suppress di-jet events from QCD processes.

4.3 Tau Sample Selection

A small set of selection criteria is applied to each event in the above mentioned datasets to avoid introducing unnecessary problems during the algorithm development. As mentioned in Section 3.1 only calo-seeded tau-lepton candidates are considered. The first criterion applied to each candidate found during reconstruction is, that it is truth-matched to a hadronically decaying tau lepton (cf. Section 3.1). This criterion is applied to develop the algorithm on a pure sample of tau leptons. In addition, only single-prong candidates are accepted. Single-prong decays have the largest branching fraction, and the presence of only one charged track simplifies the development of the neutral pion reconstruction. A later extension to multi-prong candidates is possible at any time. To avoid problems with tau candidates hitting both the electromagnetic barrel and endcap calorimeters at the same time, the tau candidate is restricted to $|\eta| < 1.0$. The extension to the electromagnetic endcap calorimeter should be straightforward (cf. Chapter 7). The resulting selection criteria for the tau lepton candidates are summarized in Tab. 4.2.

The selection criteria are passed by about 35 % of all tau lepton candidates found in the used datasets. This is mainly caused by the restriction to the central barrel which contributes a drop to about 40 %. The restriction on the number of tracks ($\approx 85\,\%$ of all tau leptons are one prong) and the truth match have less impact.

variable	selection criterion
$\Delta R\left(\tau_{\mathrm{gen}}, \tau_{\mathrm{rec}}\right)$	< 0.2
$\left|\eta_{\tau_{\mathrm{rec}}}\right|$	< 1.0
N_{tracks}	$= 1$

Table 4.2: Summary of the selection criteria applied to tau candidates used to develop the subshower algorithm.

4.4 Event Properties

In the following, properties of the tau leptons from both samples after applying the selection criteria are shown.

The E_T and the E_T^{vis} spectrum of the selected tau-lepton candidates is shown in Fig. 4.1. The selection efficiency for the single-tau sample with $p_T^\tau = 20\,\mathrm{GeV}$ is low, since the visible energy of the tau-lepton candidate lies significantly below the generated p_T^τ, i.e. in a region where the tau-lepton reconstruction efficiency is low. From now on only the $Z \to \tau^\pm \tau^\mp$ and the single-tau sample with $p_T^\tau = 50\,\mathrm{GeV}$ are used, since they cover a comparable visible E_T range from $\sim 15\ to 50\,\mathrm{GeV}$. This low to medium p_T^τ is well-suited for the development and validation of the reconstruction algorithm for neutral pions. The single-tau sample with $p_T^\tau = 100\,\mathrm{GeV}$ is later used for comparisons.
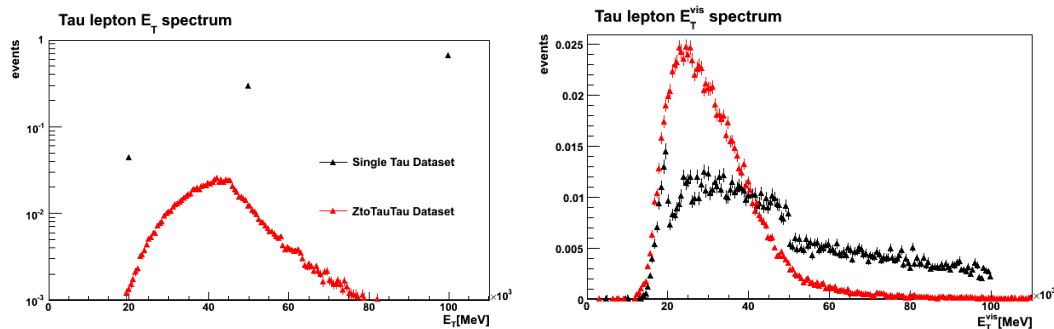
Figure 4.1: E_T and E_T^{vis} spectrum of selected tau leptons shown in black for the single tau samples and in red for the $Z \to \tau^\pm \tau^\mp$ sample. The step at around $50\,\mathrm{GeV}$ in the E_T^{vis} distribution of the single tau sample arises from the discrete tau lepton energies.

The transverse energy distribution of the charged pion and the neutral pion is shown in Fig. 4.2.

In addition to the E_T distributions of the tau leptons and their decay products, the distances between the charged and the neutral pion and between the photons from the neutral pion decay are of special interest for this study. The distance between the charged and the neutral pion is shown in Fig. 4.3. It reflects qualitatively the degree of overlap between energy
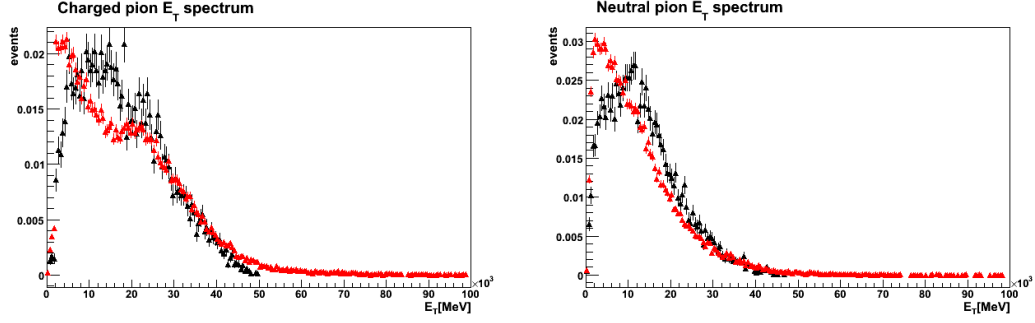
Figure 4.2: Transverse energy distribution of charged and neutral pions from a tau lepton decay for the single tau sample with $p_T^\tau = 50\,\mathrm{GeV}$ (black) and the $Z \to \tau^\pm \tau^\mp$ sample (red). Only tau leptons which fulfill the selection criteria mentioned above are considered.

deposited by the charged and the neutral pion. The probability of reconstructing a neutral pion as a single calorimeter clusters is given by the distance between the two photons from the neutral pion decay. The further away the two photons are from each other, the less likely it is that they build a single cluster in the calorimeter. The distance distribution is shown in Fig. 4.4.
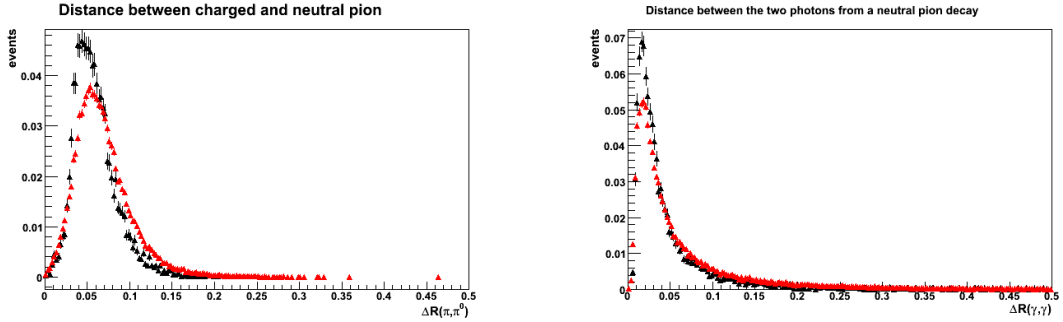
Figure 4.3: Distance between charged and neutral pion from a tau lepton decay. The single-tau sample with $p_T^\tau = 50\,\mathrm{GeV}$ is shown in black, the $Z \to \tau^\pm \tau^\mp$ sample is shown in red. The shift of the latter datasets towards higher distances originates in the lower visible energy.

Figure 4.4: Distance between the generated two photons from a neutral pion in a tau lepton decay in black for events from the single tau datasets with $p_T^\tau = 50\,\mathrm{GeV}$ (black) and for events from the $Z \to \tau^\pm \tau^\mp$ dataset (red).

Chapter 5

Neutral Pion Subshower Reconstruction

5.1 Strategy Overview

As discussed in Section 1.4 a tau lepton decay results in about $62\,\%$ in at least one charged pion and n neutral pions (with $n \geq 0$). Fig. 4.3 shows that for $Z \to \tau^{\pm}\tau^{\mp}$ decays more than $85\,\%$ of the neutral pions are closer than 0.1 in ΔR to a charged pion. As shown later shower of the charged pion in the calorimeter is contained within $\Delta R \approx 0.05$ from the track. Therefore the energy deposited by the charged pion and the one deposited by the neutral pions overlap in most decays, even for the transverse momenta range considered in this study (see Section 4.4). Hence it is necessary to separate the contributions to the total deposited energy due to hadronic interactions ("hadronic energy") and electromagnetic interactions ("electromagnetic energy") in order to reconstruct the number of neutral pions and their four-momenta correctly.

The approach chosen to reconstruct the neutral pion subshowers under these conditions is illustrated in Fig. 5.1. The hadronic energy in the electromagnetic calorimeter (shaded red-white) is removed from the electromagnetic calorimeter. Beforehand the amount of energy to be removed has to be calculated by subtracting the energy in the hadronic part of the calorimeter (shaded red-yellow) from the energy computed using the transverse momentum measured by the tracking system together with the assumption of the particle being a charged pion. The next step is to find neutral pion candidates in the remaining energy distribution (shaded yellow-green) and to reject possible fake candidates coming from the rest of the event or from imperfections in the energy subtraction.

The following sections explain these individual steps of the reconstruction algorithm in the order of execution. In summary they are:

- the computation of the "hadronic energy" in the electromagnetic calorimeter in Section 5.2;

- the removal of this energy in Section 5.3;

- the indication of neutral pion candidates in the remaining energy distribution in the electromagnetic calorimeter in Section 5.4;

- the suppression of misidentified neutral pion candidates in Section 5.5.

Before the neutral pion reconstruction algorithm is presented, it is useful to study the fraction of energy deposited by neutral pions for each layer in the electromagnetic calorimeter. Fig. 5.2 shows the average energy fractions deposited by an isolated neutral pion (resulting from a tau-lepton decay) in the four layers of the electromagnetic calorimeter. To ensure
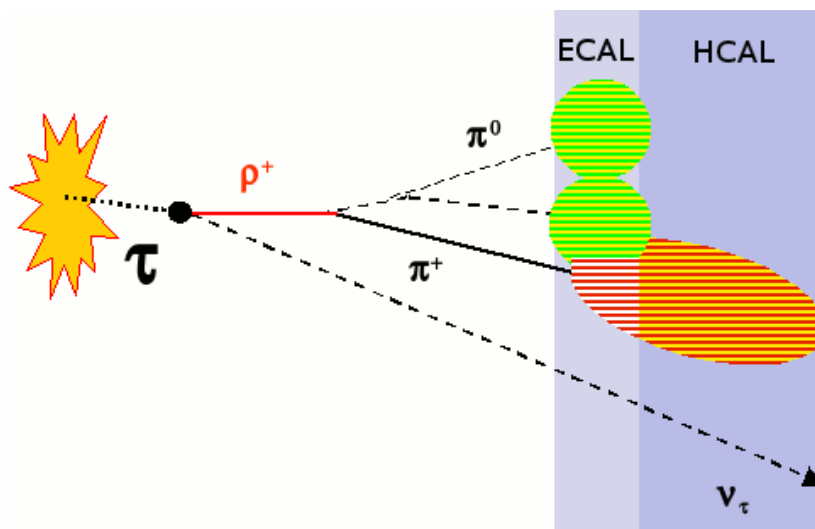
Figure 5.1: Schematic sketch of a $\tau^{\pm} \to \rho^{\pm}\nu_{\tau}$ decay in the ATLAS calorimeter. The decay lengths shown are not to scale and the overlap between the two photons and the charged pion is too small.

isolation, only neutral pions with a distance ΔR greater than 0.2 from the track are used for this study, since the energy depositions of a charged pion are well contained in a cone of $\Delta R = 0.2$ around the track, as shown later. Showers originating from neutral pions have a $99\,\%$ containment in the first three layers of the electromagnetic calorimeter.

In the following, the third layer of the electromagnetic barrel (EMB3) are counted as part of the hadronic calorimeter (HCAL), as commonly done in tau reconstruction at ATLAS. The electromagnetic calorimeter (ECAL) then comprises the first three layers (including the presampler) of the electromagnetic barrel (PresamplerB, EMB1, EMB2). This definition will be used throughout this thesis.

5.2 Calculation of the Hadronic Energy in the Electromagnetic Calorimeter

For tau-lepton decays with neutral pions a direct measurement of the energy deposited by the charged pion in the electromagnetic calorimeter (in the following E^{π}_{ECAL}) is in general not possible, since the calorimeter shower of one or more neutral pions may overlap with the charged pion's energy deposition. Therefore an indirect approach has to be used: E^{π}_{ECAL} is calculated as the difference between the charged pion energy estimated from the track measurement (E^{π}_{Track}) and the energy deposited in the hadronic calorimeter (E^{π}_{HCAL}), i.e.:

$$E^{\pi}_{\mathrm{ECAL}} = E^{\pi}_{\mathrm{Track}} - E^{\pi}_{\mathrm{HCAL}} \ . \tag{5.1}$$

The hadronic energy in the hadronic calorimeter, E^{π}_{HCAL}, can be measured by summing up the energy around the track in each layer of the hadronic calorimeters within a cone of $\Delta R = 0.2$ around the direction of the track measured at the calorimeter surface. Therefore the track has to be extrapolated to the surface of each calorimeter layer. Fig. 5.3 shows, thath the charged pion's energy is well contained in a cone of radius $\Delta R = 0.2$ around the
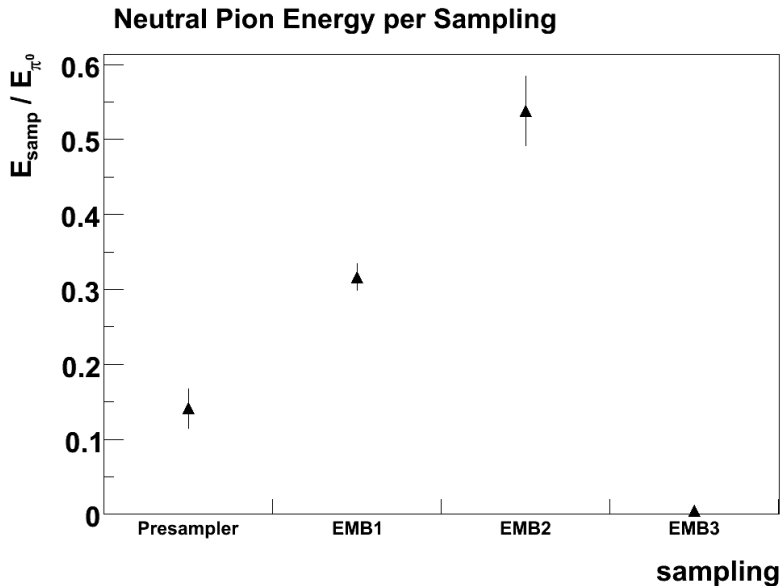
Figure 5.2: Fraction of energy per layer deposited by an isolated neutral pion in the electromagnetic calorimeter. Only a negligible amount of energy is deposited in EMB3.

track. The η, ϕ and p_T resolutions obtained from the tracking system for charged pions from the single-tau sample with $p_T^\tau = 50\,\text{GeV}$ are shown in Fig. 5.4.

5.2.1 Corrections to the Hadronic Energy Measurement

Since the ATLAS calorimeter is non-compensating (cf Section 2.2.3) the cell energy deposited by hadrons must be corrected to the hadronic energy scale. This is necessary to obtain the same response to electrons and hadrons at equal energies. For the hadronic calibration the cell energies are multiplied by a cell- and energy-dependent scale factor $f_{\frac{e}{\pi}}$.

Additionally interactions with dead material in the detector impact the energy reconstruction for hadrons. To correct this, a term $f_{\text{cryo}}\sqrt{E_{\text{EMB3}}E_{\text{Tile0}}}$ is applied [16]. E_{EMB3} and E_{Tile0} denotes the uncalibrated energy in the last layer of the electromagnetic barrel or the first layer of the hadronic tile calorimeter.

The resulting calculation of the hadronic energy in the electromagnetic calorimeter, E_{ECAL}^π, is:

$$E_{\text{ECAL}}^\pi = E_{\text{Track}}^\pi - \sum_{i \in I} f_{\frac{e}{\pi},i} E_i + f_{\text{cryo}}\sqrt{E_{\text{EMB3}}E_{\text{Tile0}}} \,, \tag{5.2}$$

where I denotes the set of cells in the hadronic calorimeter, whose distance ΔR from the track is smaller than 0.2.

5.2.2 Validation of Hadronic Energy Calculation

To verify the performance of the E_{ECAL}^π calculation, $\tau^\pm \to \pi^\pm \nu_\tau$ decays are used. The energy actually measured in the electromagnetic calorimeter around the track is compared to E_{ECAL}^π. Due to the absence of neutral pions, both energies should be the same. Fig. 5.5 shows the
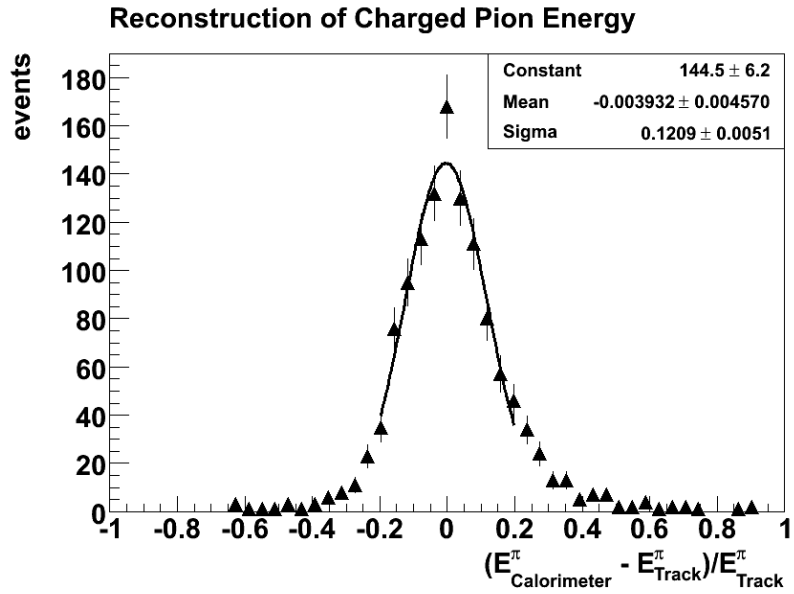
Figure 5.3: Resolution of charged pion energy reconstruction in units of energy obtained from the calorimeter for $\tau^{\pm} \to \pi^{\pm}\nu_{\tau}$ decays using the single-tau with $p_T^{\tau} = 50\,\text{GeV}$ data sample. The distribution is fitted using a Gaussian function.
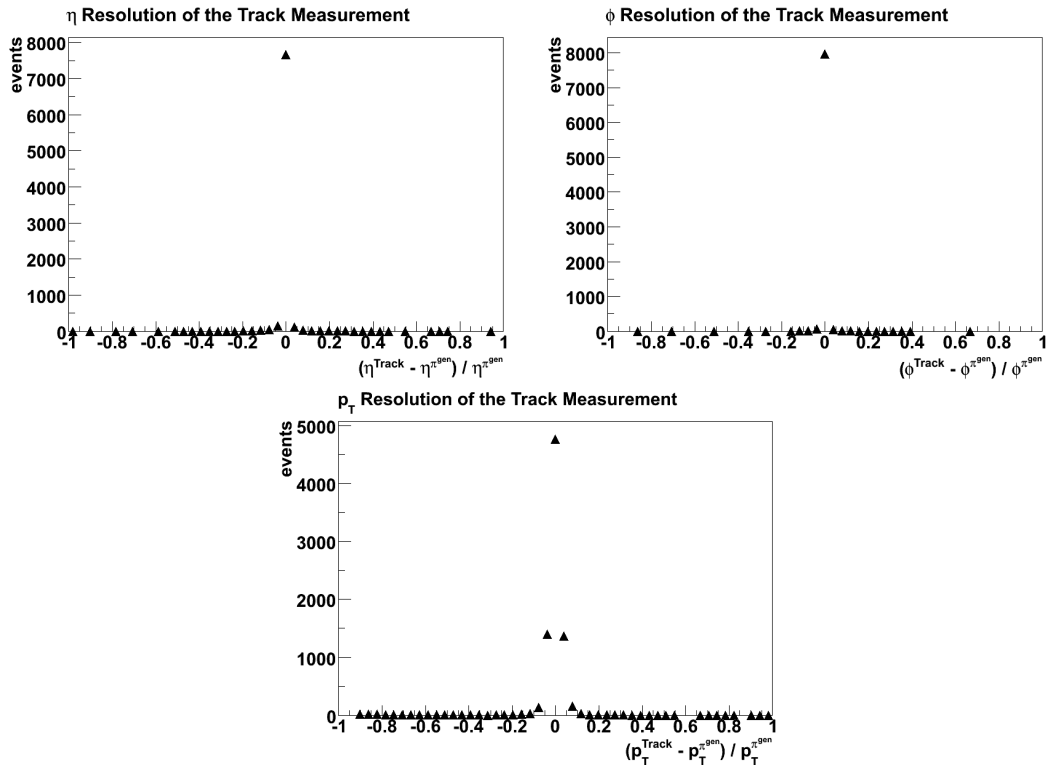
Figure 5.4: Pseudorapidity, azimuthal angle and transverse energy resolution obtained with the tracking system for charged pions from $\tau^{\pm} \to \pi^{\pm}\nu_{\tau}$ decays using the single-tau with $p_T^{\tau} = 50\,\text{GeV}$ data sample.

difference between the measured and the calculated energy. The calculation of E_{ECAL}^{π} works reasonably well. Only a small peak towards -1 can be observed. In this cases the uncertainty of the energy measurement in the hadronic calorimeter exceeds the energy deposited in the electromagnetic calorimeter.

Charged Pion Energy Calculation

Constant	89.17 ± 5.08
Mean	-0.006708 ± 0.006654
Sigma	0.1268 ± 0.0088
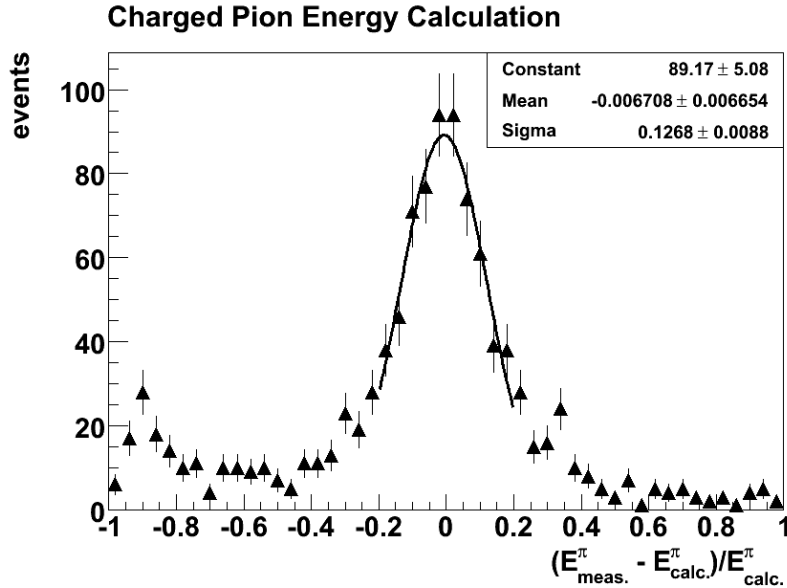
Figure 5.5: Difference between the calculated and measured energy deposited by a charged pion in the electromagnetic calorimeter. Only $\tau^{\pm} \rightarrow \pi^{\pm}\nu_{\tau}$ decays from the single-tau sample with $p_T^{\tau} = 50\,\mathrm{GeV}$ were used.

5.3 Hadronic Energy Removal

After the hadronic energy in the electromagnetic calorimeter has been estimated, it has to be subtracted from the total energy in the electromagnetic calorimeter. For a hadronic tau decay with neutral pions in the final state the energy in each cell is in general comprised of energy depositions due to hadronic and electromagnetic interactions. The goal of the subtraction is to remove the hadronic energy contribution from each cell. To calculate this contribution, the fraction of hadronic energy deposited deposited in cell i, κ_i, is estimated. The following sections describe the estimation of κ_i and the subtraction itself in more detail. In addition an approach for validating the subtraction algorithm is presented.

5.3.1 Subtraction

If κ_i is known for each cell the subtraction can be performed cell by cell. The total amount of hadronic energy deposited in each cell, defined as $\kappa_i \cdot E_{\mathrm{ECAL}}^{\pi}$, is subtracted from the measured energy, E_i, for each cell i in a cone of $\Delta R = 0.4$ around the tau jet direction (see Eq. 5.3).

$$E_i^{\mathrm{sub}} = E_i - \kappa_i E_{\mathrm{ECAL}}^{\pi} \tag{5.3}$$

Since E_{ECAL}^{π} is computed at the hadronic scale it's value exceeds the measured energy. To subtract the correct amount of energy it must be "scaled down" to the electromagnetic

scale. This is done by applying the inverse hadronic weight $\frac{1}{f_{e/\pi}}$ to E^π_{ECAL}. Thus Eq. 5.3 has to be modified. This yields the formula used to compute the hadronic energy contribution to the total energy measured in cell i and hence the formula for the remaining energy after subtraction shown in Eq. 5.4.

$$E^{\mathrm{sub}}_i = E_i - \kappa_i \frac{E^\pi_{\mathrm{ECAL}}}{f_{e/\pi,i}} \tag{5.4}$$

This formula is applied to all cells in a cone of $\Delta R < 0.4$ around the track. On average the remaining energy distribution reflects the energy deposited by the photons and hence the neutral pions of the tau lepton decay.

5.3.2 Estimation of the Hadronic Energy Fraction

The fraction of hadronic energy in each cell of the electromagnetic calorimeter, κ_i, is calculated by using the lateral and longitudinal shower development of charged pions in the electromagnetic calorimeter. If the shower development is known, κ_i, can be estimated. This is done by calculating w_i, a measurement of κ_i, using the integral of the lateral shower parameterization, f_L, over the volume of the cell and multiplying it with the longitudinal parameterization, c_L, (see Eq. 5.5). The volume element in the pseudorapidity-azimuthal angle space is denoted by $\cosh(\eta)\,d\eta d\phi$.

$$w_i = c_L \cdot \int_{\mathrm{volume\ cell\ i}} f_L\left(\eta - \eta_{trk}, \phi - \phi_{track}\right) \cosh(\eta) d\eta d\phi \tag{5.5}$$

In order to compute κ_i, w_i has to be normalized to one (see Eq. 5.6).

$$\kappa_i = \frac{w_i}{\sum_j w_j} \tag{5.6}$$

Determination of Lateral Shower Profile

The lateral shower profile shows the distribution of the charged pion's energy density as a function of the distance $\Delta\eta$ and $\Delta\phi$ from the track impact point on the calorimeter surface. It can be obtained from simulated $\tau^\pm \to \pi^\pm \nu_\tau$ events. For each event e, a two dimensional histogram in the (η, ϕ)-space, m^e, of the energy density distribution around the track is created. Since cell geometry is very different for different layers of the electromagnetic calorimeter, each layer is studied separately leading to one histogram, m^e_L, per event e and layer L. The bin size of each histogram reflects roughly the cell size of the layer it is created from. To calculate the average over all available events, each histogram is normalized by E^π_{ECAL}:

$$m_L = \sum_{\{\mathrm{events\ e}\}} \frac{m^e_L}{E^\pi_{\mathrm{ECAL}}} \ . \tag{5.7}$$

The histograms, $m_{\mathrm{Presampler}}$, m_{EMB1} and m_{EMB2}, of the energy density of a charged pion shower around its track are shown in Fig. 5.6.

The distributions of the histograms m_L are fitted with a sum of three exponential functions as proposed in [26]. The fit function has nine free parameters a_i, b_i, c_i with $i \in \{1, 2, 3\}$ and is given in Eq. 5.8. Two different parameters, b_i and c_i, are used for the width in η and ϕ
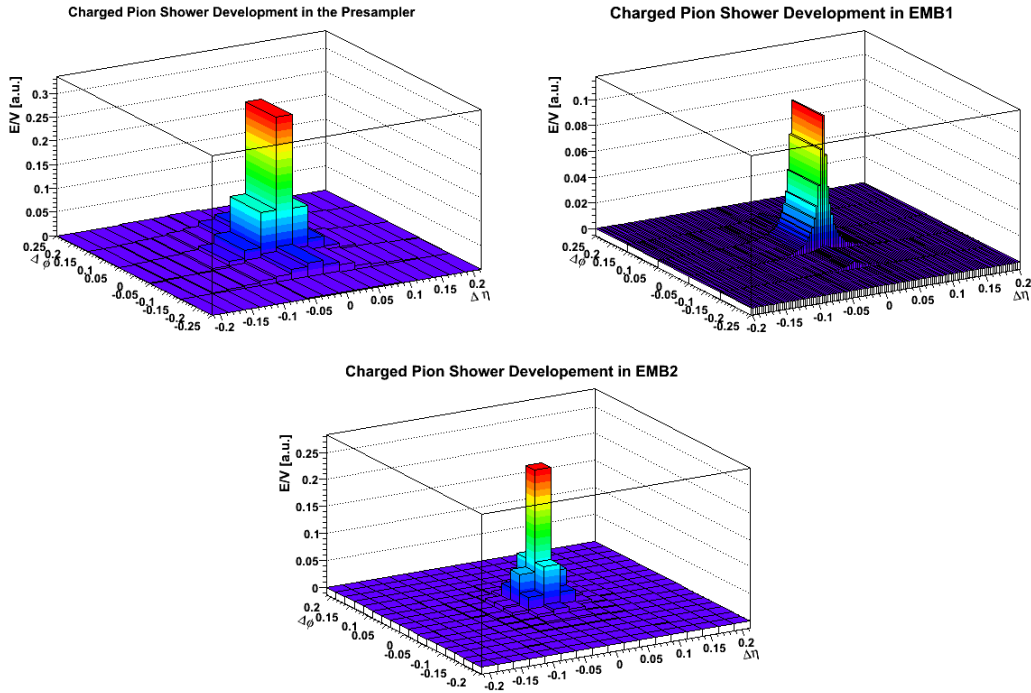
Figure 5.6: Energy density distributions in the (η, ϕ)-space around the track of a charged pion from a $\tau^{\pm} \rightarrow \pi^{\pm}\nu_{\tau}$ decay using the single-tau sample with $p_T^{\tau} = 50\,\text{GeV}$.

respectively, since the cells of the first two layers of the electromagnetic calorimeter are not quadratic.

$$f_L^{\text{fit}} = \sum_{i \in \{1,2,3\}} a_i e^{-\sqrt{b_i \Delta \eta^2 + c_i \Delta \phi^2}} \tag{5.8}$$

Since it is not easy to check the quality of a two dimensional fit the fitted distributions are presented in three different ways:

1. as a projection onto the η-axis

2. as a slice of $\Delta \phi \leq \Delta \phi_{\text{cell}}$ in η direction through the center of the distribution

3. as an "unrolled" one-dimensional histogram (containing all bins of the two-dimensional distribution)

Fig. 5.7 shows the three visualizations for the EMB2 layer of the electromagnetic calorimeter and Fig. 5.8 shows the energy distribution and the resulting fit for each layer of the electromagnetic barrel as $\Delta \eta$ projections. The values of the nine free parameters a_i, b_i and c_i ($i \in \{1, 2, 3\}$) obtained from the fit and the resulting distributions are shown in Tab. 5.1 and Fig. 5.9.

Determination of Longitudinal Shower Profile

To determine the longitudinal shower development, the relative amount of charged pion energy per layer, c_L, is derived. The determination of c_L is done using single charged pions from
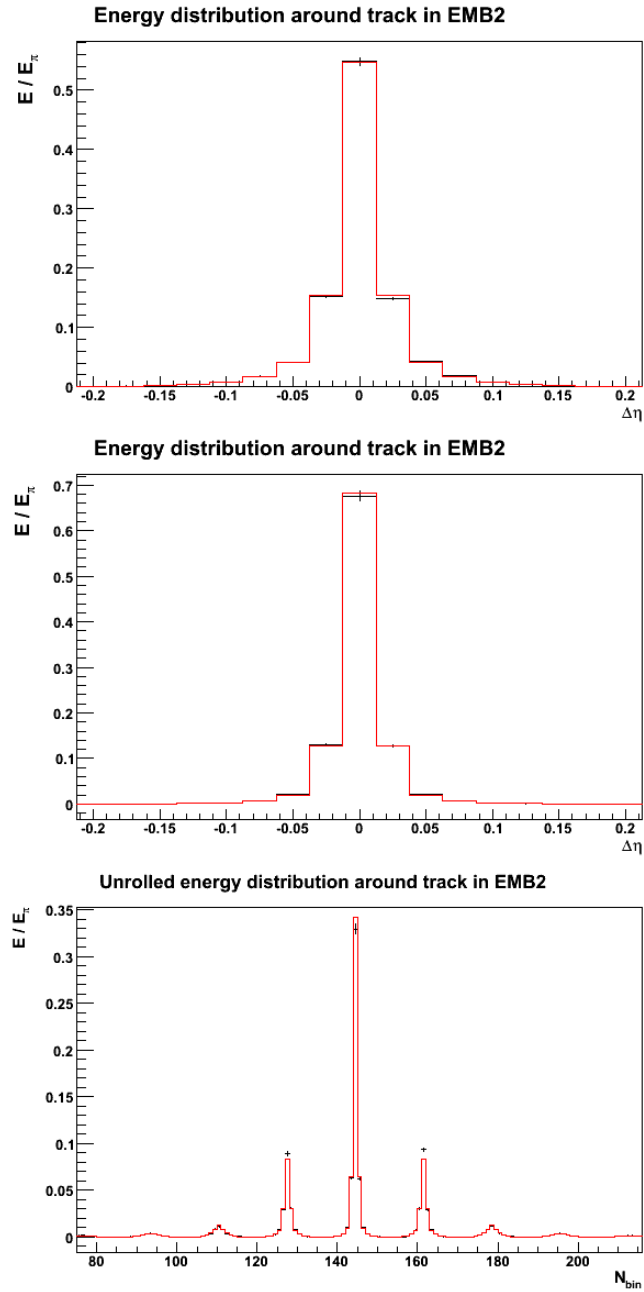
Figure 5.7: Lateral shower profile of a charged pion in the second layer of the electromagnetic calorimeter (black) and the resulting fit (red).
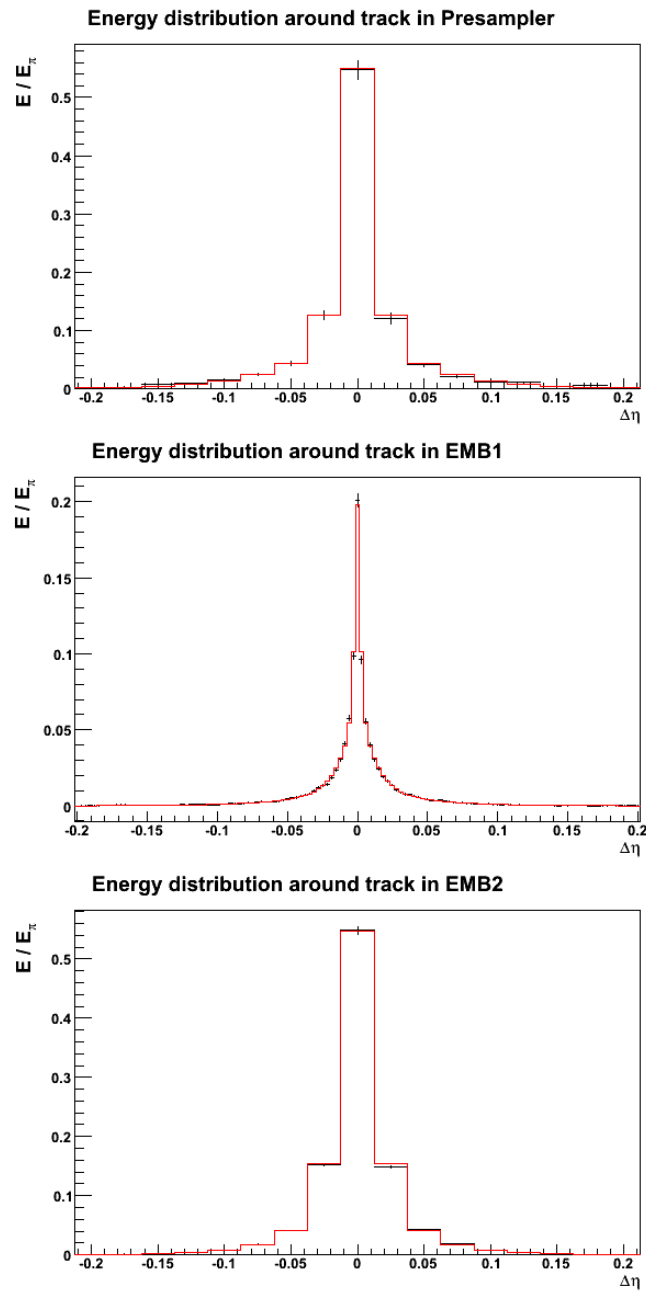
Figure 5.8: Lateral shower profiles (black) of a charged pion in the Presampler (top left), EMB1 (top right) and EMB2 (bottom) and the resulting fit (red). Shown is the (η, ϕ) distribution projected onto the η-axis.
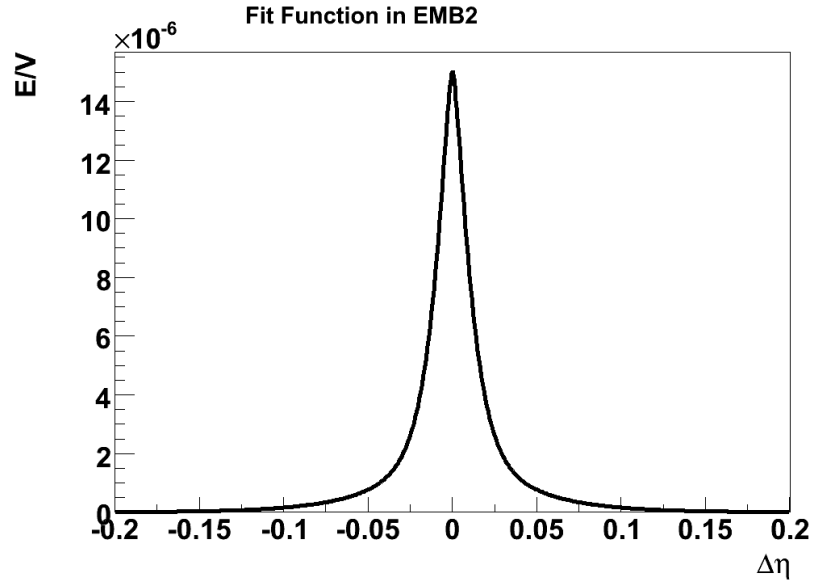
Figure 5.9: Function used to fit the lateral shower profiles of single charged pions in the second layer of the electromagnetic calorimeter. Shown is the projection onto η.

parameter	Presampler	EMB1	EMB2
a_1	(1.71 ± 0.32)	$(2.73 \pm 0.88)10^{-1}$	(1.05 ± 0.06)
b_1	$(2.61 \pm 0.69)10^4$	$(3.81 \pm 0.14)10^4$	$(1.79 \pm 0.12)10^4$
c_1	$(3.06 \pm 0.77)10^3$	$(2.81 \pm 0.14)10^3$	$(1.35 \pm 0.07)10^4$
a_2	$(1.62 \pm 0.24)10^{-1}$	$(2.17 \pm 0.05)10^{-2}$	$(4.25 \pm 0.26)10^{-2}$
b_2	$(8.96 \pm 0.89)10^1$	$(1.37 \pm 0.01)10^3$	$(1.40 \pm 0.05)10^3$
c_2	$(8.08 \pm 0.72)10^1$	$(9.98 \pm 0.14)10^2$	$(1.31 \pm 0.04)10^3$
a_3	$(7.17 \pm 0.49)10^{-2}$	$(6.79 \pm 0.07)10^{-6}$	$(1.40 \pm 0.43)10^{-4}$
b_3	$(4.43 \pm 0.03)10^1$	$(5.52 \pm 0.15)10^1$	$(5.30 \pm 0.01)10^1$
c_3	$(7.07 \pm 0.05)10^1$	$(5.22 \pm 0.14)10^1$	$(5.43 \pm 0.02)10^1$

Table 5.1: Parameters of the functions used to fit the lateral shower profiles of a single charged pion in the electromagnetic calorimeter. The errors given are those from the fit algorithm.

simulated $\tau^{\pm} \to \pi^{\pm}\nu_{\tau}$ events. Fig. 5.10 shows the average fraction of charged pion energy c_L deposited per ECAL-layer L within a cone of $\Delta R \leq 0.2$ around the track. Since the cells in the EMB2 layer of the electromagnetic calorimeter have the largest volume, they contain the largest fraction of energy.

Charged Pion Longitudinal Shower Development
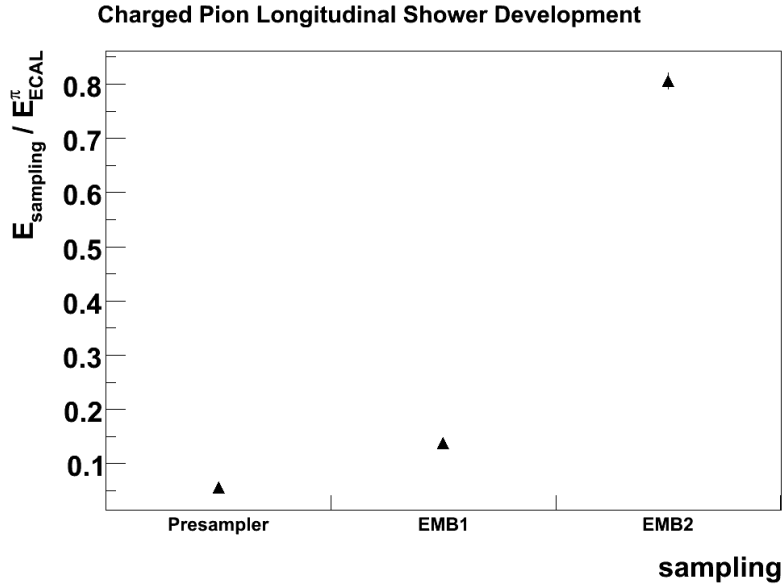
Figure 5.10: Relative amount of charged pion energy for each ECAL layer. The steep rise in EMB2 results from the greater volume of cells in the second layer.

5.3.3 Validation of the Subtraction Algorithm

The validation of the subtraction algorithm is done in two steps. At first the correct implementation of Eq. 5.1 – 5.4 has been checked by using a simple "toy test". The subtraction algorithm is then applied to a sample of simulated $\tau^{\pm} \to \pi^{\pm}\nu_{\tau}$ decays.

Energy Subtraction Toy Test

As a first check if the energy-subtraction method has been implemented correctly, a simple "toy test" has been performed. A two-dimensional histogram is filled using the parameterization of the lateral charged pion showers described above. Afterwards the energy subtraction algorithm described in Eq. 5.1 – 5.4 is run. Fig. 5.11 shows the initial and the remaining energy distribution projected onto the η-axis. The algorithm successfully removes the complete amount of energy, resulting in a flat energy distribution after subtraction. This toy test allowed for systematical studies of the dependence of the subtraction algorithm on different parameterizations of the radial shower profile and on different cell geometries. It exposed several deficiencies in earlier versions of the subtraction algorithm.
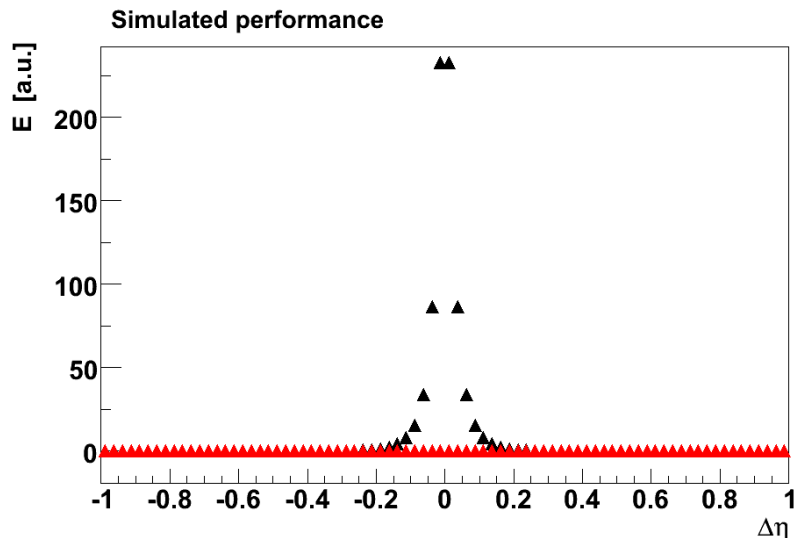
Figure 5.11: Initial (black) and remaining (red) energy obtained from a "toy test" of the subtraction of charged pion energy contributions in the electromagnetic calorimeter (Section 5.3.3).

Performance Evaluation of the Subtraction Algorithm

To evaluate the performance of the subtraction algorithm inside the official reconstruction framework, the energy distribution of charged pions from $\tau^{\pm} \to \pi^{\pm}\nu_{\tau}$ decays of the $Z \to \tau^{\pm}\tau^{\mp}$ sample are used. In this case the energy remaining after subtraction is expected to be zero, since the total available energy results from the charged pion. Fig. 5.12 shows both the initial energy deposited by the charged pion (black) and the energy remaining after subtraction (red). The subtraction seems to work reasonably well. Very close to the track the subtraction algorithm removes a little too much energy. A possible explanation is the dependence of the lateral parameterization of the shower profiles on the transverse momentum of the charged pions. As was shown in Section 4.4, the E_T spectrum of charged pions from tau-lepton decays for the $Z \to \tau^{\pm}\tau^{\mp}$ sample is slightly softer than for the single-tau sample with $p_T^{\tau} = 50\,\text{GeV}$. A comparison of the single-tau sample for $p_T^{\tau} = 50\,\text{GeV}$ and $p_T^{\tau} = 100\,\text{GeV}$ shows large differences (see Fig. 5.13) as expected. The slight imperfections observed for the subtraction do not necessitate a separate shower profile parameterization for different E_T intervals for the E_T range studied in this thesis. The percentage of the remaining energy in units of the total hadronic energy measured in the electromagnetic calorimeter is shown in Tab. 5.2.

layer	energy remaining[%]
Presampler	1.02
EMB1	0.57
EMB2	−4.35

Table 5.2: Average fraction of remaining energy in units of the total energy deposited by the charged pion in the electromagnetic calorimeter obtained after running the subtraction algorithm on a sample of $\tau^{\pm} \to \pi^{\pm}\nu_{\tau}$ decays from the $Z \to \tau^{\pm}\tau^{\mp}$ sample.
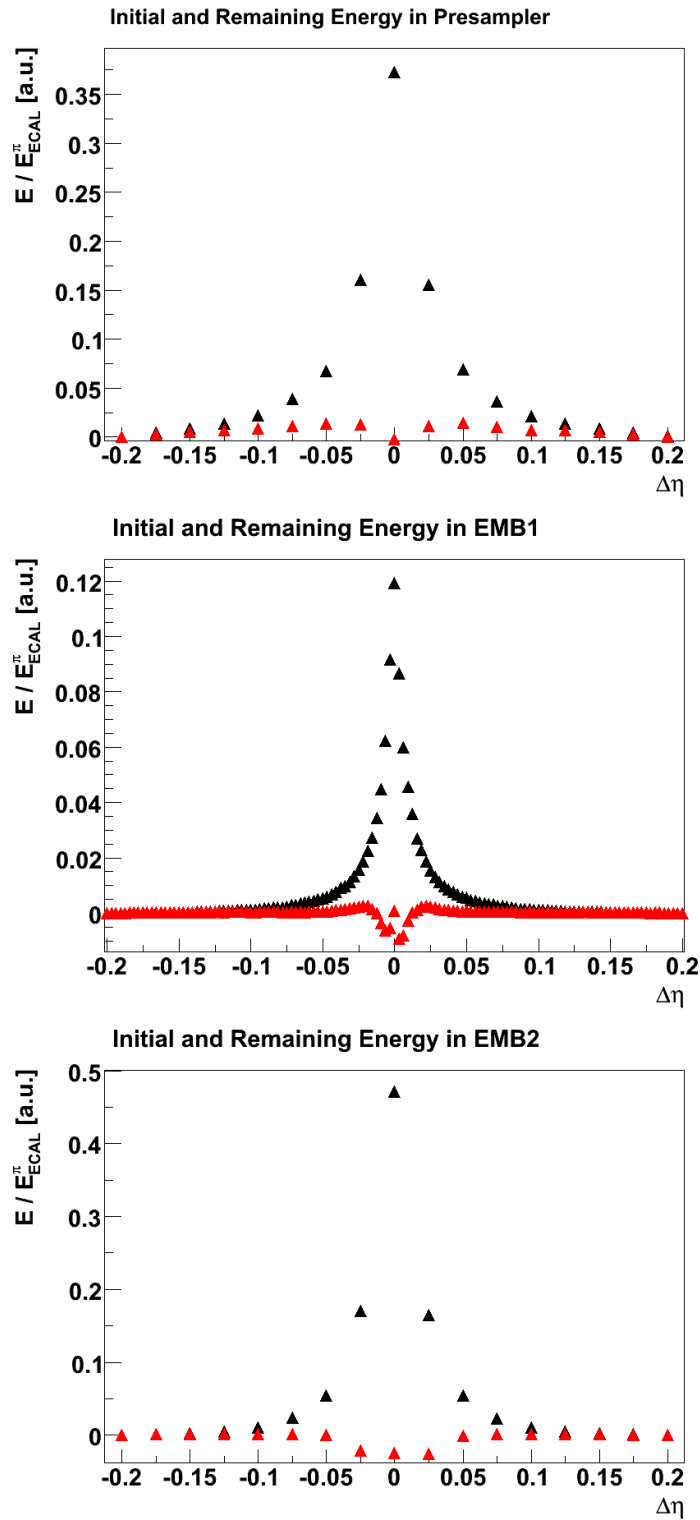
Figure 5.12: Initial (black) and remaining (red) energy in units of E_{track} after subtraction. Shown is a projection of the (η, ϕ) energy distribution along ϕ onto the η axis.

Lateral Shower Development as function of p_T^π
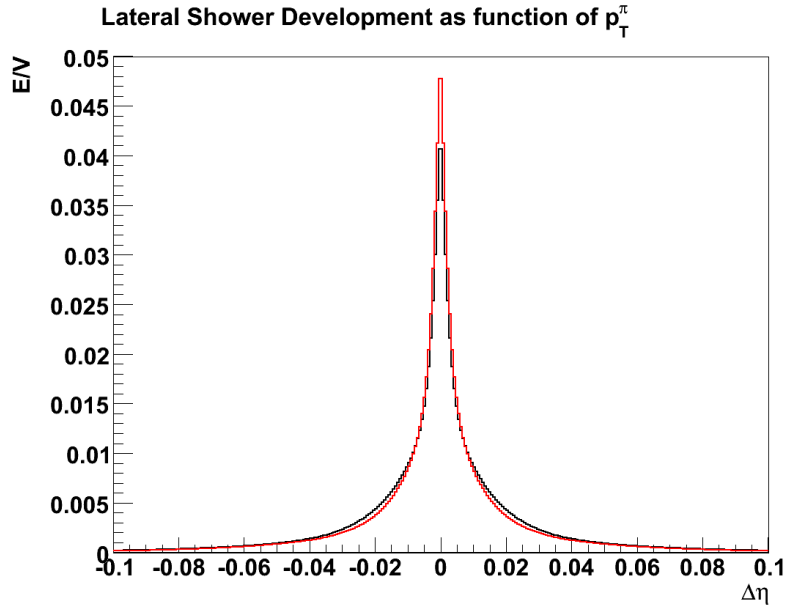
Figure 5.13: Lateral shower profiles of charged pions with $p_T^\pi < 50\,\text{GeV}$ in black and lateral shower profiles of charged pions with $50\,\text{GeV} < p_T^\pi < 100\,\text{GeV}$ in red.

5.4 Neutral Pion Candidate Finding

After removing the charged pion energy from the electromagnetic calorimeter neutral pion candidates have to be found in the remaining energy distribution. This is done by running a clustering algorithm over the cells in the remaining energy distribution and looking for electromagnetic cluster. These clusters can be classified as follows:

(1) Neutral pion cluster containing the energy depositions of both photons ("merged clusters").

(2) Clusters resulting from single photons that come from a neutral pion decay at small momenta.

(3) Clusters resulting from the rest of the event not connected to the tau lepton decay

(4) Clusters that are due to imperfections of the hadron energy subtraction. On the event-by-event basis, the shower profiles deviate form the average shower profiles obtained from the fit.

The first two items are considered as signal for this study. The clusters in classes three and four not resulting from neutral pions, need to be suppressed. This suppression will be covered in Section 5.5. In the following, all clusters found are considered as neutral pion clusters. As it turns out most of the neutral pions observed make a single merged cluster only in about $4\,\%$ of the cases, the photons are found as separated cluster ($Z \to \tau^\pm \tau^\mp$ sample). A possible strategy for recombining two distinct photon clusters to a neutral pion will be discussed in Chapter 6.

Different clustering algorithms were tested and the Topological Clustering [27] algorithm available as an algorithm in the Athena framework was chosen. One of its main advantages is that it is thoroughly maintained and tested due to its widespread use in the ATLAS reconstruction software.

Topological Clustering

The Topological Clustering algorithm uses cells as seeds that have an energy-to-noise ratio above an adjustable threshold ("Seed Threshold"). All direct neighbors of the cell are inspected and added to the cluster if their energy exceeds the so-called "Neighbour Threshold" value. This is continued until no more neighboring cells exceeding this threshold are found. As a last step all adjacent cells whose energy to noise ratio is above the so-called "Cell Threshold" are added to the cluster.

After all clusters have been built a cluster splitting algorithm is run, which searches for local maxima in these clusters. The energy of the local maximum must exceed an adjustable splitting threshold. All cells from the original cluster are then grouped around local maxima. The splitting algorithms ensures that two local maxima exceeding the splitting threshold never end up in the same cluster.

The threshold configuration used for the neutral pion reconstruction is shown in Tab. 5.3. This parameter choice corresponds to the "standard" Topological Clustering used for tau reconstruction in ATLAS. These settings should be revisited in the future to study their impact on the neutral pion reconstruction and possible improvements.

parameter	value[σ_{noise}]
Seed Threshold	4
Neighbour Threshold	2
Cell Threshold	0

Table 5.3: Settings used for the "Topological Clustering" algorithm.

Neutral Pion Candidate Selection

Each cluster formed by the Topological Clustering algorithm applied to the remaining energy distribution in the electromagnetic calorimeter in a cone of $\Delta R = 0.4$ (the "tau-cone") around the track, is treated as a neutral pion candidate. Fig. 5.14 shows the number of reconstructed neutral pion candidates for $\tau^{\pm} \to \pi^{\pm}\nu_{\tau}$, $\tau^{\pm} \to \rho^{\pm}\nu_{\tau}$ and $\tau^{\pm} \to a_1^{\pm}\nu_{\tau}$ decays separately for which zero, one or two neutral pions are expected. The majority of candidates are misidentified clusters.

Additional requirements on the transverse energy and the distance of the neutral pion candidate from the track are used to reduce the number of neutral pion misidentifications. The E_T spectrum of the neutral pion candidates and their distance from the track are shown in Fig. 5.16. Motivated by these distributions neutral pion candidates must meet the following requirements: $E_T > 500\,\mathrm{MeV}$ and $\Delta R\left(\pi, \pi_{\mathrm{cand}}^0\right) < 0.2$. The number of candidates found in $\tau^{\pm} \to \pi^{\pm}\nu_{\tau}$ decays after applying these selection criteria is shown in Fig. 5.15. A clear reduction in the number of neutral pion candidates is visible.
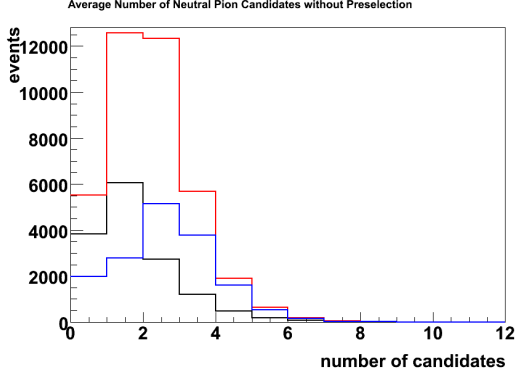
Figure 5.14: Number of candidates for $\tau^\pm \to \pi^\pm \nu_\tau$ (black), $\tau^\pm \to \rho^\pm \nu_\tau$ (red) and $\tau^\pm \to a_1^\pm \nu_\tau$ (blue) decays from the $Z \to \tau^\pm \tau^\mp$ sample after subtracting the charged pion energy from the electromagnetic calorimeter.
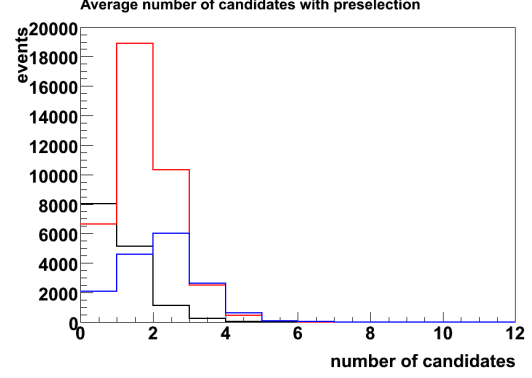
Figure 5.15: Number of neutral pion candidates with $E_T > 500\,\mathrm{MeV}$ and $\Delta R\left(\pi, \pi_{\mathrm{cand}}^0\right) < 0.2$ for $\tau^\pm \to \pi^\pm \nu_\tau$ decays (black), $\tau^\pm \to \rho^\pm \nu_\tau$ decays (red) and $\tau^\pm \to a_1^\pm \nu_\tau$ decays (blue) from the $Z \to \tau^\pm \tau^\mp$ sample.
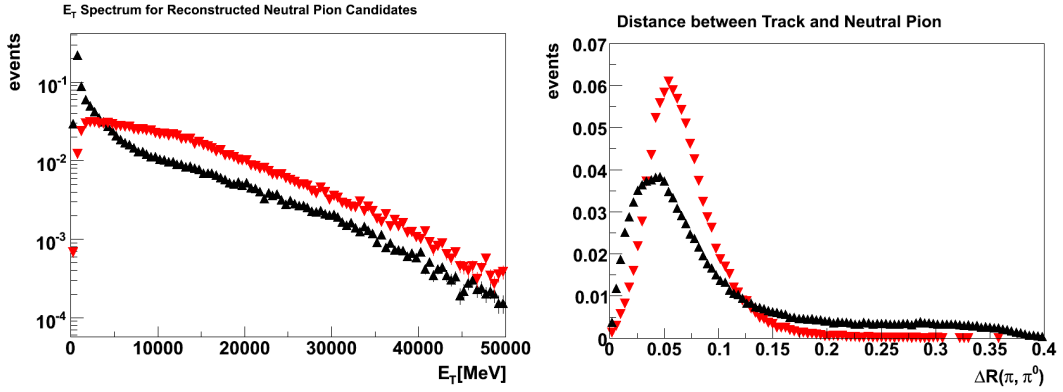
Figure 5.16: E_T spectrum and distance ΔR from track of all reconstructed neutral pion candidates (black) and generated neutral pions (red).

5.5 Suppression of Misidentified Neutral Pion Candidates

The distribution in Fig. 5.15 shows on average 0.6 neutral pion candidates for $\tau^\pm \to \pi^\pm \nu_\tau$ decays. This indicates the need for further suppression since no neutral pion is expected.

5.5.1 Neutral Pion Truth Matching

In order to classify the neutral pion candidates as signal or background it is necessary to create an truth-matching algorithm. As neutral pions decay into two photons twofold approach for the matching of reconstructed neutral pions to generated ones is used. The algorithm must be able to match both photons creating only one single neutral pion cluster and photons creating two distinct clusters.

At first the smallest distance $\Delta R_m in$ between the reconstructed neutral pion candidate and a generated neutral pion, π^0_{gen}, is calculated. If no match for a candidate is found, i.e. the closest distance, $\Delta R_m in$ exceeds 0.025, a match between the candidate and a generated photon is attempted. The following enumeration outlines this procedure:

For each reconstructed neutral pion candidate:

1. if $\Delta R_{\min}(\pi^0_{\text{gen}}, \text{candidate}) < 0.025$: classify candidate as signal;
2. else if $\Delta R_{\min}(\gamma_{\text{gen}}, \text{candidate}) < 0.025$: classify candidate as signal;
3. else: classify candidate as background.

5.5.2 Discriminating Variables

Various discriminating variables are used to distinguish between candidates from real neutral pions (signal) and those from imperfections of the algorithm or from the rest of the event (background). Eight variables that characterize the shape of the candidate cluster are taken from the so-called "CaloClusterMomentsMaker" algorithm implemented as part of the Topological Clustering [28] and are listed below. Here a moment of the quantity x is defined as $\langle x \rangle = \sum_i E_i x_i$ and the sum runs over cells with positive energy belonging to the cluster. The formulas for each variable are given in App. A.2.

<div align="center">CaloClusterMomentsMaker variables</div>

$\langle E/V \rangle$	first moment in energy density
$\langle (E/V)^2 \rangle$	second moment in energy density
$\Delta\alpha$	angle between the vector pointing from the interaction point to the shower center and the shower axis
$\Delta\phi$	ϕ difference between the shower axis and the vector pointing from the interaction point to the shower center
λ_{center}	distance along the shower axis between the calorimeter front face and the shower center
$f_{\max}$	energy fraction in the most energetic cell
$\langle \lambda^2 \rangle$	second moment in distance from shower center along the shower axis
$\langle \text{long}^2 \rangle$	second longitudinal moment

In addition the four discriminating variables listed below are used.

Custom variables	
N_{cells}	number of cells with positive energy
$\frac{E_{\text{core}}}{E}$	fraction of energy deposited in the three innermost η- strips
$\langle \eta \rangle$	first moment in η
$\langle \eta^2 \rangle$	second moment in η

In total 12 variables are available to discriminate signal from background.

The true neutral pion clusters tend to be more compact than the misidentified ones. Therefore the variables describing the extension of the cluster, e.g. the moments $\langle \eta \rangle$ and $\langle \eta^2 \rangle$, provide a good separation. For the same reason the moments of the energy density, the fraction in the most energetic cell and the fraction in the three innermost η-strips are good candidates to discriminate against misidentified neutral pion candidates. The distributions of the discriminating variables are shown in Fig. 5.17 and 5.18.

After classifying all available neutral pion candidates as being either signal or background, all discriminating variables can be checked for their usefulness in terms of separation power and correlations. To quantify these properties the "Toolkit for Multivariate Data Analysis" (TMVA) [29] is used. The distributions of the twelve discriminating variables are shown Fig. 5.17 and 5.18 for misidentified neutral pion clusters (red), clusters matched to a single photon (green) and clusters matched to neutral pions (blue). The latter two are considered as signal. The correlations are shown in Fig. 5.19. The discriminating variable $\langle \eta \rangle$ and $\langle (E/V)^2 \rangle$ are not used to their high correlations.

The distributions of clusters from single photons and neutral pions are in general quite similar. Only the first moment in energy density, the number of cells and the second moment in η are different. This can be explained, since the energy density in a cell hit by two photons will exceed the single photon case and two photons will build broader clusters yielding more cells with positive energy. The smaller average value of $\langle \eta^2 \rangle$ for clusters matched to neutral pions may result from the fact that it is calculated using a cone of $\Delta R = 0.05$ and thus the second photon from a neutral pion decay will be included in the calculation.

5.5.3 Discrimination Methods

Two different approaches have been implemented to distinguish signal from background:

- a method using one dimensional selection criteria;

- a multivariate method, in this case an "Artificial Neural Network" (ANN).

The first approach provides a safe and – compared to a neural network – easy to understand procedure to be used for first data, even though it might not yield the optimal performance. In contrast the neural-network method is particularly useful if many input variables with significant correlations are used, but it is harder to control and validate.

One Dimensional Selection Criteria

The selection is based on one-dimensional cuts on four discriminating variables with the best separation power: $\langle \eta \rangle$, $\langle \eta^2 \rangle$, N_{cells} and $\langle \frac{E}{V} \rangle$. Since $\frac{E_{\text{core}}}{E}$ is highly correlated with the second
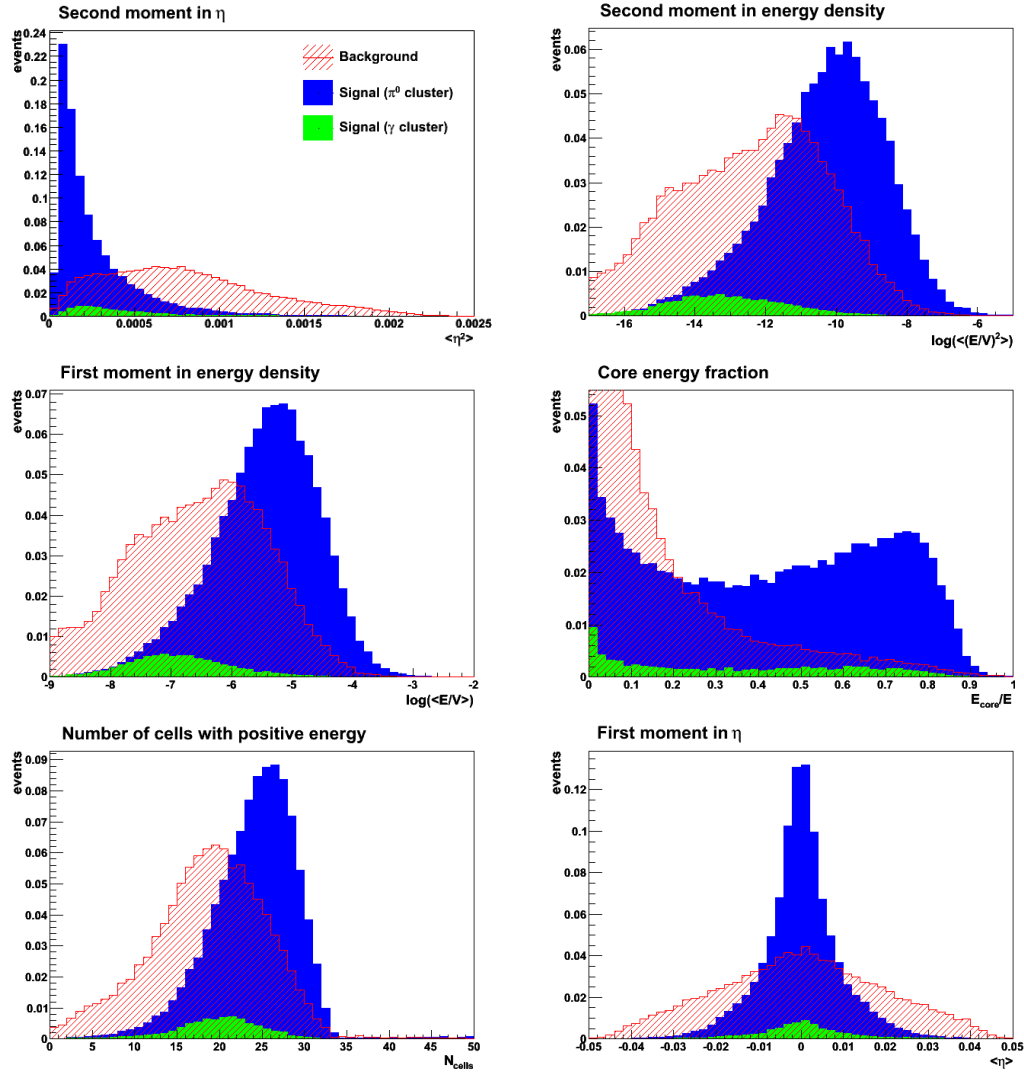
Figure 5.17: The first six discriminating variables in descending order with respect to their separation power between signal and background. The red histogram shows the distributions of misidentified neutral pion candidates, the green histogram the distributions of single-photon cluster from neutral pions and the blue histogram the distributions of truth-matched neutral pion clusters. The green and blue histogram are stacked; both are considered signal. The meaning of the different variables is described in the text.
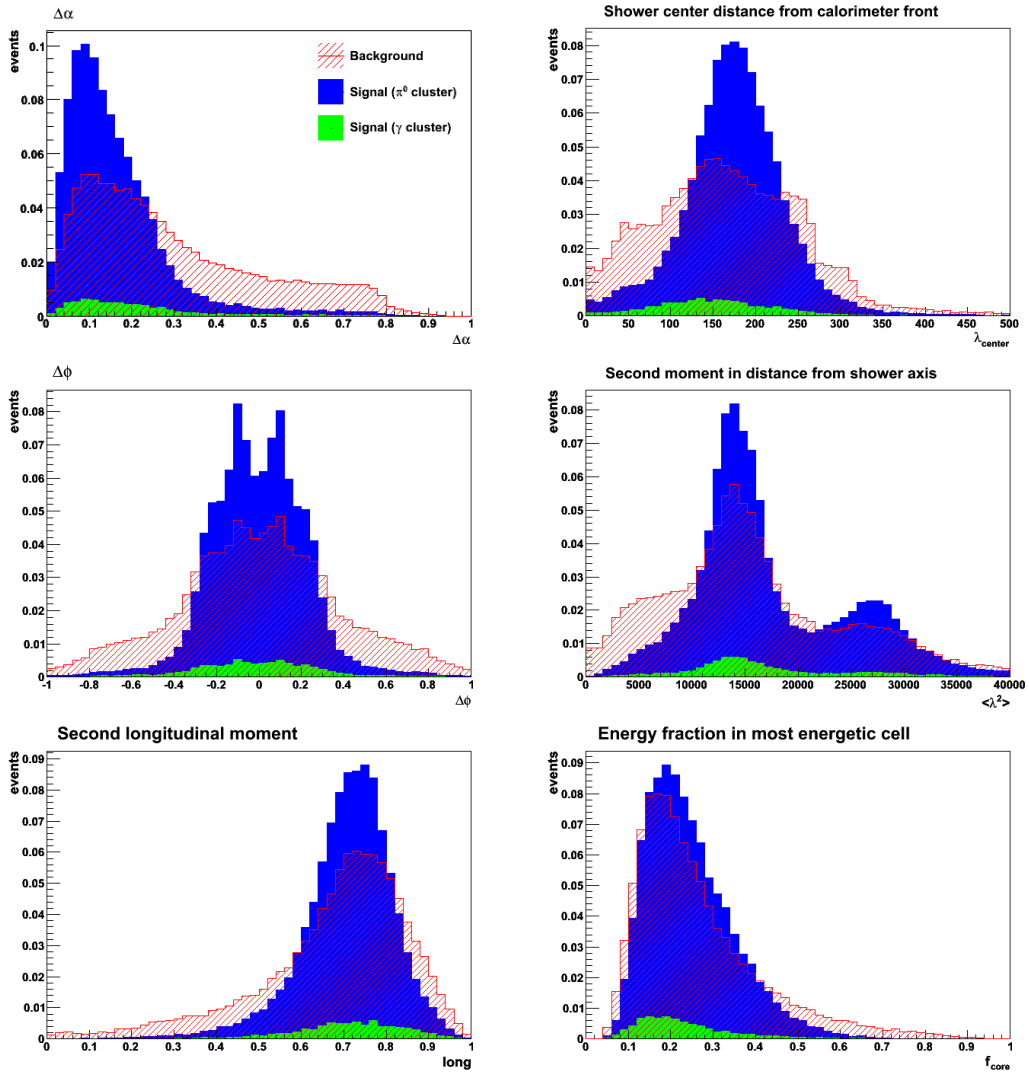
Figure 5.18: The last six discriminating variables in descending order with respect to their separation power between signal and background. The red histogram shows the distributions of misidentified neutral pion candidates, the green histogram the distributions of single-photon cluster from neutral pions and the blue histogram the distributions of truth-matched neutral pion clusters. The green and blue histogram are stacked; both are considered signal. The meaning of the different variables is described in the text.
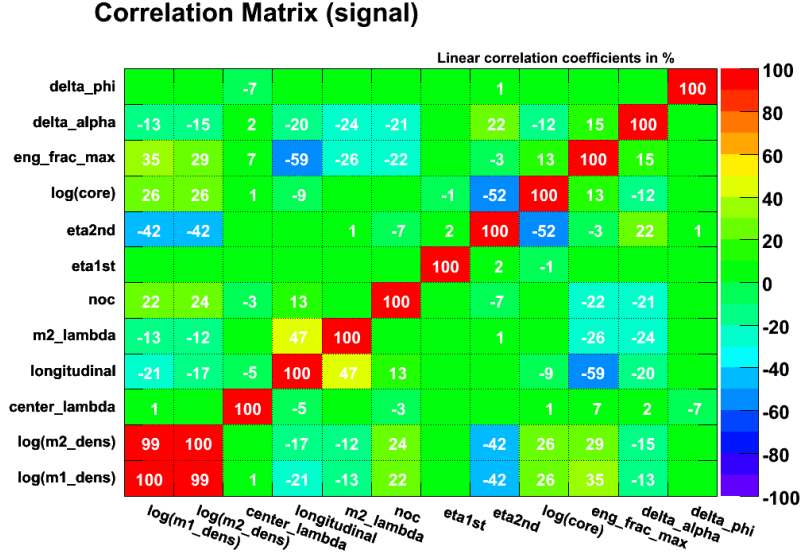
Figure 5.19: Correlations between the twelve discriminating variables. The numbers indicate correlations in percent. No number means no correlation is observed.

moment in η (52 %) and the first moment in energy density (27 %) it has been dropped. An initial set of cuts has been chosen by eye. In order to study the impact of these cuts on the input variables, the distributions of the variables are created, after the selection cuts on the other variables have been applied. Fig. 5.20 shows this distributions. It turns out, that the first moment in η does not provide any additional separation after the cuts on the other three variables. It is therefore dropped.

The final selection criteria applied are listed in Tab. 5.4. This selection is considered to be safe enough to be used with first data.

variable	selection criteria
$\langle \eta^2 \rangle$	< 0.0007
$\log\left(\langle \frac{E}{V} \rangle\right)$	> -7
N_{cells}	> 12

Table 5.4: Summary of all selection criteria applied to neutral pion candidates.

Artificial Neural Network

For the multivariate analysis all ten discriminating variables are used. Multivariate analyses are used to exploit multi-dimensional correlations to reach a better background rejection or signal-to-background ratio. Generally speaking a multivariate analysis maps the multidimensional space of input variables x_i to a single output variable d which is used to discriminate between signal and background. An artificial neural network (ANN) achieves this mapping by using a directed graph of artificial neurons (nodes), where each neuron produces a response depending on the set of input signals it receives.
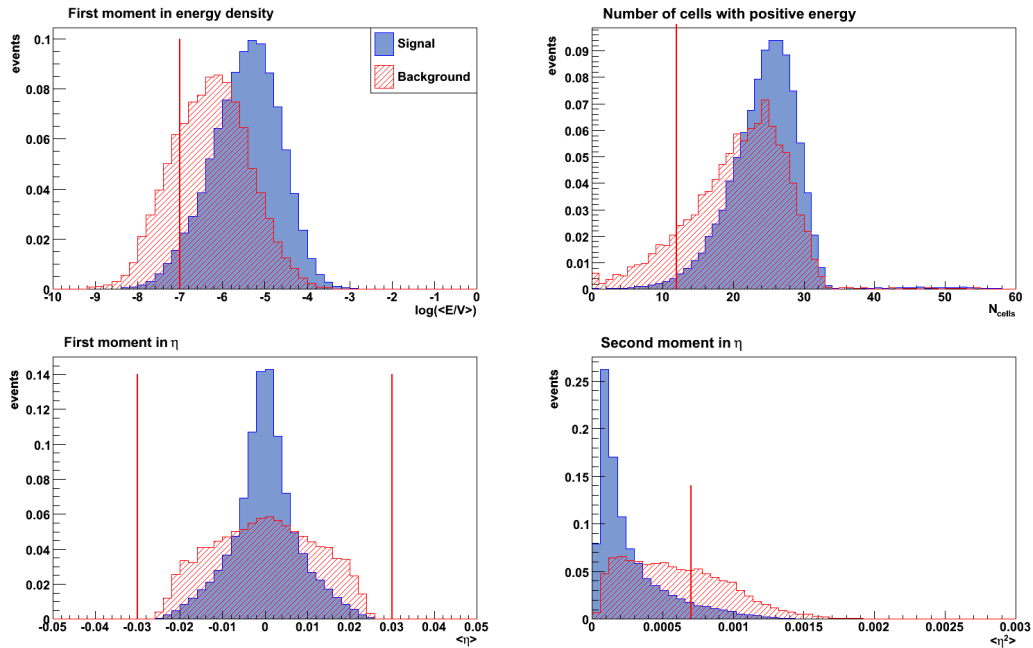
Figure 5.20: Distribution of the four input variables chosen for the cut based method, after the selection on the other variables have been applied. The red line indicates the chosen cut. The cut on $\langle\eta\rangle$ turned out to be superfluous.

The MLP classifier from the "Toolkit for Multivariate Analysis" (TMVA)[29] is used in this study. It is configured to consist of four layers: one input layer, one output layer and two hidden layers inbetween. The input layer has n neurons, where n is the number of input variables (nine in this case). The two hidden layers are made up of four and two neurons, respectively. One neuron builds the output layer. The chosen architecture is shown in Fig. 5.21.

Generally speaking each neuron represents a function which yields an output value y_i depending on the input x_i. The so-called activation function $y_i = f_i(x_i)$, which connects the input with the output used in this network, is the sigmoid function:

$$f_i(x_i) = \frac{1}{1 + e^{-x_i}} \ .$$ (5.9)

.

Each neuron is connected with all neurons of the neighboring layers. These connections are associated with a weight w_j. The input of a neuron n is a linear combination of the weighted output from the neurons in the preceding layer:

$$x_n = \sum_j w_j y_j \qquad j \in J$$

$$J = \{\text{neurons } i : \text{layer}(i) = \text{layer}(n) + 1\} \ .$$ (5.10)

.

The weights w_j which define the behavior of the neural net are obtained by training the
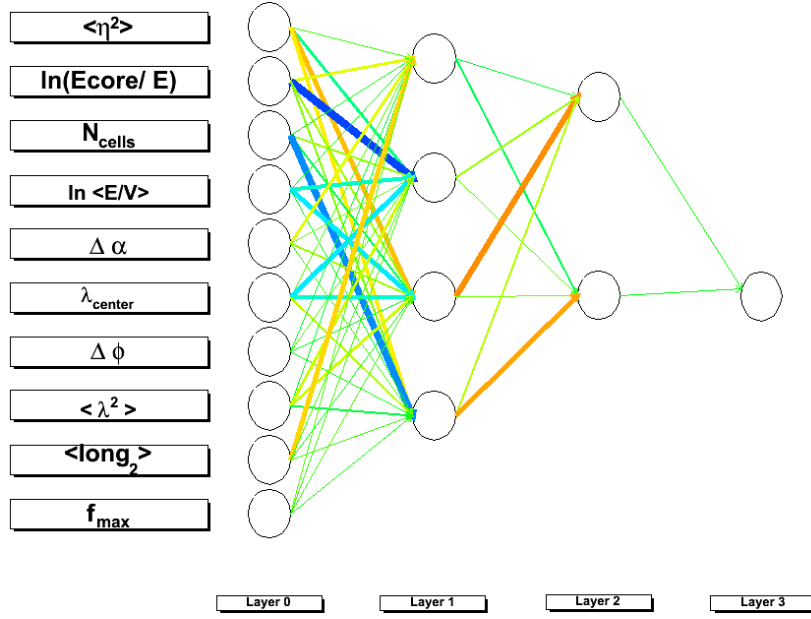
Figure 5.21: Architecture of the neural network used for the suppression of misidentified neutral pion candidates. On the left the input neurons are shown and on the right the output neuron. Inbetween the two hidden layers. The thickness of the connections illustrates the weight.

ANN with a sample of signal and background events. The training tries to minimize the error

$$\mathrm{e}(\vec{x}, \vec{w}) = \frac{1}{2} \left(y_{out} - y_{true} \right) \tag{5.11}$$

for each event. Here y_{out} denotes the output of the ANN, y_{true} is the expected output (one for signal and minus one for background), $\vec{x}$ is the input and $\vec{w}$ denotes the weights, which are chosen randomly for the first event. After each event $\vec{w}$ is corrected by calculating the derivative $-\nabla e$ and changing $\vec{w}$ accordingly. This is repeated m_{cycles} times (η denotes the learning rate):

$$\vec{w}^{m_{\mathrm{cycles}}} = \vec{w}^{m_{\mathrm{cycles}}-1} - \eta \nabla e \ . \tag{5.12}$$

The ANN is trained using one half of the available signal and background samples. After this training is finished a discriminant[1] is generated. The other half of the samples is used to check the performance and test for overtraining. The error estimator as a function of the training cycles is shown in Fig. 5.22. For this study 500 training cycles are chosen. At this point the error estimator reaches its final value and the probability of overtraining is minimized, since the number of training cycles is kept as small as possible. The discriminant obtained from the ANN is shown in Fig. 5.23 for clusters matched to neutral pions, clusters matched to single photons and misidentified neutral pion clusters in separately. Clusters from single photons show an almost flat distribution, since the three most important shower shapes ($\langle \eta^2 \rangle$, $\langle E/V \rangle$ and N_{cells}) are different for clusters matched to neutral pions and for clusters matched to single photons (see above). The selection applied on this discriminant used to separate between signal and background is discussed in the next chapter.

---

[1]The discriminant the output distribution of the output neuron. It is presented separately for signal and background events.
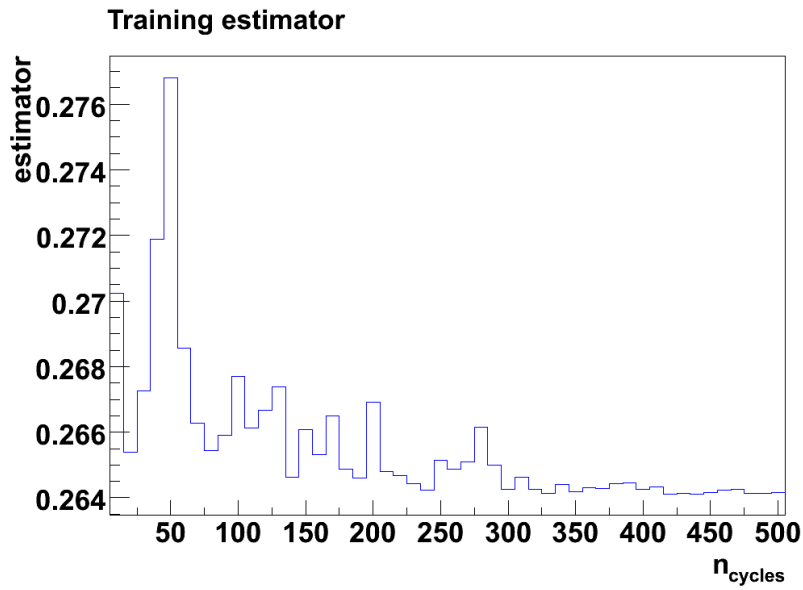
Figure 5.22: Error estimator, e, of the ANN as function of training cycles, m_{cycles}.
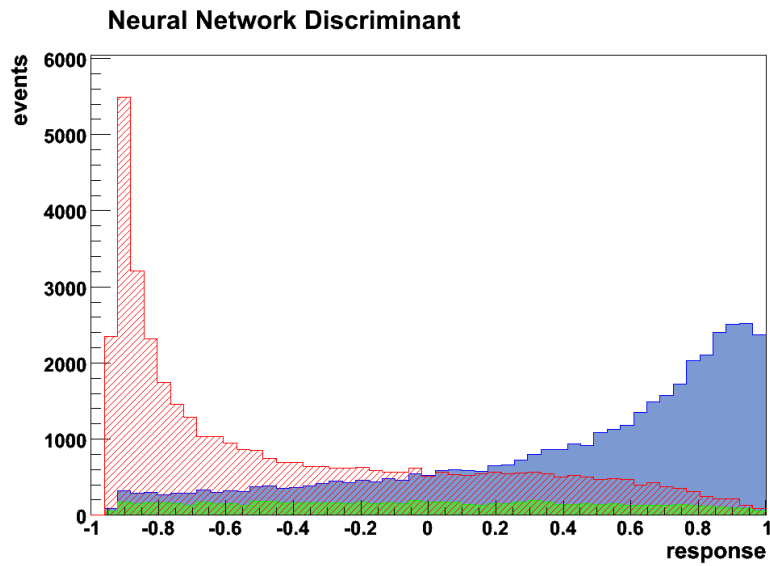
Figure 5.23: Discriminant output after training of the neural network. The misidentified neutral pion candidate distribution is shown in red, the distribution of neutral pion candidates matched to a single photon in green and the distribution of neutral pion candidates matched to a neutral pion is shown in blue.

Chapter 6

Reconstruction Performance

The performance of the reconstruction algorithm for neutral pions is evaluated in this chapter using the efficiency to reconstruct the correct number of neutral pions for $\tau^\pm \to \pi^\pm \nu_\tau$, $\tau^\pm \to \rho^\pm \nu_\tau$ and $\tau^\pm \to a_1^\pm \nu_\tau$ decays. Having reviewed these quantities the performance has been studied as a function of the tau-decay kinematics. The quality of the reconstruction of neutral pions is checked using the the energy and direction resolutions. In addition the reconstruction of the intermediate resonances is evaluated.

In the following section the neural network is used. In addition the one dimensional selection criteria method is compared to the neural network method. All results shown are obtained using the $Z \to \tau^\pm \tau^\mp$ sample.

6.1 Neutral Pion Reconstruction Efficiency

As shown in Section 1.4, the number of final state neutral pions in one-prong tau decays indicates to a good approximation (neglecting decay channels with a branching fraction smaller than one percent), whether the tau lepton decayed via $\tau^\pm \to \pi^\pm \nu_\tau$, $\tau^\pm \to \rho^\pm \nu_\tau$ or $\tau^\pm \to a_1^\pm \nu_\tau$. It is thus useful to define an efficiency ϵ_D^N for reconstructing N neutral pions for the generated decay mode $D \in \{\pi, \rho, a_1\}$, where in the following π, ρ and a_1 are used as acronyms for the $\tau^\pm \to \pi^\pm \nu_\tau$, $\tau^\pm \to \rho^\pm \nu_\tau$ and $\tau^\pm \to a_1^\pm \nu_\tau$ decays:

$$\epsilon_D^N = \frac{\text{number of generated decays D with N reconstructed } \pi^0}{\text{number of generated decays D}} \ . \tag{6.1}$$

In addition, an analogous efficiency is defined with the additional requirement that the N reconstructed neutral pions are matched to generated neutral pions:

$$\epsilon_{D,\,\text{truth-matched}}^N = \frac{\text{number of gen. decays D with N reco. and truth-matched } \pi^0}{\text{number of generated decays D}} \ . \tag{6.2}$$

The efficiency ϵ_D^N shows how well the different tau-lepton decay modes can be separated using the neutral pion reconstruction algorithm, while $\epsilon_{D,\,\text{truth-matched}}^N$ includes the additional information whether the neutral pions are correctly reconstructed.

6.1.1 Optimizing the Neural Network Selection

The neutral pion efficiency ϵ_D^N obtained with the neural network depends on the value of the discriminant used to distinguish between true and misidentified neutral pion candidates. In order to quantify the influence of the selection cuts on the discriminant on ϵ_D^N

and $\epsilon_{D,\text{truth-matched}}^N$, their dependence on the discriminant selection is shown in Fig. 6.1 and 6.2 separately for each decay mode. As can be seen from the plots, the efficiency ϵ_D^N for the $\tau^\pm \to \pi^\pm \nu_\tau$ decay increases with tighter selection cuts, and the efficiency ϵ_D^N for $\tau^\pm \to a_1^\pm \nu_\tau$ decays decreases. The efficiency ϵ_D^N for $\tau^\pm \to \rho^\pm \nu_\tau$ decays is nearly constant for selection cuts between -0.8 and 0.2 and decreases for larger and smaller selection cuts.

This behavior is easy to understand: if the selection cut on the discriminant is close to the value one , the efficiency ϵ_D^N for $\tau^\pm \to \pi^\pm \nu_\tau$ decays will increase, since almost all misidentified neutral pions will be suppressed. On the other hand many true neutral pions will be discarded and thus the efficiencies for $\tau^\pm \to \rho^\pm \nu_\tau$ and $\tau^\pm \to a_1^\pm \nu_\tau$ decays will decrease. Selection cuts close to -1 will yield contrary results: decreasing $\tau^\pm \to \pi^\pm \nu_\tau$ and increasing $\tau^\pm \to \rho^\pm \nu_\tau$ and $\tau^\pm \to a_1^\pm \nu_\tau$ efficiencies. An appropriate selection cut can be chosen to meet the need of each physics analysis. In this study a selection cut of -0.6 on the discriminant is selected as working hypothesis. It provides a good efficiency ϵ_D^N for $\tau^\pm \to \pi^\pm \nu_\tau$, while maintaining a reasonable efficiency for the $\tau^\pm \to a_1^\pm \nu_\tau$ decay.
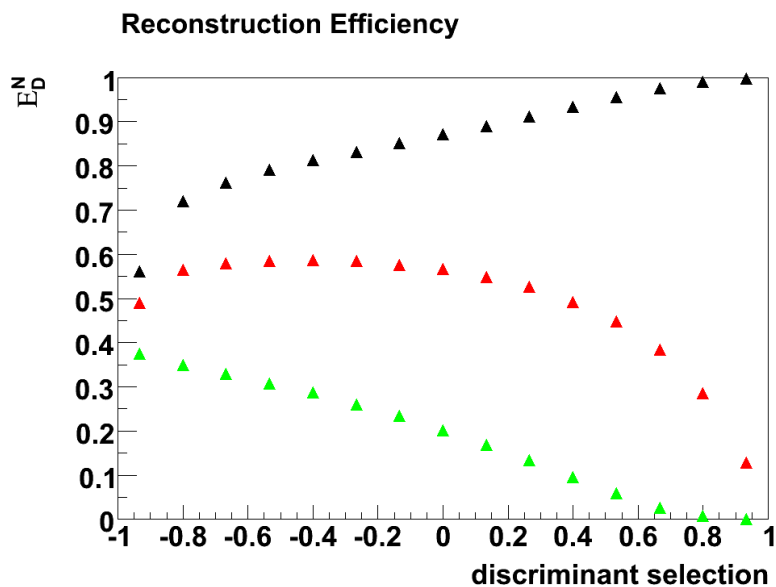
Figure 6.1: Efficiency ϵ_D^N as function of the ANN discriminant selection. The efficiencies ϵ_π^0 (black), ϵ_ρ^1 (red) and $\epsilon_{a_1}^2$ (green) are shown.

6.1.2 Reconstruction Efficiency

The efficiencies ϵ_D^N and $\epsilon_{D,\text{truth-matched}}^N$ are presented as "efficiency matrices" in Tab. 6.1 and 6.2, respectively. The index N denotes the column of the matrix (i.e. the number of reconstructed neutral pions) and the index D the row (i.e. the generated tau-lepton decay mode). The statistical errors are on the order of $\approx 0.5\%$ and are thus neglected in the table.

It is trivial that the efficiency $\epsilon_{D\,\text{truth-matched}}^N$ for $\tau^\pm \to \pi^\pm \nu_\tau$ is 100%, since no reconstructed neutral pions is truth-matched. In 23.08% of all tau lepton decays through a ρ-resonance no truth matched neutral pion candidate is found. Events where the neutral pion carries only a small fraction of the tau lepton energy are the suspected cause for this (compare also Fig. 6.6

Reconstruction Efficiency
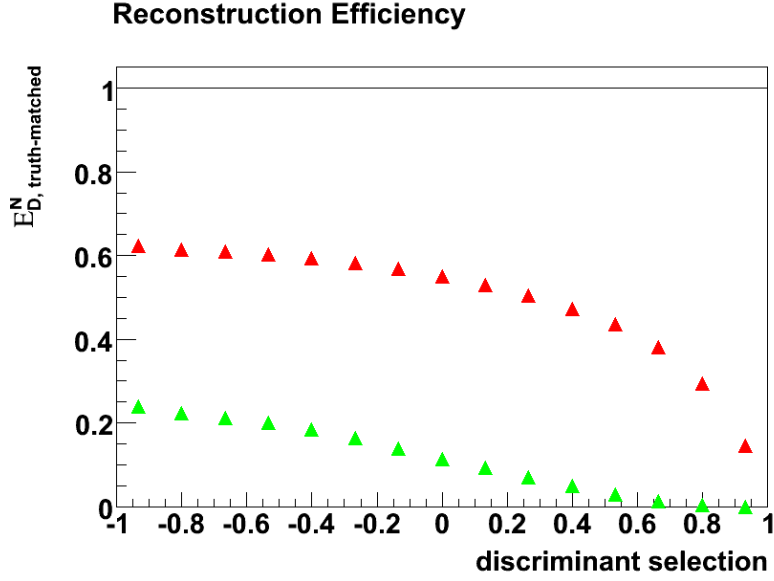
Figure 6.2: Efficiency $\epsilon^N_{D\,\text{truth-matched}}$ as function of the ANN discriminant selection. Shown is $\epsilon^0_{\pi,\,\text{truth-matched}}$, $\epsilon^1_{\rho,\,\text{truth-matched}}$ (red) and $\epsilon^2_{a_1,\,\text{truth-matched}}$ (green). The black line at one is $\epsilon^0_{\pi,\,\text{truth-matched}}$.

Decay Mode	$0\,\pi^0$ **rec.**$[\%]$	$1\,\pi^0$ **rec.**$[\%]$	$\geq 2\,\pi^0$ **rec.**$[\%]$
$\tau^\pm \to \pi^\pm \nu_\tau$	100.00	0.00	0.00
$\tau^\pm \to \rho^\pm \nu_\tau$	36.79	60.56	2.65
$\tau^\pm \to a_1^\pm \nu_\tau$	25.04	52.43	22.53

Table 6.1: Efficiencies $\epsilon^N_{D,\,\text{truth-matched}}$ for $\tau^\pm \to \pi^\pm \nu_\tau$, $\tau^\pm \to \rho^\pm \nu_\tau$ and $\tau^\pm \to a_1^\pm \nu_\tau$ decays.

decay mode	$0\,\pi^0$ **rec.**$[\%]$	$1\,\pi^0$ **rec.**$[\%]$	$\geq 2\,\pi^0$ **rec.**$[\%]$
$\tau^\pm \to \pi^\pm \nu_\tau$	77.72	19.53	2.75
$\tau^\pm \to \rho^\pm \nu_\tau$	24.53	58.24	17.23
$\tau^\pm \to a_1^\pm \nu_\tau$	17.01	41.51	41.48

Table 6.2: Efficiencies ϵ^N_D for $\tau^\pm \to \pi^\pm \nu_\tau$, $\tau^\pm \to \rho^\pm \nu_\tau$ and $\tau^\pm \to a_1^\pm \nu_\tau$ decays.

in Section 6.1.3). In these cases the uncertainty on the charged pion energy measurement in the electromagnetic calorimeter, which is dominated by the energy uncertainty in the hadronic calorimeter $\frac{\sigma(E)}{E} \approx \frac{50\,\%}{\sqrt{E(\,\mathrm{GeV})}} \oplus 5\,\%$, exceeds the total amount of neutral pion energy and hence the reconstruction of the neutral pion is almost impossible. The photons from the neutral pion decays create two distinct clusters in the calorimeter in $\approx 2\,\%$ of all $\tau^{\pm} \to \rho^{\pm}\nu_{\tau}$ decays. Only $\approx 23\,\%$ of tau-lepton decays with two neutral pions in the final state can be reconstructed correctly as a $\tau^{\pm} \to a_1^{\pm}\nu_{\tau}$ with truth-matching of the neutral pions, and $25\,\%$ of them are reconstructed without any neutral pions. As discussed above neutral pions with low transverse momenta are difficult to reconstruct. This could explain the decreased efficiencies ϵ_D^N for $\tau^{\pm} \to a_1^{\pm}\nu_{\tau}$ decays with respect to $\tau^{\pm} \to \rho^{\pm}\nu_{\tau}$ decays, since the neutral pions from $\tau^{\pm} \to a_1^{\pm}\nu_{\tau}$ decays have in general smaller transverse momenta than neutral pions from $\tau^{\pm} \to \rho^{\pm}\nu_{\tau}$ decays.

The efficiencies ϵ_D^N are smaller than $\epsilon_{D\,\mathrm{truth-matched}}^N$ for the $\tau^{\pm} \to \pi^{\pm}\nu_{\tau}$ and $\tau^{\pm} \to \rho^{\pm}\nu_{\tau}$ decays, since the total number of neutral pions is larger. Therefore only about $77\,\%$ of all $\tau^{\pm} \to \pi^{\pm}\nu_{\tau}$ decays and $58\,\%$ of all $\tau^{\pm} \to \rho^{\pm}\nu_{\tau}$ decays are now identified correctly. But the larger number of reconstructed neutral pions increases the efficiency ϵ_D^N for the $\tau^{\pm} \to a_1^{\pm}\nu_{\tau}$ decay from $\approx 23\,\%$ to $\approx 41\,\%$.

6.1.3 Dependence on Kinematics of Tau-Decay

Several studies have been made to check the dependence of the neutral pion reconstruction on tau-decay kinematics. These studies were carried out using $\tau^{\pm} \to \rho^{\pm}\nu_{\tau}$ decays, i.e. studying the effect on ϵ_{ρ}^1. Since these decays have only one neutral pion, the interpretation is easier.

- $\eta^{\tau_{\mathrm{vis}}}$, $E_T^{\tau_{\mathrm{vis}}}$: Studying the dependence of $\eta^{\tau_{\mathrm{vis}}}$ and $p_T^{\tau_{\mathrm{vis}}}$ will show the impact of different η-regions and the prospects of improving tau-lepton reconstruction at low transverse momenta.

- p_T^{Track}, $E_T^{\pi^0}/E_T^{\rho}$: If the neutral pions carry only a small fraction of the total visible tau-energy, the error on the E_{ECAL}^{π} calculation may exceeds the total neutral pion energy. Thus the reconstruction will be difficult or even impossible.

- $\Delta R\,(\gamma, \gamma)$: The neutral pion reconstruction is optimized for reconstructing merged photon clusters. The impact of this choice can be studied by looking at the efficiency ϵ_D^N as a function of the distance between the two photons.

- $\Delta R\,(\pi^{\pm}, \pi^0)$: The subtraction of the charged pion energy does not affect neutral pion reconstruction for large distances between the charged and neutral pion. Thus the dependence of the efficiency on the distance can be used to study the influence of the subtraction on the reconstruction.

Fig. 6.3 shows the dependence of the efficiency ϵ_{ρ}^1 on the η of the tau jet. The distribution is almost flat. Also the dependence on the E_T of the tau jet does not have a large influence on the efficiency ϵ_D^N. Only the first bin shows a slight drop for low E_T tau jets.

ϵ_{ρ}^1 drops with rising transverse momenta of the charged pion. Since the visible energy for tau leptons from $\tau^{\pm} \to \rho^{\pm}\nu_{\tau}$ decays is split between the charged and the neutral pion, large charged pion transverse momenta imply small transverse momenta for the neutral pions. As outlined above it is more difficult to reconstruct low p_T neutral pions as the error on E_{ECAL}^{π}
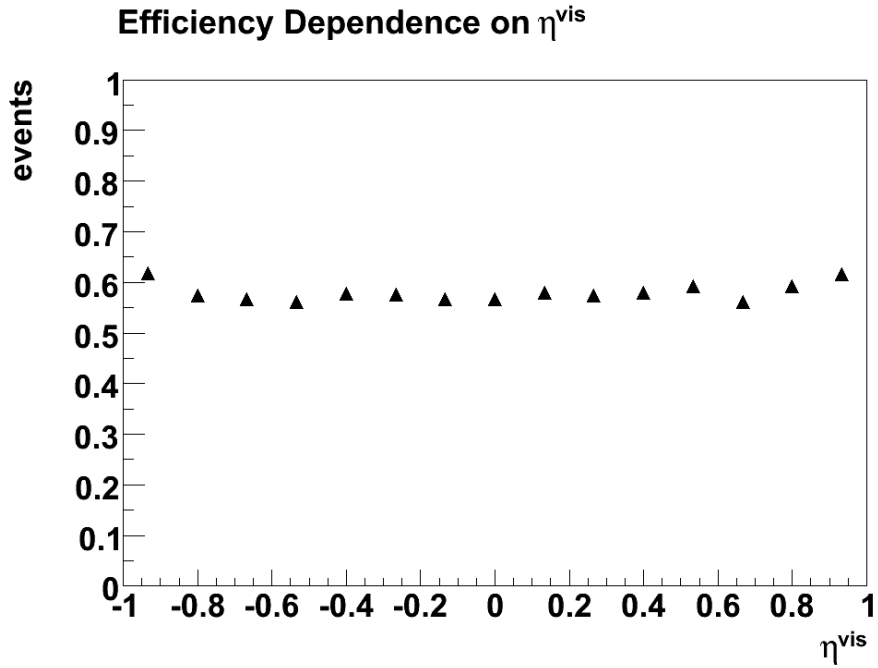
Figure 6.3: Efficiency ϵ_D^N for $\tau^\pm \to \rho^\pm \nu_\tau$ decays as a function of the tau-lepton η^{vis}.
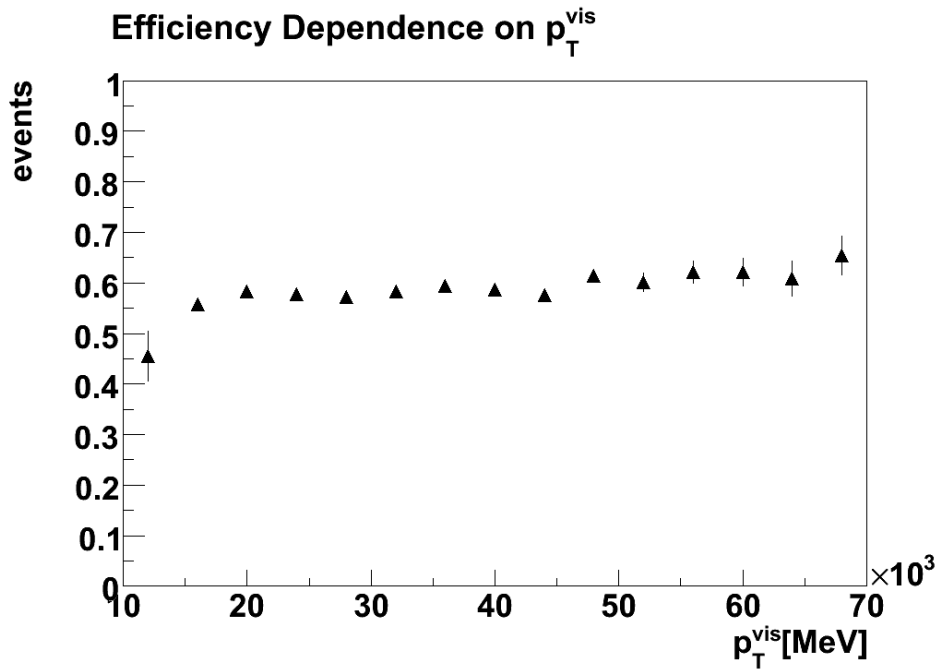
Figure 6.4: Efficiency ϵ_D^N for $\tau^\pm \to \rho^\pm \nu_\tau$ decays as a function of the tau-lepton p_T^{vis}.

gets comparable to the neutral pion energy. The distribution of the efficiency ϵ_ρ^1 as a function of $E_T^{\pi^0}/E_T^{\tau_{\mathrm{vis}}}$ shown in Fig. 6.6 verifies this. The efficiency drops significantly for small neutral pion energy fractions.

Efficiency Dependence on p_T^{Track}
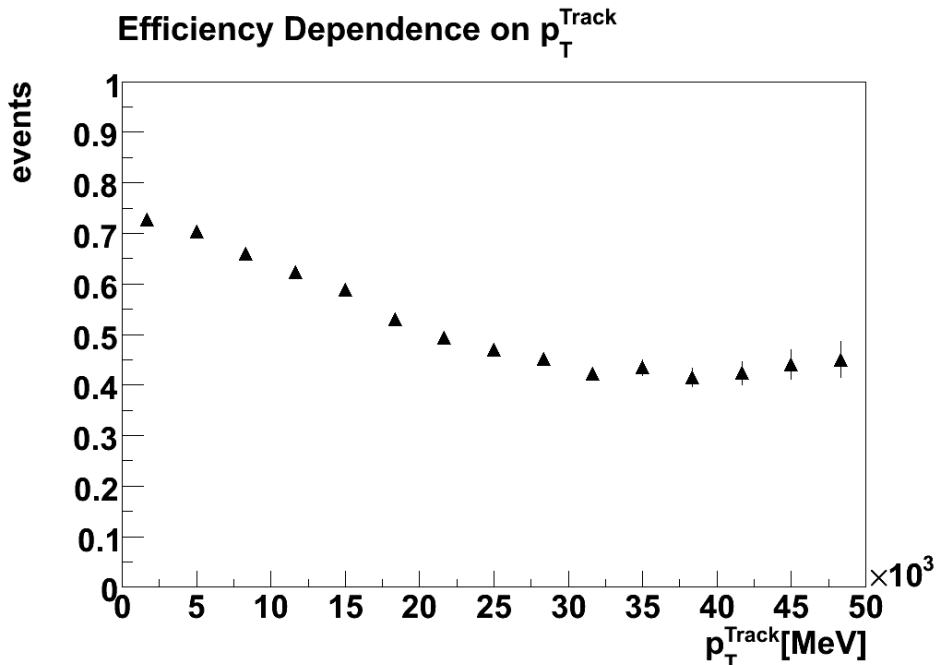
Figure 6.5: Efficiency ϵ_D^N for $\tau^\pm \to \rho^\pm \nu_\tau$ decays as a function of the transverse momenta of the charged pion track.

The decreasing performance for low neutral pion energies could also be caused by the fact, that the reconstruction is optimized to reconstruct calorimeter cluster, formed by both photons of the neutral pion decay. Since the opening angle between the two photons emitted by the neutral pion decay depends on the transverse momentum of the neutral pion, the reconstruction of a merged neutral pion cluster may be impossible for low energy neutral pions. The distribution shown in Fig. 6.7 indicates that the performance drops for big opening angles, since the two photons make distinct clusters in the calorimeter. This problem could be compensated in further studies by trying to recombine the two separate photon clusters to a neutral pion by looking at the invariant mass (Chapter 7).

Another dependence which is studied is the effect of the distance between the neutral and the charged pion on the efficiency ϵ_D^N. If this distance is large enough the subtraction should have almost no influence on the reconstruction. Therefore the difference in efficiency between small and large distances can give a hint about how well the neutral pion reconstruction algorithm works in the region where the reconstruction of the neutral pion depends strongly on the subtraction of the charged pion energy. The distribution in Fig. 6.8 shows that the reconstruction performance depends only weakly on the distance of the track to the neutral pion only a slight drop is seen in the first bin. This indicates that the subtraction performs well and allows the reconstruction of neutral pions even if their energy depositions overlap with the ones from the charged pion.
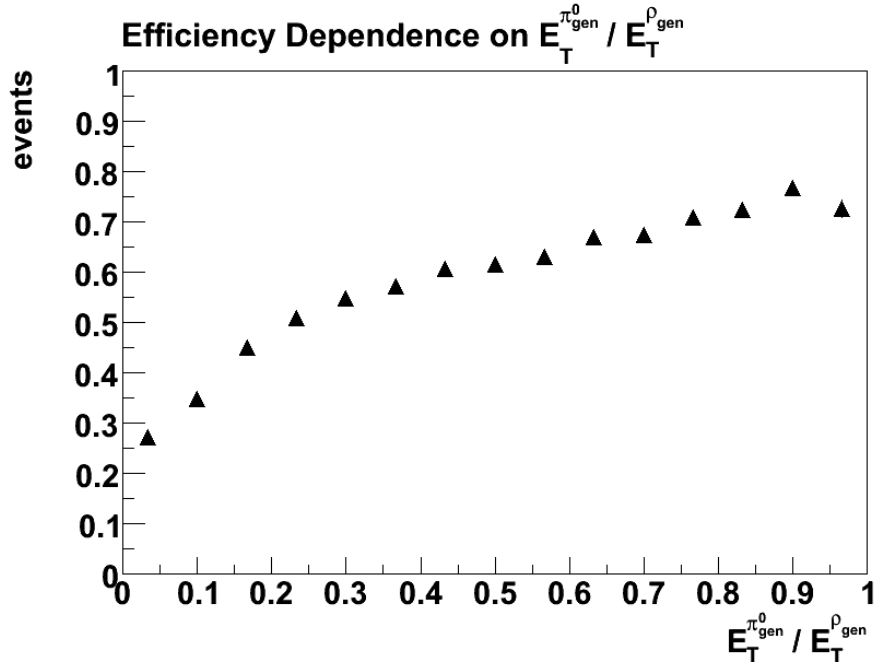
Figure 6.6: Efficiency ϵ_D^N as a function of the transverse energy ratio of π^0 and ρ.
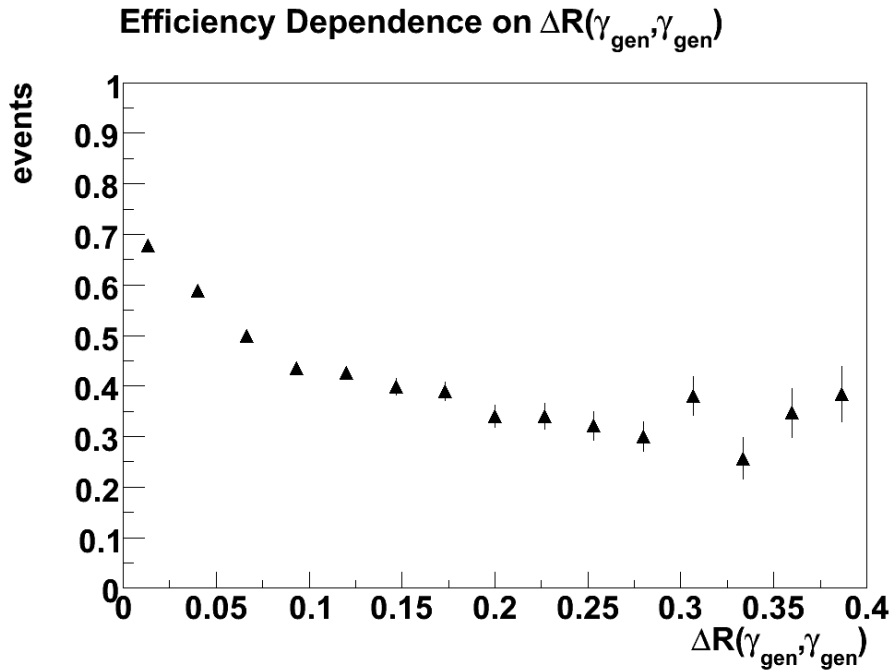
Figure 6.7: Efficiency ϵ_D^N as a function of the distance between the two photons from the neutral pion decay.
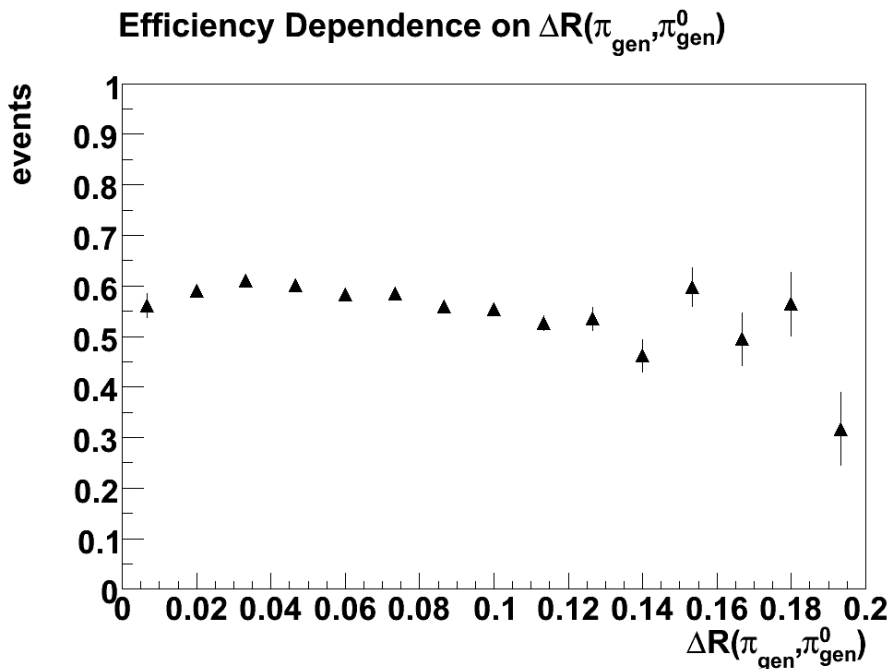
Figure 6.8: Efficiency ϵ_D^N as a function of the distance of the track to the neutral pion.

6.2 Neutral Pion Resolution and Intermediate Resonances

To study the quality of the neutral pion reconstruction, Fig. 6.9 shows the resolution of the reconstructed neutral pion's transverse energy, pseudorapidity and azimuthal angle. In these distributions only tau-lepton decays with the correct number of reconstructed neutral pions are used, i.e. $\tau^\pm \to \rho^\pm \nu_\tau$ or $\tau^\pm \to a_1^\pm \nu_\tau$ decays with one or two reconstructed neutral pions, respectively.

The transverse energy, pseudorapidity and azimuthal angle of reconstructed neutral pions are compared with those of the generated neutral pions. The central region of each resolution distribution was fitted using a Gaussian function. To quantify the energy and direction resolution of neutral pion reconstruction the mean (μ) and sigma (σ) of the fitted Gaussian functions are given in the top right corner of each plot.

The pseudorapidity and azimuthal angle fits are nicely centered around zero and show no bias. The obtained resolutions are on the order of the calorimeter cell size for both the $\tau^\pm \to \rho^\pm \nu_\tau$ and the $\tau^\pm \to a_1^\pm \nu_\tau$ decays. In contrast the transverse energy shows a shift of $-5.3\,\%$ for the $\tau^\pm \to \rho^\pm \nu_\tau$ and $-6.7\,\%$ for the $\tau^\pm \to a_1^\pm \nu_\tau$ decay. As shown, neglecting the third layer of the electromagnetic calorimeter for neutral pion reconstruction only introduces a bias of $\approx 1\,\%$. In addition the subtraction of slightly too much charged pion energy, could explain the shift. Another possible reason may that the calibration for neutral pion clusters is not optimal. The tail towards small energies may be caused by the reconstruction of a neutral pion candidate from a single photon, since it carries less energy than the neutral pion.
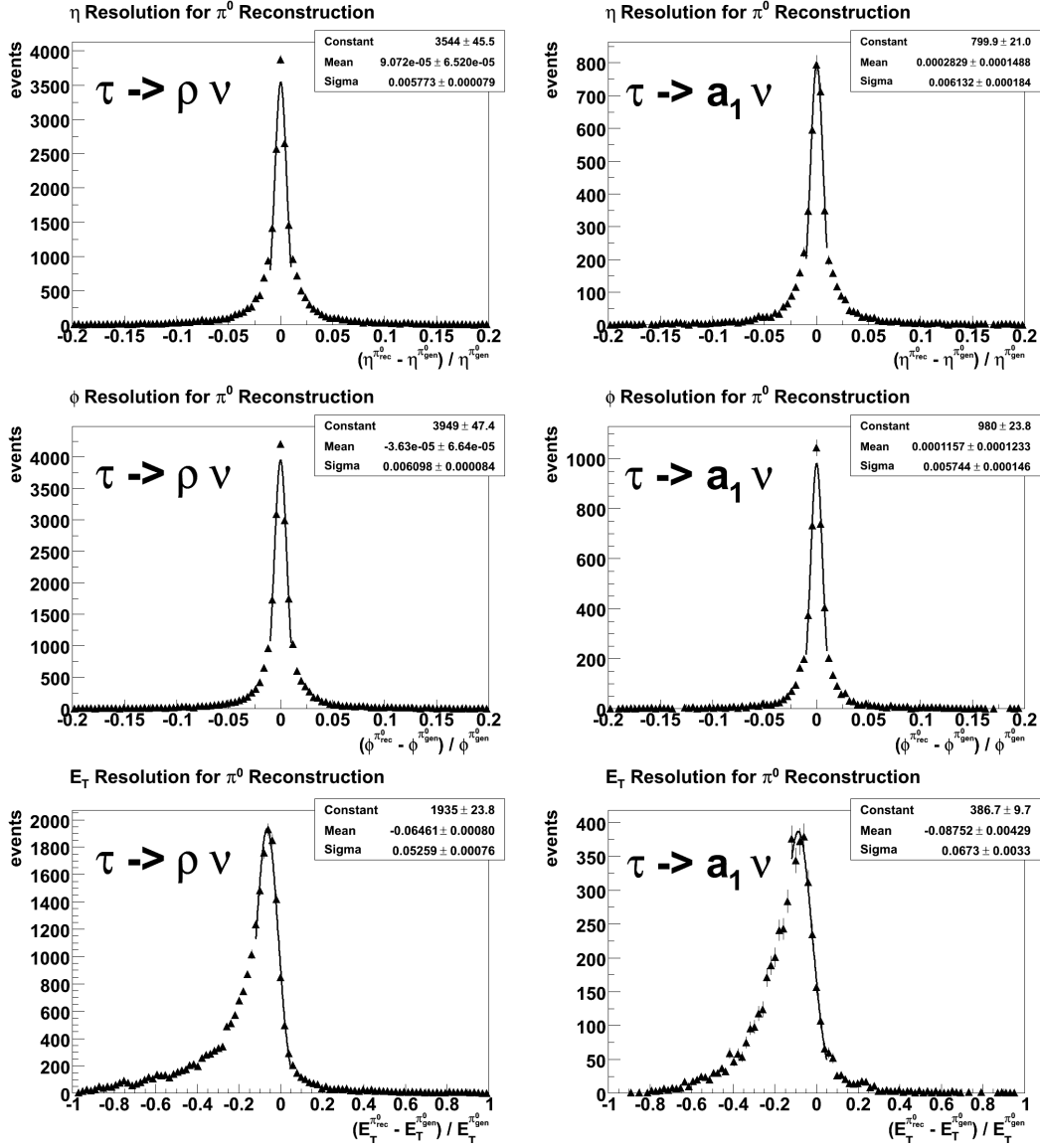
Figure 6.9: η, ϕ and E_T resolution of reconstructed neutral pions for $\tau^{\pm} \rightarrow \rho^{\pm}\nu_{\tau}$ decays on the left hand and $\tau^{\pm} \rightarrow a_1^{\pm}\nu_{\tau}$ decays on the right hand.

6.2.1 Reconstruction of Intermediate Resonances

The reconstruction of the invariant mass of the intermediate ρ and a_1 resonances in the hadronic tau-lepton decay is another cross check of the neutral pion reconstruction performance. It is calculated by combining the track ($\pi^\pm$) and neutral pion measurements, e.g. $E_\rho = E_{\text{Track}} + E_\pi^0$. Thus it depends on the E_T reconstruction and the reconstruction of the angles between charged and neutral pions. The invariant mass distribution can also be used in physics analyses as an additional selection criterion to enhance the signal over background ratio.

The invariant mass of the intermediate resonance is calculated for two scenarios:

1. all events with a generated $\tau^\pm \to \rho^\pm \nu_\tau$ ($\tau^\pm \to a_1^\pm \nu_\tau$) decay and one (two) reconstructed neutral pion(s)

2. all events with one (two) reconstructed neutral pion(s)

The first is a performance check for the ideal case where the $\tau^\pm \to \rho^\pm \nu_\tau$ decay is correctly identified. The second does not use generator information and is therefore also possible with data. All distributions are shown in Fig. 6.10 and 6.11.
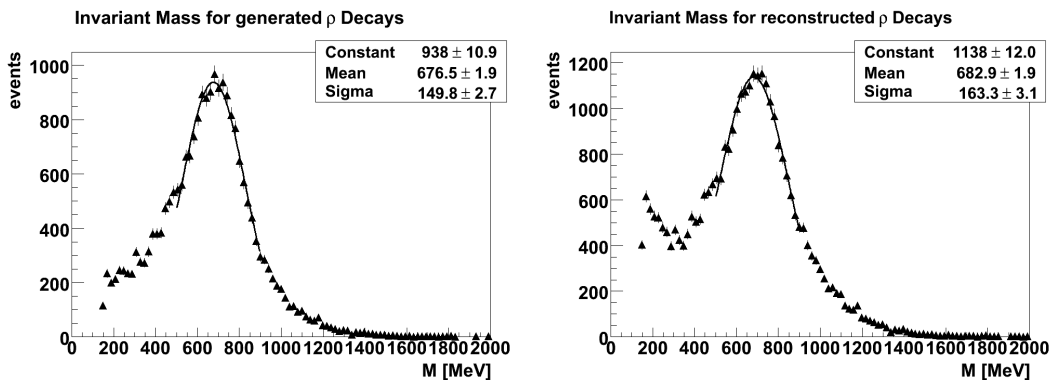
Figure 6.10: Invariant mass distribution for generated $\tau^\pm \to \rho^\pm \nu_\tau$ decays with one reconstructed neutral pion on the left side and all tau lepton decays with one reconstructed neutral pion on the right.

The currently best values for the ρ invariant mass and natural width are $m_\rho = 775.49 \pm 0.34\,\text{MeV}$ and $\Gamma_\rho = 149.4 \pm 1.0\,\text{MeV}$ and for the a_1 the best values are $m_{a_1} = 1230 \pm 40\,\text{MeV}$ and $\Gamma = 250$ to $600\,\text{MeV}$ [8]. In both scenarios the invariant mass of the ρ and the a_1 can be reconstructed reasonably well. The peak of the intermediate resonance invariant mass distribution is slightly shifted towards smaller energies. Part of this effect can be contributed to the underestimation of the energy of reconstructed neutral pion candidates. For the ρ decay this shift is around $-100\,\text{MeV}$ and for the a_1 decay around $-200\,\text{MeV}$. The comparison between the distributions from the first scenario and the distributions from the second one does not yield big differences in the core region only the masses are slightly smaller. But a peak is observable towards smaller energies and the tail for energies well above the central peak grows.
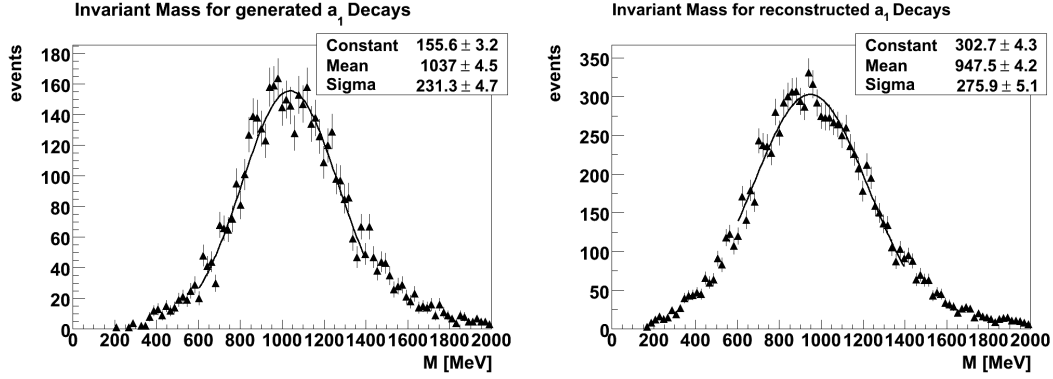
Figure 6.11: Invariant mass distribution for generated $\tau^{\pm} \to a_1^{\pm} \nu_\tau$ decays with two reconstructed neutral pion on the left side and all tau lepton decays with two reconstructed neutral pion on the right.

6.2.2 Intermediate Resonance Resolution

The intermediate resonances ρ and a_1 in tau-lepton decays are reconstructed by combining track and neutral pion measurements. Fig. 6.12 shows the E_T-, η- and ϕ-resolution obtained from $\tau^{\pm} \to \rho^{\pm} \nu_\tau$ decays with one and $\tau^{\pm} \to a_1^{\pm} \nu_\tau$ decays with two reconstructed neutral pions. The reconstruction of the intermediate resonances works with a very good resolutions. Only the energy shows a small bias towards smaller energies, which is caused by the neutral pion reconstruction.

6.3 Comparison with an Already Existing Algorithm

As presented in Section 3.3 a neutral pion subshower algorithm exists for the reconstruction of "track-seeded" tau-lepton candidates. The results of the reconstruction algorithm presented in this thesis are compared to that of the already existing reconstruction. Tab. 6.3 lists the fraction of correctly reconstructed single-prong tau-lepton decays for both algorithms. The algorithm could improve the efficiency ϵ_D^N for $\tau^{\pm} \to \pi^{\pm} \nu_\tau$ and $\tau^{\pm} \to \rho^{\pm} \nu_\tau$ decays. These decays appear in about 72 % of all hadronic single-prong decays of tau leptons. However a drop in the efficiency ϵ_D^N for the $\tau^{\pm} \to a_1^{\pm} \nu_\tau$ decay is observed, which is due to a harsher rejection of misidentified neutral pions.

Decay Mode	Reconstructed	
	New Algorithm[%]	Existing Algorithm[%]
$\tau^{\pm} \to \pi^{\pm} \nu_\tau$	77.7	66.4
$\tau^{\pm} \to \rho^{\pm} \nu_\tau$	58.2	50.9
$\tau^{\pm} \to a_1^{\pm} \nu_\tau$	41.5	52.8

Table 6.3: Efficiencies ϵ_D^N for neutral pions from the algorithm presented in this thesis and an already existing one used for track-seeded tau candidates. Numbers for the existing algorithm are taken from [18].

The resolutions obtained from the neutral pion reconstruction are listed in Tab. 6.4 for the
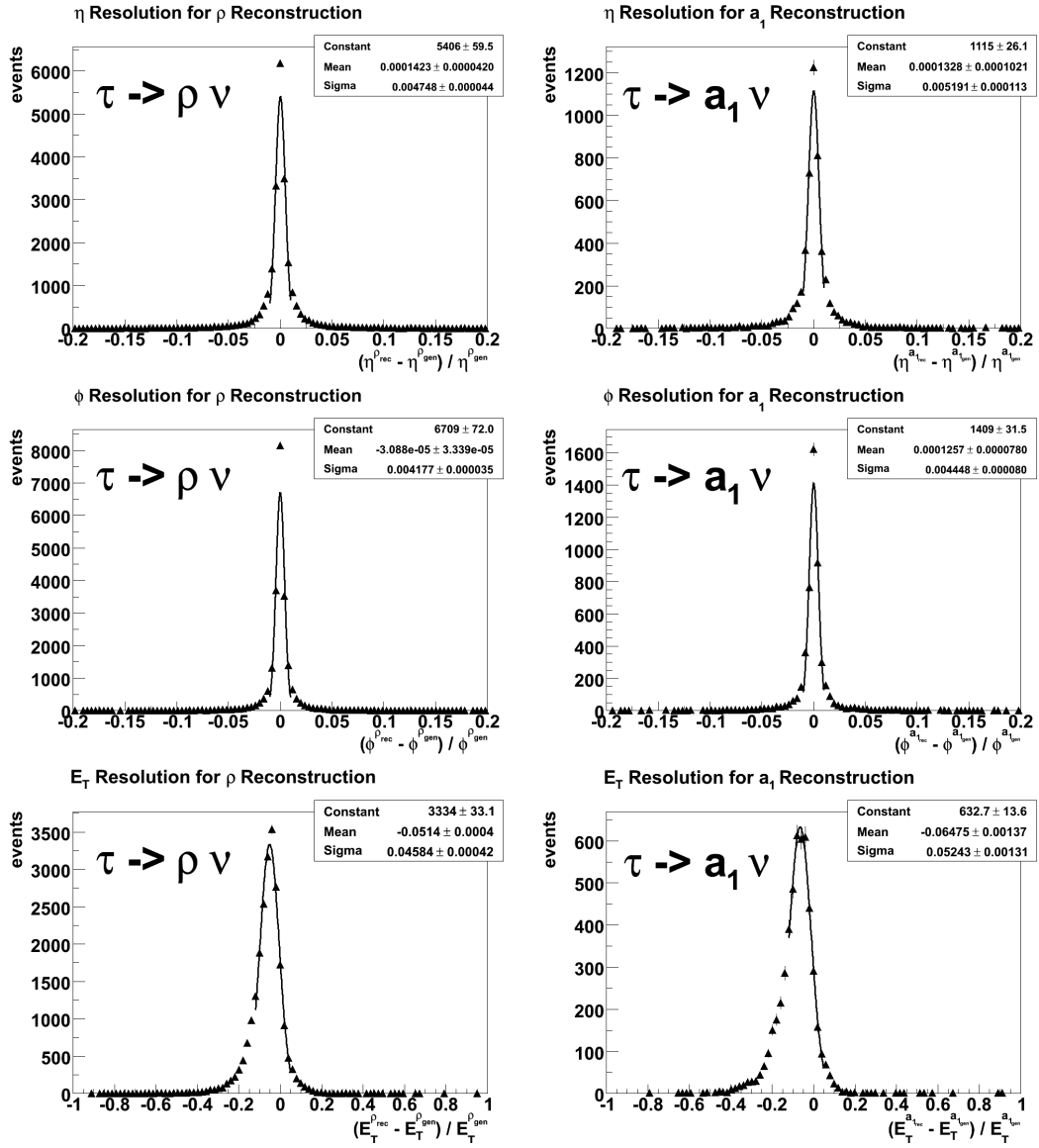
Figure 6.12: η-, ϕ- and E_T-resolution of the combined system track and reconstructed neutral pions for $\tau^\pm \to \rho^\pm \nu_\tau$ decays on the left hand and $\tau^\pm \to a_1^\pm \nu_\tau$ decays on the right hand.

new algorithm presented in this study and the already existing one. While the η resolution is comparable or slightly worse, all other results improved significantly. The difference between the track- and calo-seeded approach and the different software release (12.0.6) do not make a big difference for the reconstruction of neutral pion.

	$\sigma\left(\eta_\pi^0\right)$	$\sigma\left(\phi_\pi^0\right)$	$\sigma\left(E_T^{\pi^0}\right)$	$\sigma\left(E_T^\rho\right)$
New Algorithm[%]	0.577 ± 0.008	0.610 ± 0.008	5.26 ± 0.08	4.58 ± 0.04
Ex. Algorithm[%]	0.56 ± 0.02	1.4 ± 0.04	14 ± 0.6	6.8 ± 0.3

Table 6.4: Resolutions of the neutral pion reconstruction from $\tau^\pm \to \rho^\pm \nu_\tau$ decays for the algorithm presented in this study and an already existing algorithm. The numbers are taken from [18].

6.4 Comparison with the Cut-Based Approach for First Data

As shown in Section 5.5.3 a suppression of misidentified neutral pions for first data was implemented using a cut-based selection on three shower shape variables of neutral pion candidates. In order to evaluate the performance and thus the feasibility of this approach, the efficiencies and resolutions are studied in the same way as for the suppression using the neural network method. The efficiencies ϵ_D^N are shown in Tab. 6.5. Again, the rows denote the generated tau-lepton decay mode and the columns the number of reconstructed neutral pion candidates. The performance of both approaches is comparable. The cut-based approach uses harder selection criteria thus the efficiency matrix is slightly shifted to the right yielding increased $\tau^\pm \to \pi^\pm \nu_\tau$ and decreased slightly $\tau^\pm \to a_1^\pm \nu_\tau$ efficiencies.

decay mode	$0\,\pi^0$ **rec.**[%]	$1\,\pi^0$ **rec.**[%]	$\geq 2\,\pi^0$ **rec.**[%]
$\tau^\pm \to \pi^\pm \nu_\tau$	84.15	13.50	2.35
$\tau^\pm \to \rho^\pm \nu_\tau$	25.67	59.14	15.19
$\tau^\pm \to a_1^\pm \nu_\tau$	16.62	43.48	39.90

Table 6.5: Efficiencies ϵ_D^N obtained with the cut-based approach developed for first data.

In addition to the efficiency ϵ_D^N, the resolutions of the neutral pion direction and energy, as well as the resolution of the reconstructed intermediate resonances of the tau-lepton decay have been studied for the cut-based misidentified neutral pion suppression. The resolution distributions are shown in App. A.3 and the results are listed in Tab. 6.6 together with the results presented above for the suppression using the neural network with the neutral pion shower shape variables. The comparison yields, that the resolutions of the neural network approach are slightly better, but the cut-based approach performs nonetheless very well.

It is still surprising, that the simple cut-based approach shows comparable or slightly increasing efficiencies ϵ_D^N. The performance of the neural network will be studied further in order to understand this effect.

	$\sigma\left(\eta_\pi^0\right)$	$\sigma\left(\phi_\pi^0\right)$	$\sigma\left(E_T^{\pi^0}\right)$	$\sigma\left(E_T^\rho\right)$
Cut-based[%]	0.639 ± 0.008	0.648 ± 0.007	5.30 ± 0.008	4.65 ± 0.05
Neural Network[%]	0.577 ± 0.008	0.610 ± 0.008	5.26 ± 0.08	4.58 ± 0.04

Table 6.6: Resolutions of the neutral pion reconstruction from $\tau^\pm \to \rho^\pm \nu_\tau$ decays for the cut-based and the neural-network approach for suppressing misidentified neutral pions.

Chapter 7

Plans for Validation with Data and Further Improvements

7.1 Validation with Data

Studies carried out on Monte-Carlo samples must be validated with real data to reveal deficiencies in Monte-Carlo simulation. At the moment the charged pion shower development and the shapes of neutral pion clusters in the electromagnetic calorimeter are obtained from Monte-Carlo. Thus discrepancies between data and simulation would affect the charged pion energy subtraction and the suppression of misidentified neutral pions.

To validate the shower development of the charged pion in the electromagnetic calorimeter a sample of isolated charged pions is needed. This sample can be obtained from data by searching for isolated tracks, which are mostly pions. To ensure that the track originated from a pion, the energy deposited in the calorimeter must be consistent with the one calculated from the track transverse momentum using the pion mass hypothesis.

The agreement of shower-shape variables for neutral pions in the electromagnetic calorimeter is reflected in the agreement of the discriminant used for misidentified neutral pion suppression. In order to obtain the discriminant, a sample of true and misidentified neutral pions is needed. Since we expect the misidentified neutral pions to result mainly from differences between the actual hadronic shower development and the one used for subtraction, the simplest and most intuitive approach is to use hadronic tau-lepton decays as starting point.

A clean source of tau leptons is expected to be the Z-boson decay into two tau leptons ($q\bar{q} \to Z \to \tau^{\pm}\tau^{\mp}$), where at least one of the tau leptons is required to decay hadronically. Already with first data the $Z \to \tau^{\pm}\tau^{\mp}$ sample will be large enough (cf. Section 1.3.1) to carry out this studies. The hadronic decay of both tau leptons is hard to trigger, but $Z \to \tau^{\pm}\tau^{\mp}$ can be triggered efficiently, if one of the tau-leptons is required to decay into an electron or muon. Another advantage is that QCD background can be efficiently suppressed by requiring that the invariant mass is consistent with that of the Z-boson calculated in the collinear approximation.

A sample of neutral pions can then be obtained by selecting isolated electromagnetic clusters belonging to a hadronic tau-lepton decay. In contrast misidentified neutral pion candidates can be obtained from $\tau^{\pm} \to \pi^{\pm}\nu_{\tau}$ decays, selected by looking for isolated tracks as described above. In addition the sample of single charged pions can be used to validate the shower development in the electromagnetic calorimeter obtained from simulation.

7.2 Systematic Uncertainties

In order to use the neutral pion subshower reconstruction in physics analysis, the influence of systematic uncertainties on the reconstruction efficiency and the resulting neutral pion resolutions must be studied. The estimation of systematic uncertainties will become meaningful once first data are taken. However based on Monte-Carlo simulation it may be useful to study the sensitivity of the algorithm to certain systematic effects.

- The energy measurement uncertainties in the hadronic calorimeter will affect the estimation, and thus the subtraction, of charged pion energy.

- The reconstruction of neutral pion candidates and their energy measurement will be affected by measurement uncertainties in the electromagnetic calorimeter.

- The uncertainties in measuring the track transverse momentum will affect the estimation of charged pion energy. Since this study is optimized for low p_T tau leptons, for which the tracking outperforms the calorimeter measurement, the effect will be small compared to calorimeter uncertainties (cf. Fig. 5.4).

- The uncertainty caused by the parameterization of the charged pion shower development. This could be tested by using another parameterization which yields a good fit, for instance the sum of three Gaussian functions instead of three exponential functions.

- Varying the fit parameters within their errors will yield the uncertainty from the fit. This uncertainty will decrease with statistics.

- Differences of the shower shapes variables between data and simulation will affect the discriminant used for suppression of misidentified neutral pion candidates and thus the reconstruction.

If differences between data and Monte-Carlo simulation are observed and they cannot be easily explained by certain problems in the reconstruction one could reweight the Monte-Carlo to the data and estimate the effects. This would give a conservative estimation of the error. However the first step is to establish agreement between data and simulation. For the determination of systematic effects the data will guide us.

7.3 Future Plans

Several extensions and improvements of the algorithm for neutral pion subshower reconstruction are possible and can be categorized in two areas.

- Verify the performance presented in this study for the implementation in the official tau-lepton reconstruction package and fully utilize the improvements over the previously implemented algorithm.

- Further improvements of the algorithm itself, e.g. extension to three-prong candidates and the electromagnetic endcap.

7.3.1 TauRec Implementation

As part of this thesis, the algorithm presented here has been implemented in the official ATLAS TauRec package. The implementation was done in the release 14.4.0 of the Athena offline reconstruction software. Currently the implementation is being validated. The results will be compared to that of the existing neutral pion reconstruction. It is expected that with the new neutral pion reconstruction and decay mode separation the tau-lepton identification can be improved. Since information about neutral pion subshowers is used for the misidentified tau-lepton suppression (cf Section 3.3) the tau-identification discriminant needs to be retrained and the resulting tau-candidate efficiency versus jet-rejection plots have to be studied.

7.3.2 Improvements of the Algorithm

Up to now the reconstruction algorithm for neutral pion subshowers has been developed for the central electromagnetic barrel and single-prong tau candidates. In order to provide neutral pion subshower information for almost all tau candidates two extensions are necessary.

- The neutral pion reconstruction must be extended to work with the electromagnetic endcap calorimeter. In principle this extension is easy, since only the parameterization of the charged pion shower development has to be checked for the endcap calorimeters. But a first implementation yielded technical problems with different formats stored cell geometries, which could be resolved. Furthermore tau-lepton candidates, which deposit energy both in the electromagnetic barrel and endcap have to be studied in detail to understand the influence of the transition between the two calorimeter parts.

- The extension to multi-prong tau-lepton decays is not problematic once the energy contribution of each charged pion to the total energy in the electromagnetic calorimeter is known, since clustering and misidentified neutral pion suppression can be used as for the single-prong case. The approach presented in Section 5.2 does not lead to a correct estimation of the energy of the charged pion for multiple tracks, since their energy depositions in the hadronic calorimeter may overlap. Thus the energy deposited in each cell must be shared between the tracks according to the tracks momenta and the distances between the tracks and the cell. As proposed in [22] for tau-leptons with n charged tracks, the energy in the electromagnetic calorimeter deposited by the k-th charged pion can be computed using

$$E_{\text{ECAL}}^{\pi_k} = E_{\text{Track}}^{\pi_k} - E_{\text{HCAL unique}}^{\pi_k} - f_k \cdot E_{\text{HCAL shared}}^{\pi_k} \ . \tag{7.1}$$

Here, $E_{\text{HCAL unique}}^{\pi_k}$ denotes the energy of cells within the cone around π_k only and $E_{\text{HCAL shared}}^{\pi_k}$ denotes the energy in cells shared by other cones. The fraction of shared energy contributing to $E_{\text{ECAL}}^{\pi_k}$, f_k, is calculated using

$$f_k = \frac{E_{\text{Track}}^{\pi_k} - E_{\text{HCAL unique}}^{\pi_k}}{\sum_l \left(E_{\text{Track}}^{\pi_l} - E_{\text{HCAL unique}}^{\pi_l} \right)} \ . \tag{7.2}$$

Using these formulas the reconstruction algorithm can be extended to three-prong[1] tau candidates.

Aside from these extensions further studies can be carried out to improve the performance of the reconstruction algorithm.

p_T-dependence: The charged pion shower development depends on the track transverse momentum. Since so far this study aims at tau leptons with low to medium transverse energy, it would be beneficial to optimize the reconstruction algorithm in intervals of E_T^{vis} or even better in intervals of p_T^{Track}. It would also be interesting to see for what maximum transverse energy value the reconstruction yields reasonable results.

Photon clusters: In its current version the reconstruction algorithm treats all reconstructed electromagnetic clusters after subtraction of the charged pion energy as neutral pion candidates. This is justified by the generally small distance between the two photons resulting in a merged cluster in 96 % of all cases (cf. Section 6.1.2). Nonetheless a separate treatment of single photon clusters can improve the reconstruction at lowest p_T. Trying to reconstruct the neutral pion invariant mass from two electromagnetic clusters would allow to recombine two photons to a neutral pion cluster. Fig. 7.1 shows the invariant mass of two calorimeter clusters matched to photons from a neutral pion obtained with the $Z \to \tau^{\pm}\tau^{\mp}$ sample. This information could then be used to correct the reconstructed decay mode by recombining the two photons to a neutral pion, or to train to different discriminants, one for photons and one for neutral pions.

TopoCluster parameters: The parameters used for the topological clustering and cluster splitting algorithm will influence the shape of the reconstructed neutral pion clusters. Thus other parameters could increase or decrease the separation power of the misidentified neutral pion suppression.

---

[1]The extensions works in principle also for five-prong candidates, but these can be neglected due to their small branching fraction.
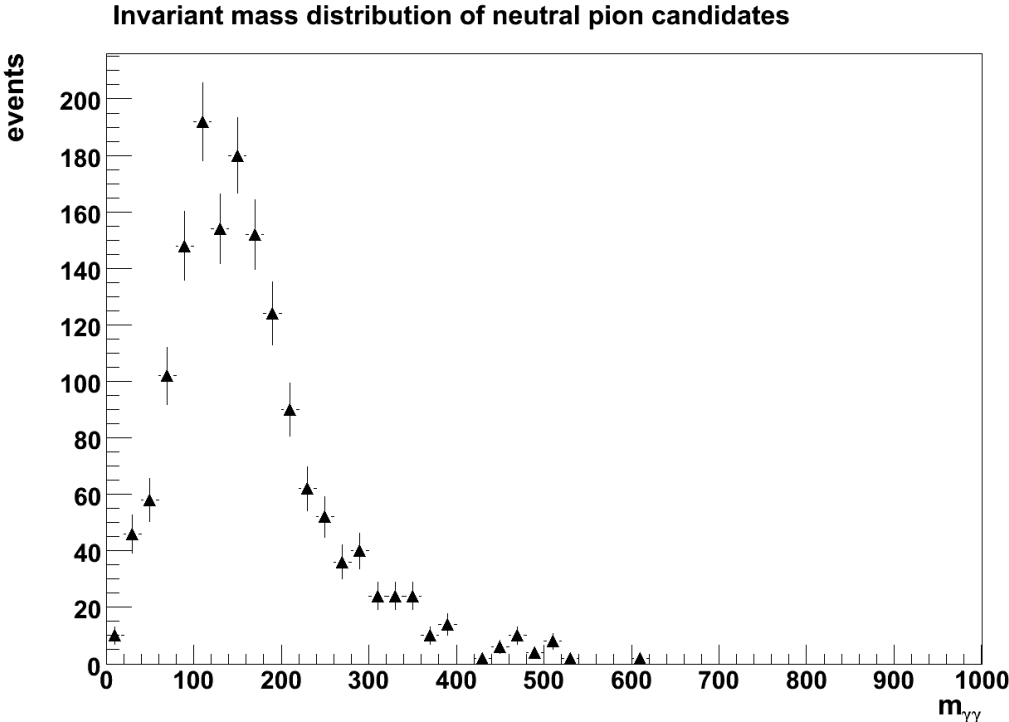
Figure 7.1: Invariant mass of two reconstructed clusters, both matched to a true photon.

Chapter 8

Conclusion

Tau leptons are important signatures for the search for new physics and the search for the Higgs boson of the Standard Model and supersymmetric extensions. While an algorithm for tau-lepton reconstruction and identification exists in ATLAS, its performance at low transverse momenta as well as an identification of the tau-lepton decay mode are areas where significant improvements can be made. The reconstruction of low p_T tau leptons is important for tau-leptons in long SUSY decay chains. The separation of $\tau^\pm \to \pi^\pm \nu_\tau$ from $\tau^\pm \to \rho^\pm \nu_\tau$ and $\tau^\pm \to a_1^\pm \nu_\tau$ decays is useful for studies of the tau-lepton polarization, for instance to get information about the spin of SUSY particles decaying into tau leptons. Based on this motivation, this thesis presented a detailed study of the tau-lepton substructure, in particular an algorithm for the reconstruction of neutral pions subshowers in hadronic tau-lepton decays is developed.

The reconstruction algorithm for neutral pion subshowers tries to identify neutral pions in an energy distributions after the charged pion's energy depositions have been removed. The algorithm is divided into four steps. At first the charged pion's energy depositions in the electromagnetic calorimeter are computed, which has been validated. The uncertainty is dominated by the energy measurement in the hadronic calorimeter. The second step is the energy subtraction using a parameterization of the charged pion shower development extracted from simulated $\tau^\pm \to \pi^\pm \nu_\tau$ decays. The subtraction shows in general satisfying results, but yields small imperfections close to the track. These imperfections and deviations of the average shower parameterization from the actual hadronic shower lead on average to ≈ 0.6 misidentified neutral pion candidates per tau-lepton decay. To further suppress the misidentified neutral pions, shower shapes variables of the neutral pion are used to train a neural network, which suppresses the misidentified neutral pion candidates. The suppression reduces the average number of misidentified neutral pion to ≈ 0.2 allowing for a identification of the correct number of neutral pions of $\tau^\pm \to \pi^\pm \nu_\tau$ decays in $\approx 80\%$. The reconstruction of $\tau^\pm \to \rho^\pm \nu_\tau$ decays is possible in $\approx 60\%$ and the reconstruction of $\tau^\pm \to a_1^\pm \nu_\tau$ in $\approx 40\%$ of all cases.

The efficiency dependence on tau-lepton kinematics has been studied. These studies showed, that the reconstruction of neutral pions close to the track works almost as good as the reconstruction of isolated neutral pions. Hence the subtraction of the charged pion energy allows to reconstruct neutral pions even if their energy depositions overlap with the ones from charged pions. As expected, the efficiency drops as the charged pion transverse momentum rises and the neutral pion transverse momentum decreases. In addition the resolution of neutral pion energy and direction have been studied. It turned out that the reconstruction of the neutral pion direction shows no bias and a good resolution. The reconstruction of the neutral pion's transverse energy is slightly biased towards smaller energies. The neutral pion

reconstruction allows for a classification of the decay mode as one of $\tau^\pm \to \pi^\pm \nu_\tau$, $\tau^\pm \to \rho^\pm \nu_\tau$ and $\tau^\pm \to a_1^\pm \nu_\tau$ decays.

A comparison of the efficiencies and resolutions obtained with the neutral pion reconstruction presented in this study to an already implemented one shows that the resolution and efficiencies could be improved for the $\tau^\pm \to \pi^\pm \nu_\tau$ and $\tau^\pm \to \rho^\pm \nu_\tau$ decays. In addition the resolution of the neutral pion transverse energies could be improved by more than $50\,\%$. Therefore one part of this thesis was the implementation of the reconstruction algorithm in the release 14.4.0 of the official ATLAS reconstruction software to make it available to all ATLAS users. The implementation is currently being validated.

This thesis presented also plans for validation of the neutral pion reconstruction with data using a $Z \to \tau^\pm \tau^\mp$ sample. The charged pion shower development and the shower shapes of neutral pion candidates must be validated. In addition plans for extensions and further improvements of the algorithm were presented, for instance the extension to the whole η-range and multi-prong tau-lepton candidates.

The neutral pion reconstruction developed in this thesis may also work for other particle decays. The subtraction of charged pion energy could improve more general reconstruction tools like the energy-flow algorithms. The work presented in this thesis will hopefully be used as a tool for new physics search and increase tau-lepton reconstruction and identification.

Appendix A

Appendix

A.1 Track Quality Criteria in Tau Lepton Reconstruction

The basic quality criteria tracks in the tau-lepton reconstruction are listed in the following [18].

- good fit of the track's space points (χ^2/NDF < 1.7)

- more than seven hits in the Semiconductor pixel and silicon microstrip layers

- more than nine "low-threshold" hits in the Transition Radiation Tracker

- less than six "high-threshold" hits in the Transition Radiation Tracker

- the transverse impact parameter must be smaller than one millimeter.

In addition to these criteria the track-seeded approach requires $p_T^{\text{Track}} > 9\,\text{GeV}$ for the track used as seed and the calo-seeded approach requires $p_T^{\text{Track}} > 1\,\text{GeV}$ for all tracks. In order to find a third track, the requirements on the TRT-hits are relaxed.

A.2 Available Cluster Moments

The CaloClusterMomentsMaker algorithm calculates shower shape variables for calorimeter clusters. For some of these variables the shower axis is needed as reference. It is calculated by finding an axis, which minimizes the energy weighted spatial correlations of all cells with positive energy belonging to the cluster. Therefore the symmetric matrix, C, is calculated Eq. A.1.

$$C = \begin{pmatrix} C_{xx} & C_{xy} & C_{xz} \\ C_{xy} & C_{yy} & C_{yz} \\ C_{xz} & C_{yz} & C_{zz} \end{pmatrix} \tag{A.1}$$

using

$$
\begin{aligned}
C_{xx} &= \frac{1}{w} \sum_i E_i^2 \left(x_i - \langle x \rangle \right)^2 \\
C_{xy} &= \frac{1}{w} \sum_i E_i^2 \left(x_i - \langle x \rangle \right) \left(y_i - \langle y \rangle \right)
\end{aligned}
\tag{A.2}
$$

with

$$w = \sum_i E_i^2 \ . \tag{A.3}$$

The index i runs over all cells with positive energy comprising the cluster. The eigenvector of the matrix, C, which is closest to the vector pointing from the interaction point to the shower center, $\vec{c}$ is then considered as the shower axis.

Once the shower axis, $\vec{s}$ is defined the lateral, r_i, and longitudinal, λ_i, distance of the cell i from the shower center can be defined as

$$
\begin{aligned}
r_i &= |(\vec{x_i} - \vec{c}) \times \vec{s}| \\
\lambda_i &= (\vec{x_i} - \vec{c}) \cdot \vec{s}
\end{aligned} \tag{A.4}
$$

.

Now the formulas for all moments used in this study can be listed in the following. All sums run over all cells with positive energy belonging to the cluster, and E_{norm} is defined as $E_{\text{norm}} = \sum_i E_i$.

$$
\begin{aligned}
\langle E/V \rangle &= \frac{1}{E_{\text{norm}}} \sum_i E_i \left(\frac{E_i}{V_i} \right) \\
\left\langle (E/V)^2 \right\rangle &= \frac{1}{E_{\text{norm}}} \sum_i E_i \left(\frac{E_i}{V_i} \right)^2 \\
\Delta\alpha &= \angle\, (\vec{c}, \vec{s}) \\
\Delta\phi &= \Delta\phi\, (\vec{c}, \vec{s}) \\
\left\langle \lambda^2 \right\rangle &= \frac{1}{E_{\text{norm}}} \sum_i E_i \left(\lambda_i^2 \right) \\
\left\langle \text{long}^2 \right\rangle &= \frac{\text{long}_2}{\text{long}_2 + \text{long}_{\text{max}}} \\
\text{long}_2 &= \left\langle \lambda^2 \right\rangle,\ \text{with } \lambda = 0 \text{ for the two most energetic cells} \\
\text{long}_{\text{max}} &= \left\langle \lambda^2 \right\rangle \text{ with } \lambda = 10 \text{ for the two most energetic and } \lambda = 0 \text{ for all other cells}
\end{aligned} \tag{A.5}
$$

A.3 Reconstruction Performance for the 1D Selection Criteria
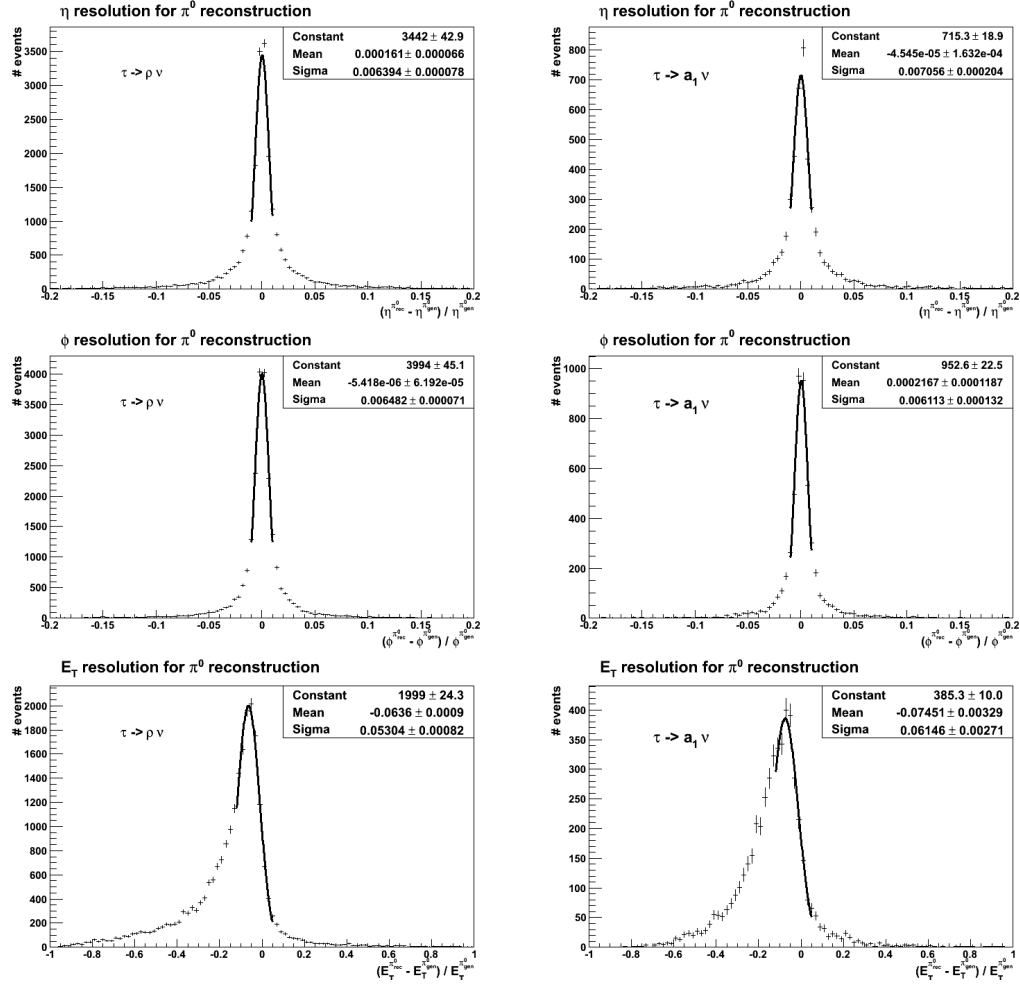
Figure A.1: Eta, phi and transverse energy resolution of reconstructed neutral pions for $\tau^\pm \to \rho^\pm \nu_\tau$ decays on the left hand and $\tau^\pm \to a_1^\pm \nu_\tau$ decays on the right hand. One dimensional selection criteria for fake suppression were used to create this plots. The resolutions are comparable to the ones shown in chapter six.
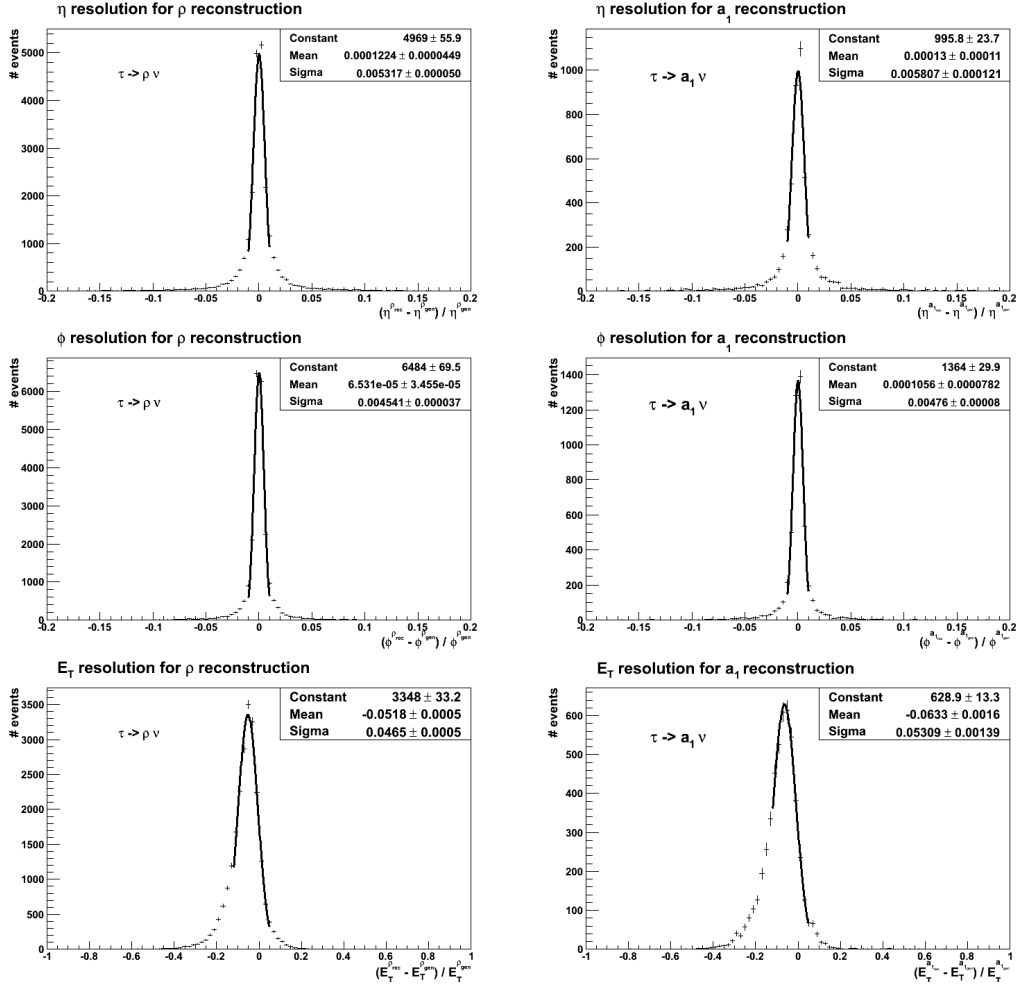
Figure A.2: Eta, phi and transverse energy resolution of the combined system track and reconstructed neutral pions for $\tau^{\pm} \to \rho^{\pm}\nu_{\tau}$ decays on the left hand and $\tau^{\pm} \to a_1^{\pm}\nu_{\tau}$ decays on the right hand. One dimensional selection criteria for fake suppression were used to create this plots. The reconstruction performs comparable to the one using the neural network for fake suppression.

List of Figures

List of Tables

Bibliography

[1] R. Barate et al. Search for the standard model Higgs boson at LEP. *Phys. Lett.*, B565:61–75, 2003.

[2] M. Gruenewald and D. Karlen. talks at international conference on high-energy physics, vancouver 1998, `http://www.cern.ch/LEPEWWG/misc`.

[3] D. N. Spergel et al. First Year Wilkinson Microwave Anisotropy Probe (WMAP) Observations: Determination of Cosmological Parameters. *Astrophys. J. Suppl.*, 148:175, 2003.

[4] Paul Langacker and Ming-xing Luo. Implications of precision electroweak experiments for M(t), rho(0), sin**2-Theta(W) and grand unification. *Phys. Rev.*, D44:817–822, 1991.

[5] A. Kaczmarska. Tau leptons as a probe for new physics at LHC. *Nucl. Phys. Proc. Suppl.*, 169:351–356, 2007.

[6] Monoranjan Guchait, Ritva Kinnunen, and D. P. Roy. Signature of heavy charged Higgs boson at LHC in the 1 and 3 prong hadronic tau decay channels. *Eur. Phys. J.*, C52:665–672, 2007.

[7] Martin L. Perl et al. Evidence for anomalous lepton production in e+ e- annihilation. *Phys. Rev. Lett.*, 35:1489–1492, 1975.

[8] C. Amsler et al. Review of particle physics. *Phys. Lett.*, B667:1, 2008.

[9] Achim Stahl. *Physics with Tau Leptons*. Springer tracts in modern physics ; 160. Springer, 2000.

[10] B. Aubert et al. Search for the decay $\tau^- \rightarrow 4\pi^- 3\pi^+ (\pi^0)\nu_\tau$. *Phys. Rev.*, D72:012003, 2005.

[11] B. K. Bullock, Kaoru Hagiwara, and Alan D. Martin. Tau polarization and its correlations as a probe of new physics. *Nucl. Phys.*, B395:499–533, 1993.

[12] Monoranjan Guchait and D. P. Roy. Using Tau Polarization for Charged Higgs Boson and SUSY Searches at LHC. 2008.

[13] T Nattermann, K Desch, P Wienemann, and C Zendler. Measuring tau-polarisation in neutralino2 decays at the lhc. Technical Report ATL-COM-PHYS-2008-242, CERN, Geneva, Dec 2008.

[14] AC Team. The four main lhc experiments. Jun 1999.

[15] G. Aad et al. The ATLAS Experiment at the CERN Large Hadron Collider. *JINST*, 3:S08003, 2008.

[16] C Roda and I Vivarelli. Cell based jet calibration. Technical Report ATL-PHYS-PUB-2005-019. ATL-COM-PHYS-2005-017. CERN-ATL-PHYS-PUB-2005-019, CERN, Geneva, 2005.

[17] W. Braunschweig et al. RESULTS FROM A TEST OF A Pb-Fe LIQUID ARGON CALORIMETER. DESY 89/022.

[18] Le Bihan A. C. et al. Identification of hadronic τ decays with ATLAS detector. Technical Report ATL-COM-PHYS-2007-066, CERN, Geneva, 2007.

[19] Christov A. et al. Performance of the tau reconstruction and identification algorithm with release 14.2.10. Technical Report ATL-COM-PHYS-2008-122, CERN, Geneva, 2008.

[20] D. Froidevaux, P. Nevski, and E. Richter-Was. Energy flow studies for hadronic tau's with DC1 data. Technical Report ATL-COM-PHYS-2005-024, CERN, Geneva, 2005.

[21] A. Aktas et al. Tau Lepton production in e p collisions at HERA. *Eur. Phys. J.*, C48:699–714, 2006.

[22] Christian Veelken. Search for Events with Isolated Leptons and Large Missing Transverse Momentum in e p Collisions at HERA. *Dissertation, Univ. of Liverpool (2005)*.

[23] Torbjorn Sjostrand, Stephen Mrenna, and Peter Skands. PYTHIA 6.4 physics and manual. *JHEP*, 05:026, 2006.

[24] S. Jadach, Z. Was, R. Decker, and Johann H. Kuhn. The tau decay library TAUOLA: Version 2.4. *Comput. Phys. Commun.*, 76:361–380, 1993.

[25] S. Agostinelli et al. GEANT4: A simulation toolkit. *Nucl. Instrum. Meth.*, A506:250–303, 2003.

[26] Yu. A. Budagov et al. Study of the hadron shower profiles with the ATLAS tile hadron calorimeter. 1997.

[27] S. Menke. Topological Clustering, `https://twiki.cern.ch/twiki/bin/view/Atlas/TopologicalClustering`.

[28] S. Menke. Cluster Moments, `https://twiki.cern.ch/twiki/bin/view/Atlas/ClusterMoments`.

[29] Andreas Hocker et al. TMVA: Toolkit for multivariate data analysis. *PoS*, ACAT:040, 2007.

Erklärung:

Ich versichere, dass ich diese Arbeit selbständig verfasst und keine anderen als die angegebenen Quellen und Hilfsmittel benutzt habe.

Heidelberg, den 01.01.2009

....
(Unterschrift)